SILESIAN UNIVERSITY OF TECHNOLOGY

Faculty of Chemistry

Department of Physical Chemistry and Technology of Polymers

Paola Zimmermann Crocomo

DOCTORAL DISSERTATION

The intermolecular and intramolecular donor-acceptor charge transfer behaviour as a way to control thermally activated delayed fluorescence emission.

Promoter: Prof. dr hab. inż. Przemysław Data

Gliwice 2022

Acknowledgements

Firstly, I would like to express my great appreciation for my supervisor Przemyslaw Data, who believed in my success and always motivated me to pursue my dreams. Thank you for your time, guidance, patience, support and most of all, for your friendship.

It is an honour to work in a chill environment, and for that, I have to thank all my colleagues in the EXCEED group. In particular, I would like to thank Marli, Leandro, Welisson, Nicolas, Klaudia, Rita, Radek, Damian, Ola, Agata, Sandra and Pavel for helping with my training, as well as time spent in long, fruitful discussions about chemistry.

Living in such a different country is always a challenge, and for certain, the friendships I made in Poland helped me endure academic life and the sadness of being so far from home. I was lucky to meet my girlfriend, Nerea, who has always encouraged and believed in me. My friends, Gabriel, Bonnie, Fasika, Wiktoria, Aravinth and Algharsi, brought me so much joy and made my days light and easy. To my Brazilian friends who are like family to me, Marília, Sheila, Tiago, Marcelly, Jakes, Nina, Thamara, Victoria, João, Edinho, and so many others who spent countless hours in video calls whenever I needed help and affection, my eternal gratitude.

Finalmente, gostaria de agradecer toda a minha família por sempre me encorajarem a seguir meu coração. Especialmente meus pais, Leila e Paulo que mesmo de longe se fazerem tão presentes, sou muito grata pelos seus conselhos, pela força e acolhimento que vocês sempre me deram. Amo vocês.

Financing Acknowledgements

Table of Contents

List of Abbreviations

^{3}LE	Local Triplet States
Ag	Silver
AgCl	Silver chloride
Al	Aluminium
Bu$_4$NBF$_4$	Tetrabutylammonium Tetrafluoroborate
CBP	4,4′-bis(N-carbazolyl)-1,1′-biphenyl
CCD	Charge-Coupled Device
CE	Counter Electrode
CT	Charge Transfer
D-A	Donor-Acceptor
D-A-D	Donor-Acceptor-Donor
DCM	Dichloromethane
DF	Delayed Fluorescence
EBL	Electron-Blocking Layer
E$_{HOMO}$	Energy level of Highest Occupied Molecular Orbital
E$_{LUMO}$	Energy level of Lowest Occupied Molecular Orbital
E$_{ox}$	Oxidation Potential
EPR	Electron Paramagnetic Resonance
EQE	External Quantum Efficiency
E$_{red}$	Reduction Potential
ETL	Electron-Transporting Layer
eV	Electron Volt
HAT-CN	(1,4,5,8,9,11-Hexaazatriphenylenehexacarbonitrile)
HBL	Hole-Blocking Layer
HIL	Hole-Injecting Layer
HOMO	Highest Occupied Molecular Orbital
HTL	Hole-Transporting Layer
ICT	Intramolecular Charge Transfer
IQE	Internal Quantum Efficiency
ISC	Intersystem Crossing
ITO	Indium Tin Oxide

LE	Locally-Excited
LED	Light-Emitting Diodes
LiClO$_4$	Lithium perchlorate
LiF	Lithium fluoride
LUMO	Lowest Unoccupied Molecular Orbital
MLCT	Metal-Ligand Charge Transfer
NPB	(*N,N'*-di(1-naphthyl)-*N,N'*-diphenyl-(1,1'-biphenyl)-4,4'-diamine)
O$_2$	Molecular oxygen
OLED	Organic Light-Emitting Diode
PF	Prompt Fluorescence
PLQY	Photoluminescence Quantum Yield
PMMA	Poly(methyl methacrylate)
PMT	Photomultiplier Tubes
Pt	Platinum
RE	Reference Electrode
rISC	Reverse Intersystem Crossing
RTP	Room-Temperature Phosphorescence
S$_0$	Singlet Ground State
S$_1$	Singlet Excited State
SOC	Spin-Orbit Coupling
T$_1$	Triplet Excited State
TADF	Thermally Activated Delayed Fluorescence
TCSPC	Time-Correlated Single-Photon Counting
THF	Tetrahydrofuran
TPBi	2,2',2"-(1,3,5-Benzinetriyl)-tris(1-phenyl-1-H-benzimidazole)
TSBPA	(4,4'-(Diphenylsilanediyl)bis(*N,N*-diphenylaniline))
TTA	Triplet-Triplet Annihilation
V	Volt
WE	Working Electrode
ΔE$_{ST}$	Singlet-triplet energy gap
λ$_{onset}$	Onset wavelength

List of Publications

1. **<u>CROCOMO, P. Z.</u>**; OKAZAKI, M.; HOSONO, T.; MINAKATA, S.; TAKEDA, Y; DATA, P. Dibenzophenazine based TADF emitters as dual electrochromic and electroluminescence materials, Chemistry A European Journal, **2022**. Manuscript accepted.

2. IZUMI, S.; GOVINDHARAJ, P.; DREWNIAK, A., **<u>CROCOMO, P. Z.</u>**; MINAKATA, S.; DE SOUSA, L. E.; DE SILVA, P. DATA, P.; TAKEDA, Y. Comparative study of thermally activated delayed fluorescent properties of donor–acceptor and donor–acceptor–donor architectures based on phenoxazine and dibenzo[a,j]phenazine, Beilstein Journal of Organic Chemistry, 18, 459–468, **2022**. https://doi.org/10.3762/bjoc.18.48

3. WAGNER, J.; CROCOMO, P. Z.; KOCHMAN, M. A.; KUBAS, A.; DATA, P.; LINDNER, M. Modular, n-Doped Concave PAHs for High-Performance OLEDs with Tunable Emission Mechanisms. Angewandte Chemie International Edition, **2022**. https://doi.org/10.1002/anie.202202232

4. HOSONO, T.; DECARLI, N. O.; **<u>CROCOMO, P. Z.</u>**; GOYA, T.; DE SOUSA, L. E.; TOHNAI, N.; MINAKATA, S.; DE SILVA, P.; DATA, P. TAKEDA, Y. The regioisomeric effect on the excited-state fate leading to room-temperature phosphorescence or thermally activated delayed fluorescence in a dibenzophenazine-cored donor-acceptor-donor system. Journal of Materials Chemistry C, 10, 4905-4913, **2022**. DOI: 10.1039/d1tc05730h

5. GOYA, T.; **<u>CROCOMO, P. Z.</u>**; HOSONO, T.; MINAKATA, S.; DE SOUSA, L. E.; DE SILVA, P.; DATA, P.; TAKEDA, Y. A New Entry to Purely Organic Thermally Activated Delayed Fluorescence Emitters Based on Pyrido[2,3-b]pyrazine–Dihydrophenazasilines Donor–Acceptor Dyad. Asian Journal of Organic Chemistry, 11, **2022**. https://doi.org/10.1002/ajoc.202100780

6. **<u>CROCOMO, P. Z</u>**.; KAIHARA, T.; KAWAGUCHI, S.; STACHELEK, P.; MINAKATA, S.; DE SILVA, P.; DATA, P.; TAKEDA, Y. The Impact of C2 Insertion into a Carbazole Donor on the Physicochemical Properties of Dibenzo[a,j]phenazine-Cored Donor-Acceptor-Donor Triads. Chemistry A European Journal, 27, 13390-13398, **2021**.

7. BARROS, M. R.; BITTENCOURT, O. R.; **<u>CROCOMO, P. Z.</u>**; MAFRA, G.; CARASEK, E.; MAGOSSO, H. A.; JOST, C. J.; WINIARSKI, J. P. Adsorption of Hazardous and Noxious 4-nitrophenol by a Silsesquioxane Organic-inorganic Hybrid Material. Journal of Sol-gel Science and Technology, 99, 402-412, **2021**. https://doi.org/10.1007/s10971-021-05573-3

8. **<u>CROCOMO, P. Z.</u>**; WINIARSKI, J. P.; BARROS, M. R.; LATOCHESKI, E.; NAGURNIAK, G. R.; PARREIRA, R. L. T.; SIEBERT, D. A. MICKE, G. MAGOSSO, H. A.; JOST, C. L. Silver Nanoparticles-Silsesquioxane Nanomaterial Applied to the Determination of 4-Nitrophenol as a Biomarker. Electroanalysis, 31, 2319-2329, **2019**. https://doi.org/10.1002/elan.201900217

1. Introduction

Over a hundred years ago, the houses were illuminated by incandescent light bulbs, which, to produce light, involved heating a wire filament until it glowed. Moreover, by the end of the 1930s, fluorescent lamps started to be commercialized, they were able to produce light from electrical energy up to six times more efficiently.[1]

Light-Emitting Diodes (LEDs) revolutionised the world when the first devices with practical use were invented,[2,3] changing the way to produce light without losing the biggest part of the energy as a waste of heat, like most of the old bulbs. Years of research ended up making tiny diodes more efficient, with immediate full brightness and many other exciting attributes.[4,5]

Subsequently, improvements kept coming, and after the first Organic Light-Emitting Diode (OLED) was reported in 1987,[6] the display industry expanded to an exciting range of applications, with thinner, lighter, brighter and even curved and flexible devices.[7,8]

The research does not stop discovering and evolving the way of producing light, and every day we realize the importance of finding better ways to reduce the waste of energy. Furthermore, optical devices are present everywhere in our daily lives, therefore, it is vital to understand better the processes that occur in their operation to produce lower-cost and more efficient illuminating devices.

At the present moment, the lightning market is still dominated by LEDs, although OLEDs have been trying to take over the market for a while now. The biggest limitation of typical fluorescent OLEDs is due to the maximum Internal Quantum Efficiency (IQE) of 25%. As a result of spin-statistics, phosphorescent OLEDs may achieve up to 100% IQE, although these types of devices generally are based on organometallic complexes containing heavy metals. With that in mind, the last years were marked by an increase in the development of heavy-metal free highly conjugated compounds exhibiting Thermally Activated Delayed Fluorescence (TADF) and/or Room-Temperature Phosphorescence (RTP), processes that revolutionized the optical field of research, on account of the possibility to increase the efficiency of OLED devices without the use of heavy metallic atoms, which are expensive and scarce nowadays.[9–11]

Through the hybridization of the lowest singlet and triplet excited states, TADF behaviour arises from the maximization of the use of excitons, resulting in characteristic

fluorescence emission spectra with lifetimes comparable with phosphorescent complexes. TADF compounds are characterized by molecules containing donor and acceptor groups, separated to decrease the conjugation, presenting small energy splitting between singlet and triplets ($\Delta E_{ST} < 0.3$ eV) and intramolecular charge-transfer character. TADF-based OLEDs have been thoroughly investigated in the past years,[9,12–14] producing highly efficient devices.[11]

Organic compounds that exhibit higher values for ΔE_{ST} usually are not efficient for TADF applications but can have potential as RTP emitters. Therefore, adjustment of different emission properties can be obtained by the use of similar structures with simple substituent modifications.[15]

The main purpose of this work is to report the investigation of TADF and RTP emitters through the characterization by electrochemical and photophysical methods and further application in the manufacture of OLEDs, with the intent of better understanding the distinct emission pathways and the parameters that can influence and optimize such processes.

2. Background Theory

2.1. Organic Emitters

In nature, we can find light-emitting organisms such as fireflies, fungi, bacteria, and marine animals like fishes, shrimp, jellyfish, and many others.[16]

The research interest in organic electroluminescence started with the anthracene crystal's light emission discovery report.[17] Organic materials can exhibit extremely high fluorescence quantum efficiencies in the visible spectrum, however, their use in optoelectronic devices was hampered by the high voltage requirement for the injection of charges into organic crystals.[6] Devices containing organic materials resulted in significantly lower efficiencies and lifetimes when compared to inorganic materials.[18]

The successful application of such compounds in optoelectronics was established at the end of the 1980s,[6,19] marking the start of a new generation of lightning devices. A wide range of properties can be achieved and studied, from the use of low molecular weight to conjugated oligomers or polymers.[18] One of the significant advantages of using organic compounds is the possibility of playing with their properties by simple changes in their molecular structure.[10]

Nowadays, the search for all-organic emitters comes from the will to overcome the use of rare and expensive materials, such as heavy metals like iridium and platinum.[9]

2.2. Electronic Transitions in Organic Emitters

When a molecule absorbs the necessary amount of energy, it undergoes electronic transitions from the ground state (S_0) to one of the excited states (S_1, S_2 or T_1), as shown in Figure 1 in Jablonski's diagram. The absorbed energy can be released through radiative and non-radiative deactivation processes, which happen sequentially or simultaneously. One of the consequences of non-radiative decay is the dispersion of thermal energy.[20]
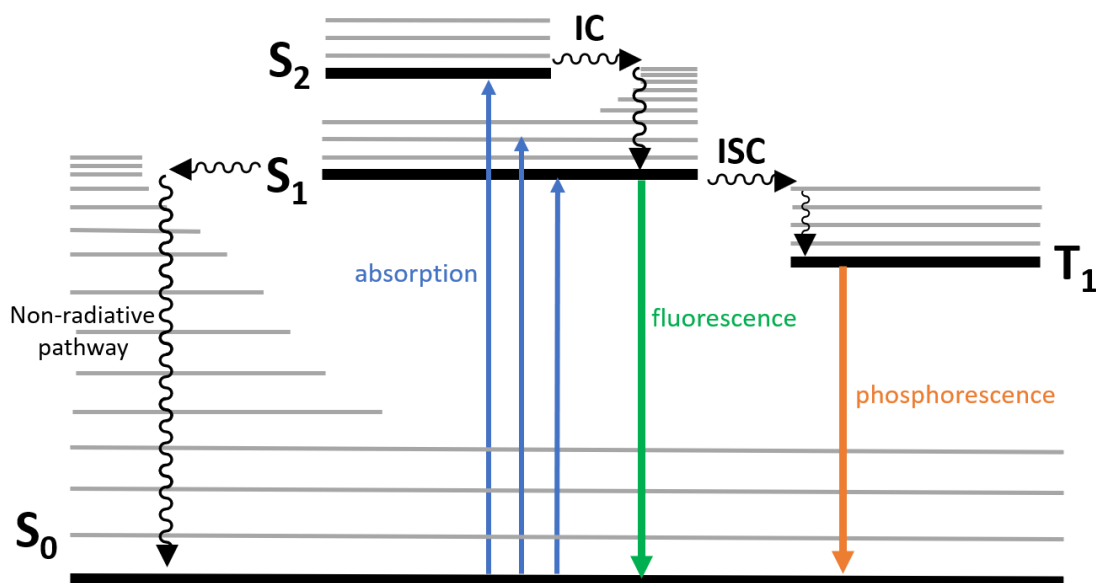
Figure 1. Jablonski Diagram for absorption, fluorescence, phosphorescent and adjacent processes. Adapted from references.[9,21] IC – Internal Convertion; ISC – Intersystem Crossing, S_0 – singlet ground state; S_1 and S_2 – singlet excited states; T_1 – triplet excited state.

In the case of radiative pathways of energy release, emission of photons (light) could be induced, that is the desired outcome in the study of light-emitting devices. A molecule in the excited state which relaxes to S_0 through radiative pathways can undergo different processes to reach S_0.[9]

The fastest radiative deactivation process is the transition from the singlet excited state (S_1) to the ground state (S_0), and the emission which arises is called fluorescence. The triplet excited state (T_1) is a metastable energy level, usually with lower energy than the relative singlet states, and the probability of transitions from T_1 to S_0 is very small. This transition takes longer time, which increases the quenching of the triplet excited states. Regardless of the low probability, this transition arising from triplet states can happen under proper conditions and is accompanied by phosphorescence emission.[21] The phosphorescence emission decay lifetimes are considerably more significant than the fluorescence decay.[22]

As a characteristic, a molecule in a singlet state (S) possesses two electrons with opposite (antiparallel) spins. From the singlet excited state S_1, a molecule can undergo an Intersystem Crossing (ISC) process, changing the orientation of spins between the two electrons, becoming parallel, which characterizes a triplet excited state (T_1).[9]

Since electrons present parallel spins in triplet excited states and antiparallel spins in singlet states, the transition from T_1 to S_0 (phosphorescence) has a spin-forbidden nature. On the other hand, fluorescence processes are considered spin-allowed because, in this case, changes in spin orientation are not required. For this reason, phosphorescence emission has a low probability of occurring, and its rate constant is very small at room temperature.[21,23,24] At very low temperatures, it is possible to eliminate the thermal deactivation processes that quench triplet states, making it easier for the transition from T_1 to S_0 to occur, hence the phosphorescence emission can be observed.[9]

The study and understanding of such transitions are of great importance for developing improved lightning devices and displays.

2.3. Organic Light-Emitting Diodes (OLEDs)

An OLED is basically a LED containing an organic compound(s) in its structure and exhibits light-induced emission by electric current.[7] The first successful OLED was reported in 1987 by Tang and VanSlyke, where a double-organic-layer device presented high green electroluminescent efficiency, fast response, and low voltage drive (starting at 2.5V) in a basic fabricated structure.[6]

Device architecture has faced many changes since the development of the first reported OLED, however, the primary structure remains the same, constituted by a thin organic emitting layer placed between two electrodes, one of which must be transparent.[25,26] Improved devices can be developed by carefully adjusting the different layers, ranging from basic three-layer structures to multi-layer devices. Extra layers with specific functions have been added with the intention of enhancing device efficiencies, such as Hole-Injecting Layers (HIL), Hole-Transporting Layers (HTL), Hole-Blocking Layers (HBL), Electron-Blocking Layers (EBL) and Electron-Transporting Layers (ETL).[25,27,28] Additionally, the emissive layer consists of the emissive compound dispersed into a host to avoid light quenching and degradation.[26,29]

An example of an OLED device with a simplified structure consists of electron and hole transporting layers, with a recombination layer between them, and these three layers are restrained by the cathode and anode electrodes, as shown in Figure 2.[22]
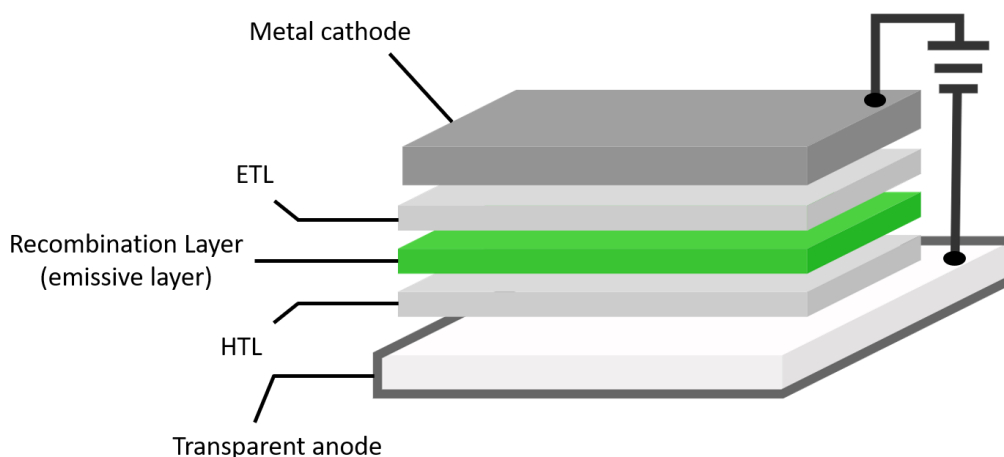
Figure 2. Example of a simplified OLED structure. Adapted from references.[13,22] *ETL –*
Electron-Transporting Layer; HTL – Hole-Transporting Layer.

Light emission arises from the exciton formation when positively charged holes and negatively charged electrons find each other at the recombination layer. Electrons and holes are attracted to each other by Coulomb interaction. The metal cathode is responsible for the injection of electrons into the Lowest Unoccupied Molecular Orbital (LUMO) of the material residing at the electron transporting layer, where the electrons jump from one molecule to the other in the direction of the anode. While the anode, which consists of a transparent semiconductor material, usually Indium Tin Oxide (ITO) coated glass, induces hole injection into the Highest Occupied Molecular Orbital (HOMO) of the HTL material. Although hard to imagine the conductivity of holes, it happens when the anode removes one electron of an organic material's HOMO, forming a positive charge in one molecule, and eventually, this charge is compensated by an electron of a neighbouring molecule, transferring the positive charge to this following molecule, and the continuity of this process consists in the conduction of the positive charge, also called as the hole.[22]

Charge recombination, which happens in the functioning of an OLED structure, generates singlet and triplet excited states. In quantum mechanical treatments, the spin of an electron can be described by an angular momentum operator, thus, electrons and holes possess an intrinsic spin quantum number $s = \frac{1}{2}$, which can exist in two states $m_s = +\frac{1}{2}$ or $m_s = -\frac{1}{2}$. In the presence of two electrons, statistically is possible to form four different spin combinations: one with antiparallel spins and total spin number $S = 0$ ($m_s = 0$); and three combinations of parallel spins with a total spin number $S = 1$ ($m_s = -1, 0, +1$),

resulting in one singlet and three triplet excitons formed as is depicted above, in Figure 3.[24]
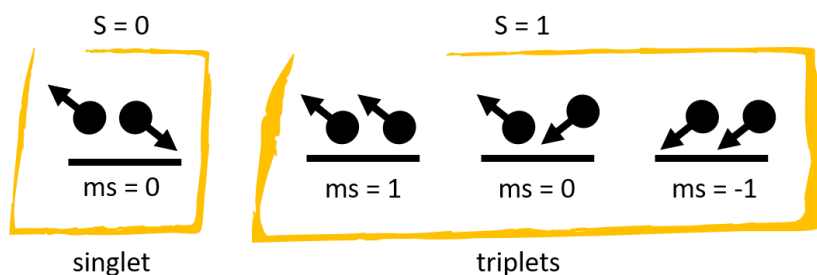
Figure 3. Schematic representation of spin combinations following charge recombination in OLEDs. Adapted from references. [30,31]

Among the many important aspects that contribute to the OLED performance, the Photoluminescence Quantum Yield (PLQY) and the exciton usage efficiency of the emitter compound are top priority.[32]

In most organic molecules, the triplet excited states are not emissive at room-temperature, therefore, an OLED that consists of a purely fluorescent emitter will be able to emit only 25% of the excitons formed, possibly losing 75% of energy through non-radiative decay processes (Figure 4).[23,24,30,33] The External Quantum Efficiency (EQE) of an OLED device is ruled by a mathematical equation, which defines that pure fluorescent OLED devices (with internal quantum efficiency limited to 25%) can have EQE up to only 5%.[23,33]
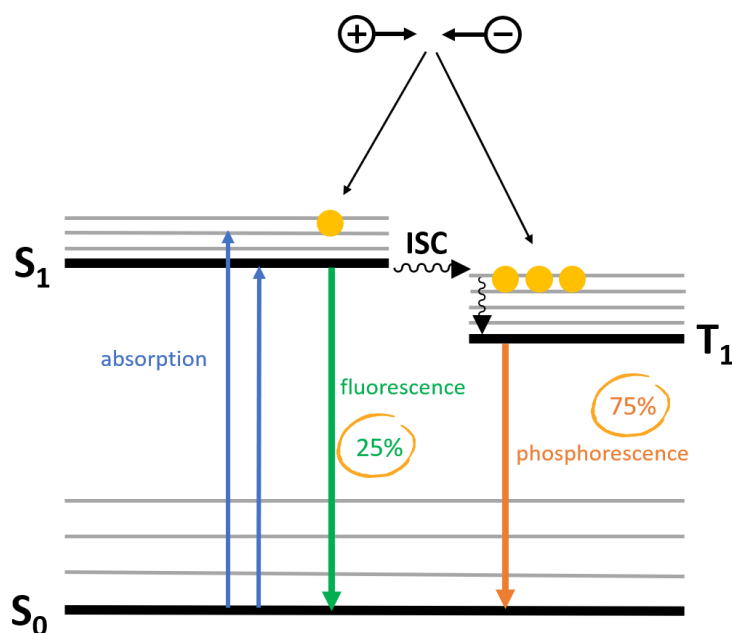
Figure 4. Jablonski Diagram for a fluorescent emitter-based OLED. Adapted from references.[9,13,34]

A specific characteristic is observed in heavy metal ions such as Ir(III), Os(II) and Ru(II): the presence of Metal-Ligand Charge Transfer (MLCT) state induces enhanced Spin-Orbit Coupling (SOC), where singlet and triplet excited states hybridize.[35–37] Thus, the existence of phosphorescence emission without the need for extremely low temperatures is called RTP, which relies on an intrinsic fast ISC process induced by the strong SOC, increasing the probability of the transition T_1-S_0 to occur.[9,23,24]

Phosphorescent materials based in complexes containing such heavy metal ions can harvest the energy of singlet and triplet excitons and populate the T_1 state with all four possible spin orientations, resulting in IQEs up to 100%. Theoretically, phosphorescent OLEDs can achieve efficiencies four times larger than pure fluorescent devices, reaching EQE of around 20%.[23,30,33] Experimentally is possible to assemble optimized devices to achieve higher efficiencies, for example, with the appropriate choice of host[12], increasing the out-coupling efficiency by inducing the orientation of the emitter molecules[38] or by the addition of surrounding materials[39]. However, in this work, we focus more on understanding the processes that occur in the emitter compound.

Ir(III) complexes are attractive due to their relatively short triplet lifetime (large rates for the transition T_1-S_0)[30] and high PLQYs. They have been extensively applied as an emitter layer in OLEDs and result in high-efficiency devices.[36,37,40–43] However, iridium is a

material that has increased its value by more than 140% in 2021. Its attractive use as a catalyst for the production of H_2 from water expanded its demand uncontrollably. Not only expensive but there is also not much iridium available on Earth, as it's a side-product obtained from the mining of palladium and platinum.[44,45]

To avoid increasing ecological problems using iridium on large scales, Delayed Fluorescence (DF) appears as one very interesting way to overcome limitations and produce high-efficiency OLED devices with all-organic compounds without the presence of heavy metal atoms. DF relies on a reverse ISC (rISC) process, which transfers energy from the excited triplet state to the excited singlet state.

There are two types of DF. P-type delayed fluorescence, where the activation energy for rISC to occur is provided from the interaction of two molecules in the excited triplet state, promoting energy transfer from one to the other, resulting in one of the molecules in the ground state and the other in the excited to a singlet state. A radiative decay from the generated singlet state leads to delayed fluorescence emission. This process is also called Triplet-Triplet Annihilation (TTA), and its maximum internal quantum efficiency is limited to 50%.[46]

The second type of DF is called E-type delayed fluorescence or TADF.

2.4. Thermally Activated Delayed Fluorescence (TADF)

As a continuity of a study from 1930, where long-lived luminescence was observed, in 1961, Parker and Hatchard reported for the first time the definition of E-type fluorescence from studies of the TADF behaviour of the compound eosin.[47] Although the mechanism involved in the TADF process was better studied and described only in 1986.[48] Moreover, in 2009, Prof. Adachi's group of research published for the first time the application of TADF emitters in OLED structure as a way to achieve enhanced devices.[34]

The fundamental principle for molecules to exhibit TADF properties is a small gap between the energies of T_1 and S_1 (ΔE_{ST}). For gaps small enough, only the increase of molecular vibration by the thermal energy from the surrounding is required as the activation energy for the rISC process, harvesting the triplet excitons back to S_1 and allowing, theoretically, 100% efficiency, as depicted in Figure 5. In this case, the radiative

decay derived from S_1 to S_0 is TADF emission, with the same characteristics as fluorescence and lifetimes comparable to phosphorescence emission.[9]
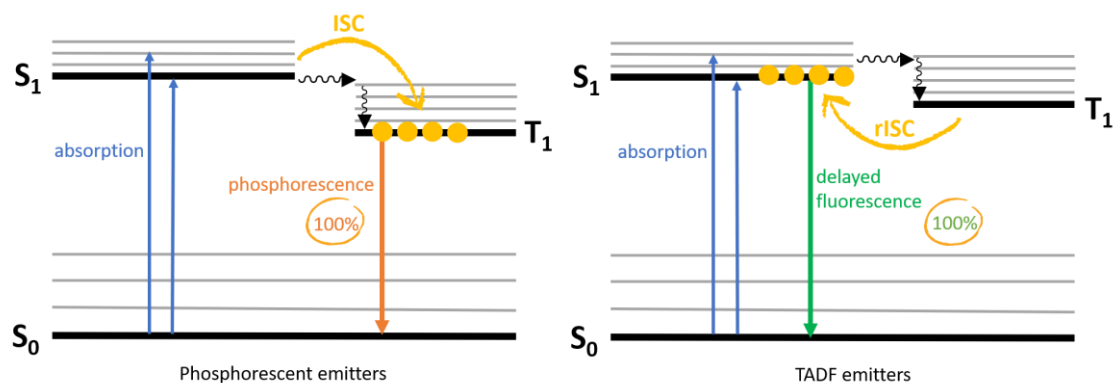
Figure 5. Jablonski diagram for phosphorescent-based and TADF-based emitters.

In practice, studies showed that molecules with Donor-Acceptor (D-A) and Donor-Acceptor-Donor (D-A-D) structures, where donor and acceptor are weakly coupled, present the feature of having a small/minimum overlap between the frontier orbitals, having LUMO situated over the acceptor moiety and HOMO placed mostly over the donor part of the molecule. Such structures comprise a reduced spin exchange energy, achieving small ΔE_{ST}, and for this reason, are extensively used for the study of TADF properties.[9,10,49,50] The angle between donor and acceptor moieties is highly determinant for the final observed emission. The molecular conformation will affect the energy levels and the spatial disposition of the frontier orbitals.[9] Chen *et al.* demonstrated the possibility of tuning between RTP and TADF properties with simple chemical modifications, which lead to different conformations in the exited states, influencing the final radiative emission pathway.[15] Furthermore, different colour emissions can be displayed by the same compound, derived from different molecular conformations achieved by mechanical interferences, and they are known as mechanochromic materials.[9,51,52]

On account of the HOMO and LUMO separation of some D-A and D-A-D structures, the absorption of photons leads to a transfer of electron density from the donor to the acceptor part, which means that the dipole moment of the molecule in the excited state is quite different than in the ground state. This process is known as Intramolecular Charge Transfer (ICT) and results in a Charge Transfer (CT) excited state.[49] In a comparison study of similar molecular structures with the same acceptor moiety, donor groups with

high electron-donating property lead to high ICT character and large HOMO-LUMO split.[49]

Generally, excited states can be divided into two categories: Locally-Excited (LE) and CT states. Such states can exist as singlet or triplet excitons, which will be indicated as a superscript on the left side, given origin to the definitions: ^{1}LE, ^{3}LE, ^{1}CT and ^{3}CT. The most significant difference between LE and CT is the former presents a large overlap between the orbitals involved, while the latter is characterized by the spatial separation between HOMO and LUMO. Emission spectra originated at LE states are represented by well-resolved thin signals, however, CT emission spectra are known for their structureless Gaussian line shape. In D-A molecular systems, electronic transitions may generate excitons localized on the donor or acceptor moieties that are represented as (D*–A) or (D–A*); or it may trigger a transfer of charge creating CT states that can be described as (D+ –A).[53]

In systems where ISC and rISC processes occur with a high rate constant, T_1 and S_1 are attributed to LE and CT states, respectively.[54] However, extensive research and study driven by the attempt to understand DF mechanisms better revealed mixed CT-LE states involved in TADF emission, mediated by the electronic coupling of the local triplet (^{3}LE) and the charge transfer states (^{1}CT and ^{3}CT).[50,55]

Hence, the basic criteria for emitters to display TADF emission is the minimization of the singlet-triplet gap. However, there is a rare possibility of careful molecular engineering strategies achieving such a high stabilization of the singlet state, resulting in a lower energy degree than its corresponding triplet state (T_1). This phenomenon, called singlet-triplet inversion (Figure 6), increases the rate of energy transfer of rISC once the conversion of triplet into singlet excitons now is an energy relaxation process, promoting the triplet contribution for the overall emission, supporting up to 100% of triplet-singlet conversion.[56]
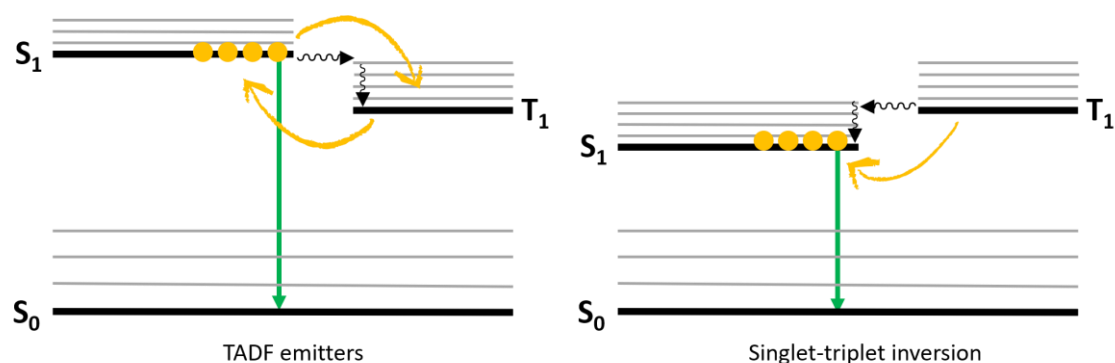
Figure 6. Jablonski diagram for TADF emitters and singlet-triplet inverted materials.

The singlet-triplet inversion effect was observed in recent works for heptazine systems,[57] and better studied for triangle-like shape N-substituted hydrocarbons through a theoretical study in an attempt to establish the importance of heteroatom substitution and to determine the pre-requisites for achieving the inversion.[58] Additionally, de Silva reported an investigation from the perspective of the electronic structure theory, imposing the requirement of LE character, along with double excitations and CT character, to provide the possibility of achieving emitters with gap inversion.[56] Although there is increasing interest in such effect and many theoretical studies, there is yet to see the application of materials containing singlet-triplet inversion in OLED devices.

The use of TADF and RTP all-organic materials to produce enhanced devices revolutionized the optical field of research as an alternative to obtain highly efficient OLEDs without the use of scarce and expensive heavy metallic atoms. Recent works have reported TADF-based OLED with 38% EQE.[11]

With the aim of better understanding the emission processes, looking for ways to increase device efficiencies, and designing novel compounds for the application in active layers in OLED's structure, the characterization and study of TADF behaviour is of utmost importance.

2.5. Characterization of TADF Compounds

2.5.1. Solvatochromism

Since most of the known TADF emitters are donor-acceptor molecules, the CT state and its energy are essential knowledge to be acquired.

21

The CT excited state is characterized by a larger dipole moment compared to the ground state. Consequently, the presence of polar solvents and matrices stabilises the CT state, which has its energy decreased and corresponding red shift of the emission spectra (larger red shifts with increasing polarity). Hence, this effect is used for a fast study, analyzing the emission spectra of a compound in solvents of different polarities. A red shift observed with the increasing polarity is a strong indication of the presence of the ICT process.[9]

As an example of a solvatochromism study, the emissions of the same compound's solutions in tetrahydrofuran (THF), toluene and dichloromethane (DCM) can be compared. In this case, toluene exhibits the lowest polarity values and DCM the highest, leaving THF with intermediate polarity. [59] Therefore, such a study would be expected a TADF molecule to exhibit red-shifted emission when solubilized in THF and DCM, in comparison with the toluene solution emission. However, as shown in Figure 7, "A" is an example of a TADF molecule, presenting solvatochromic shifts, and B is a molecule with no CT state, where emission has no significant influence from different solvent polarities.
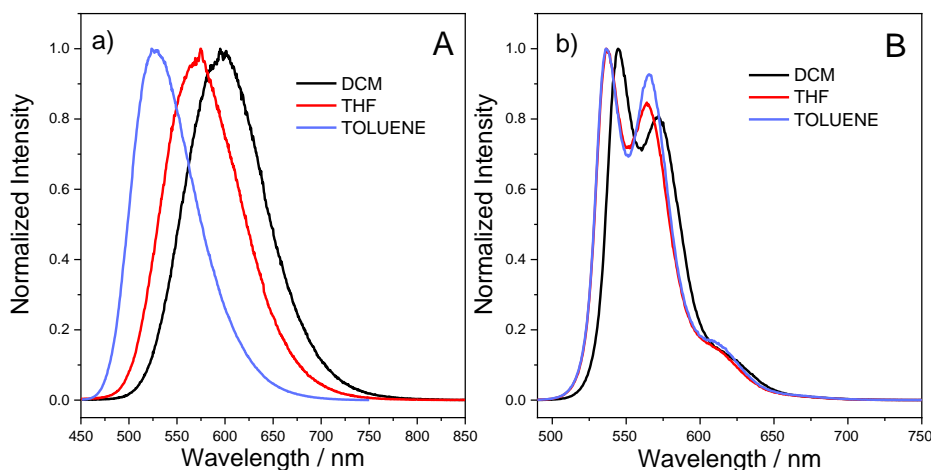
*Figure 7. Solvatochromism study for **a**) a TADF molecule and **b**) a molecule with no TADF properties.*

2.5.2. Oxygen Effect

Luminescence can be affected by some environmental factors. Kautsky observed that the presence of oxygen could quench fluorescence and phosphorescence processes, however, phosphorescence was extremely sensible, regardless of the oxygen pressure.[60]

Quenching is defined by the energy transfer from an excited molecule to a quencher in the ground state. After the quenching process, the quencher molecule will be in the excited state, and the other molecule will decay to the ground state (Figure 8). Although the energy transfer will only occur when the energy of the triplet state of the first molecule is higher than the triplet state of the quencher.[24]

Therefore, the reason for the greater sensitivity of phosphorescence towards oxygen is because the ground state for molecular oxygen (O_2) is a triplet state,[61] and its singlet excited state has very low energy (0.98 eV), which makes O_2 an excellent and well-known quencher for processes involving triplet excited states.[24,62,63]
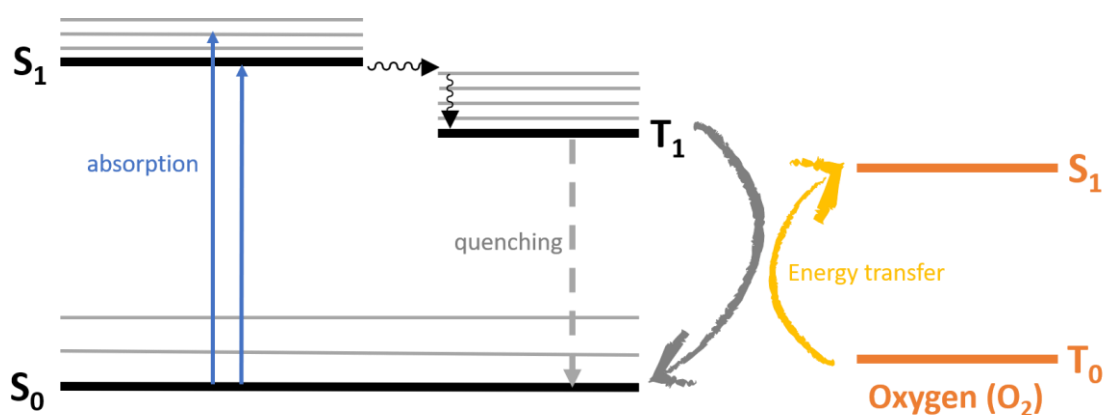
Figure 8. Jablonski diagram for Oxygen quenching of luminescence.

As phosphorescence, the TADF process also originates from triplet excited states. Therefore, any action that influences the triplet state also influences the intensity and lifetime of the TADF emission.[49]

Consequently, we can use this correlation to confirm the presence of emissions originating from triplet states with a straightforward and fast experiment called degassing: measuring the intensity of emission with and without oxygen for comparison.

Additionally, since TADF emission is extremely weak or non-existent in the presence of oxygen, it is considered that Prompt Fluorescence (PF) and DF are observed under degassed conditions, while only PF is detected under air conditions. The proportion between DF and PF (DF/PF) can be obtained by the direct ratio of the integrated spectra, resulting in a key parameter of TADF materials characterization.[54]

2.5.3. Photoluminescence Decay (Lifetime)

Accordingly to what we have discussed, the photoexcitation of a molecule will generate singlet and triplet excited states, followed by the relaxation to the ground state, which may be accompanied by the emission of light. The kinetics of the relaxation from a singlet state will differ from the kinetics of the relaxation of a triplet excited state regarding the average time the electrons spend in the excited states, what is called luminescence lifetime.[64]

Fluorescence is a very fast process, due to its spin-allowed nature, with a higher probability of occurring, its lifetime usually varies from 1 to 100 ns. Whereas the TADF process involves electron transfer to form a CT state, ISC to the local triplet states (^{3}LE) and a flip back to S_1 through rISC, where it will decay to S_0 by radiative emission. Due to all these processes and triplet excited states' long-live nature, the final emission can be detected with lifetimes from 1 μs to 100 ms.[9] For this reason, the lifetime of the emissive processes is an element of significant importance in the study of DF.

More than that, one important factor that interferes with OLED's operation is the efficiency roll-off, which is the decrease in efficiency with higher brightness and current density, both needed for application in displays.[65] However, this roll-off can be reduced by using compounds with short emission decay times.[30]

Time-Correlated Single-Photon Counting (TCSPC) is a common, well established and widely used method that allows for measuring photoluminescence decays, which relies on detecting single photons, measuring their arrival time-correlated to the laser pulse excitation. Using a high repetitive light source and Photomultiplier Tubes (PMT) is a high-resolution technique. The resulting histogram of the luminescence intensity *vs.* time represents the decay curve, as can be seen in Figure 9.[66]
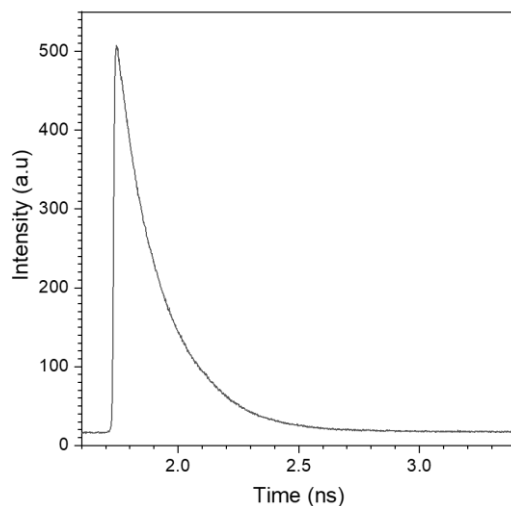
Figure 9. Example of a TCSPC histogram.

Moreover, relying on the kinetic of relaxation processes from different excited states, time-gated acquisition analysis allows to differentiate of the emission of distinct species based on the investigation of photons at a chosen time window while disregarding the other photons.[64] With the use of a Charge-Coupled Device (CCD), the camera, an invention that won part of the physics Nobel prize in 2009,[67] is possible to measure individual spectra with specified delay and integration times, as well as compose a decay curve by the compilation of many spectra in a wide range of delay and integration times, as shown in Figure 10.
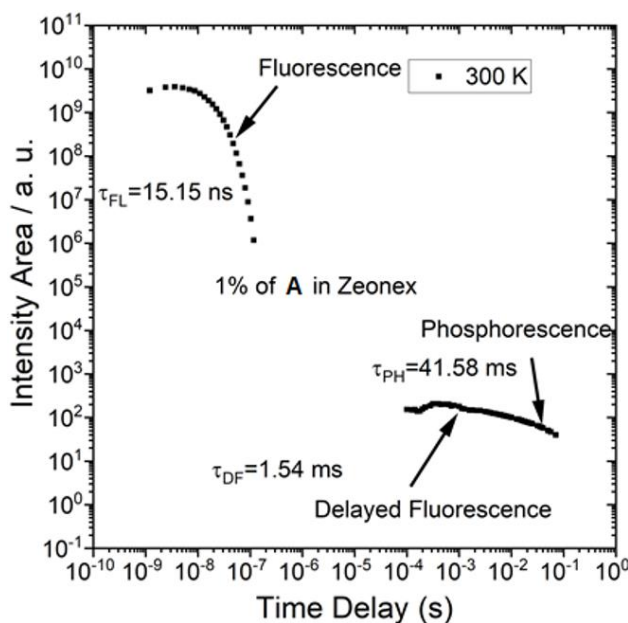
Figure 10. Decay curve of compound A in Zeonex® matrix, at 300 K.

Obtaining emission spectra at different temperatures during the time-resolved photoluminescence measurements allows us to estimate the exact point where the thermal activation for the TADF process occurs. For example, it is possible to differentiate TADF or RTP mechanisms by comparing spectra collected in different time regimes, from ns to ms.

2.5.4. Determination of ΔE_{ST}

The energy levels of T_1 and S_1 are the most important parameters to acquire in understanding the TADF process. It is assumed that the rISC process only requires thermal energy from the surroundings to occur, and for that reason, TADF's intensity and lifetime are strongly dependent upon temperature. In some of the cases, at temperatures around 77K, TADF emission is not observed, although, for emitters that exhibit a very small ΔE_{ST}, 77K can still be sufficient thermal energy to assist the rISC process.[49]

While TADF emission is more intense at room temperature, phosphorescence is usually stronger at very low temperatures. Moreover, the non-radiative decays are expected to be eliminated at extremely low temperatures. Using this principle, it is assumed that at 10 K, no TADF process can occur, and ΔE_{ST} can be drawn from the comparison of spectra of pure fluorescence and pure phosphorescence.[49]

According to Planck's theory,[68], the energy of light is proportional to its frequency. With that in mind, the energy of the excited state can be calculated from the onset wavelength (λ_{onset}) of its emission spectra, which delimits the minimum amount of energy necessary for such transition to occur; or it can also be drawn from the maximum of the emission peak, depending on the interest of the investigation. As we can see in the example of Figure 11, the energies of S_1 were drawn from the onset of fluorescence spectra at room temperature (300 K), while the energies of T_1 were taken from phosphorescence spectra at 10 K, and ΔE_{ST} is the difference between the energies of S_1 and T_1.
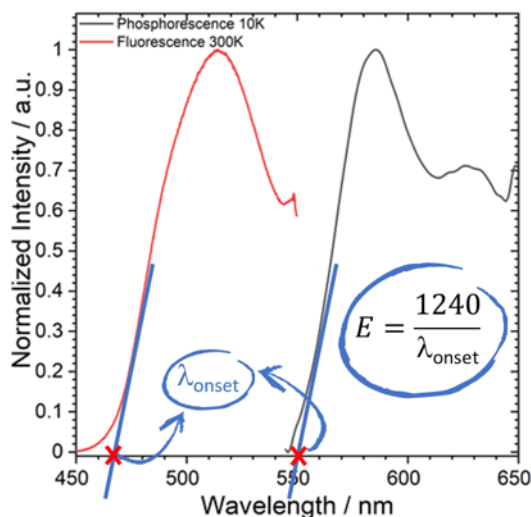
Figure 11. Fluorescence and phosphorescence spectra of compound A's layer in Zeonex® matrix.

For the investigations of such parameters, it is required equipment functioning at extreme low-temperature conditions, high-resolution spectroscopic methods and time-resolved measurements.

2.5.5. Electrochemistry

After a thorough investigation of the photophysical characteristics, the next step is the understanding of the emitter's electrochemical properties, which is extremely important considering the application of the TADF compound in OLED's structure once the devices work under applied voltage.

Voltammetry is one of the most commonly used electrochemical techniques. The study of the analyte consists of the measurement of the oxidation or reduction processes and the resulting current on the surface of the electrode when applying a difference of potential.[69]

As a result of applied voltage, with the help of a potentiostat, electrodes and electrolyte ions, an organic molecule can be reduced or oxidized via heterogeneous electron transfer, providing information about this molecule's thermodynamic and/or kinetic parameters.[70]

For Cyclic Voltammetry (CV) measurements, a typical and generally used set-up is the electrochemical cell with three electrodes that contain a working (WE), a reference (RE) and a counter electrode (CE), dipped in a solution containing the analyte and a supporting

electrolyte, usually in a glass container, all connected to a potentiostat, as showed in Figure 12. The potentiostat is an electronic device which enables the potential to be applied in the system, inducing current flow among WE and CE. It is used for controlling and measuring the voltage enclosed by WE and CE, adjusting and maintaining the potential difference between WE and RE. The potentiostat is connected with a data acquisition unit and controlled by software that uses a direct current power source to produce the potential difference.[71] The produced electrical current flows between the WE and CE, and the function of CE is to complete this electrical circuit, allowing the current to flow during the experiment. CE and WE should be made of conductive and inert material, and CE should own a larger surface area than the WE to avoid interference in the reactions happening at the WE. The potential at the WE varies linearly with time, while the potential is maintained constant at RE.[70]
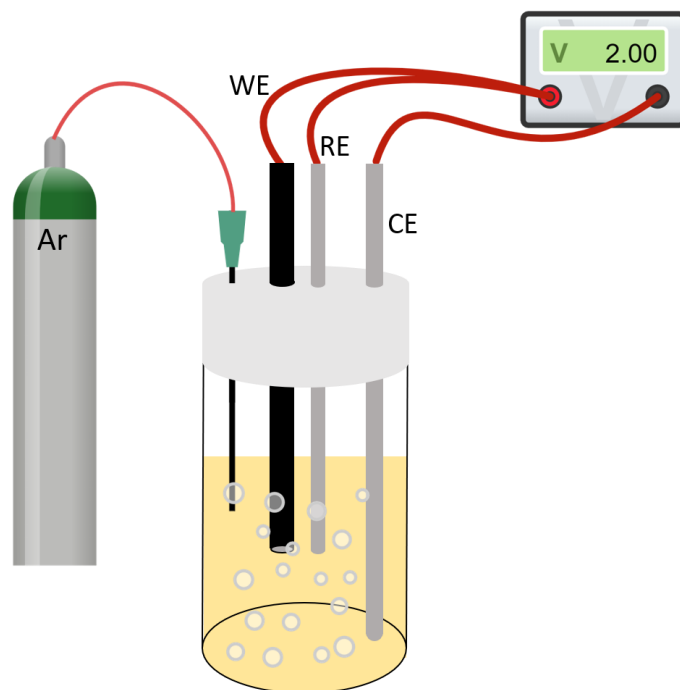
Figure 12. Representation of electrochemical cell.

Electrochemical measurements in aqueous solutions are easily comparable with reliable reference electrodes such as normal hydrogen or saturated calomel. However, the analysis of organic molecules requires the use of organic solvents. Therefore, to allow comparisons between measurements in several different solvents, ferrocene is used as standard. Ferrocene is an electrochemically stable compound and generally does not interact with other species in solution, its use is convenient and reproducible.[72]

One of the main functions of the supporting electrolyte is to decrease the resistance of the solution, enabling the conduction of charges and providing the mobility of ions to the electrodes during oxidation or reduction processes. During the electron transfer between electrode and analyte, the movement of electrolyte ions can balance electrical neutrality.[73]

The movement of electroactive species inside an electrochemical cell, either from the bulk of the solution to the electrode's surface, or vice-versa, can be controlled by three mechanisms of mass transport: convection, diffusion or migration. Convection consists of the movements caused by the action of mechanical forces such as gravity or pressure; diffusion originates from differences in concentration between two places, resulting in the movement of the analyte from areas with higher to lower concentrations to maximize its entropy; and migration is defined by the movement of ions caused by the presence of an electric field.[73,74]

The energy of the electrons at the surface of the working electrode is regulated by the potentiostat, which can be slowly increased until it reaches levels higher than the energy at the LUMO of the analyte, when consequently, an electron is transferred from the electrode to the analyte's molecule, reducing it. The potential value regarding the amount of energy necessary for the reduction is called Reduction Potential. The oxidation potential is measured similarly, by electron transfer in the opposite direction, from the analyte to the electrode's surface.[70]

The combination of solvent and supporting electrolyte compose the electrolyte solution. Depending on the choice of combination, one can have different ranges of potential where the electrolyte solution is stable and on which the electrochemical experiment can be performed.[70] This range of potential limits the values of HOMO and LUMO's energy levels that can be detected.

2.5.6. Spectroelectrochemistry

One of the few inconveniences that can be found in OLED displays is that they do not last as long as their analogous LCDs and LED displays.[75] The device's lifespan can be compromised by three important factors: dark spot formation, a sudden decrease of luminance due to electrical shorting, catastrophic failure, or intrinsic degradation. The

first two can be avoided through device encapsulation and improved deposition techniques, which means careful adjustments in device fabrication.[75–78] Intrinsic degradation, on the other hand, is provoked by the degradation of the organic compounds contained in the device layers.[78,79]

As the principle of OLED's work is through the application of electric current, it is important to understand the processes that occur in the emitter compounds under applied voltage. As a result of the combination of spectral techniques and electrochemical measurements, we can accompany the formation of charge carrier species through their characteristic spectral changes and, in this way, investigate the possible degradation routes that may take place.[29]

There are many possible combinations between spectroscopy techniques with electrochemical systems. One of the simplest combinations is the Spectroelectrochemistry UV-Vis, where the coupling of an electrochemical potentiostat and UV-Vis spectrometer allows to notice changes in the absorption characteristics of the emissive materials while applying voltage (potential difference), examining the absorption spectra of the electrogenerated products and characterizing the charge carrier species.[73] Inside the UV-Vis cuvette, the counter and reference electrodes are introduced together with a transparent WE, usually an ITO coated glass, so that the light beam can pass through and analyze the electrochemically produced species, as can be seen in Figure 13.
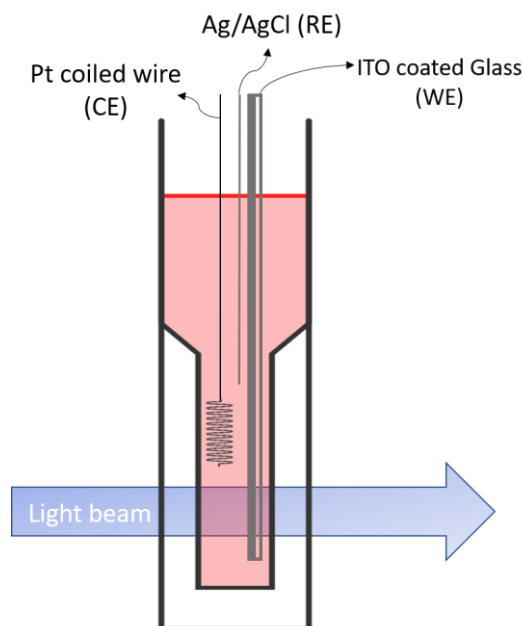
Figure 13. Cell for spectroelectrochemical UV-Vis measurements.

Additionally, Electron Paramagnetic Resonance (EPR) technique has the power to investigate the presence of unpaired electrons in molecular structures, being able to detect paramagnetic behaviour.[80] From the combination of EPR and voltammetric measurements, researchers can identify and quantify the formation of charge carrier species, monitor the appearance of radical ions, as well as characterize the atoms where these charges are localized.[81,82]

When voltage is applied and an oxidation process occurs, for example, EPR signals appear, attributed to polaron (radical cation) formation. In a common case of analysis of conjugated molecules, which undergo two step reversible oxidation process, if the potential continues to increase, the signal is expected to decrease or disappear due to the formation of bipolarons, which are spinless double-charged species. The unpaired electron of the formed polaron may also interact with the magnetic moment of another atom´s nucleus, causing what is known as hyperfine splitting, which is the split of the spectral lines of the EPR signal. Hyperfine splitting is a characteristic feature dependent on the atom's nature, allowing to detect the location of the formed charge, for example, ^1H presents double splitting and ^{14}N exhibits triple splitting of the signal.[80]

3. Materials and Experimental Methods

The description and explanation of the experimental methods used for this study are herein detailed.

3.1. Organic Compounds

The analyzed organic compounds in this study were synthesized in collaboration with Prof. Youhei Takeda's group at Osaka University, in Osaka, Japan, and Dr Marcin Lindner's group, from the Institut of Organic Chemistry Polish Academy of Sciences, in Warsaw, Poland.

3.2. Sample Preparation

3.2.1. Solution

The organic compounds used in this study were dissolved in solvents with different polarities. To obtain other concentration solutions, the organic compounds were weighed on an analytical scale, and the solvents were added in order to prepare solutions in a concentration range of mM. From those mM solutions, other solutions with a range of concentrations from 100 μM to 1 μM were prepared through dilution.

Solvents acquired: Toluene (TOL) 99+% for spectroscopy Acros Organics, Dichloromethane (DCM) CHROMASOLV® 99.9% Sigma Aldrich and tetrahydrofuran (THF) Romil Pure Chemistry were used without further purification. In addition, for electrochemical and spectroelectrochemical studies, dried tetrabutylammonium tetrafluoroborate (Bu$_4$NBF$_4$) 99% and ferrocene 98% were purchased from Sigma Aldrich and used without further purification.

3.2.2. Solid State

The synthesized compounds were investigated in the solid-state to observe the possible behaviour as active layers in OLED structure. Two matrices were chosen to avoid

possible aggregation, the polymer Zeonex® 480R was selected as the study stage between solution and solid-state and 4,4′-bis(*N*-carbazolyl)-1,1′-biphenyl (CBP) was chosen as the host for OLED. Solid-state samples were prepared at a 1% w/w ratio in Zeonex® host and a 10% w/w ratio in CBP host on sapphire disc windows as substrates.

Spin-coated films were prepared using the Spin-Coater Laurel WS-650Mz-23NPPB. The parameters (spinning time, acceleration, speed) were optimized for each different solvent. The sapphire substrate was placed in the Spin-coater. A vacuum pump connected to the equipment ensured that the substrate stayed in place, the optimized parameters were applied, and 100 μL of different solutions were dropped on the top of the substrate as soon as the spinning had begun. This method produces very uniform films.

Drop-coated films result from the drop onto the substrate while it is warmed up with the help of a hot plate. The applied temperature and time are different for each solvent and compound used in each case, CBP, for example, degrades if it undergoes temperatures higher than 50 ℃.

3.3. Steady State Measurements

3.3.1. Optical Absorption

Steady-state UV-Visible absorption spectra were recorded by a HP 8453 (Agilent) spectrophotometer using a 10mm cuvette.

3.3.2. Photoluminescence Spectroscopy

Steady-state emission spectra were recorded on a FluoroSENS spectrometer.

Solvatochromism studies were performed by analysing emission spectra in three different solvents.

The oxygen effect was investigated in solution through degassing experiments in toluene solvent using a custom made 1 cm path-length degassed cell stoppered with a Young tap and degassed using five freeze/thaw/pump cycles. The solid-state degassing measurements were performed in a liquid N_2 cryostat (Janis Research).

The PLQY was determined with the help of an integrating sphere coupled with the FluoroSENS equipment.

3.4. Time-Resolved Spectroscopy

3.4.1. Time-Gated Acquisition (iCCD)

Phosphorescence, PF and DF time-resolved spectra and fluorescence decay curves were collected using picosecond gated luminescence and lifetime measurements (from 400 ps to 1 s) using either third harmonics of high energy pulsed DPSS laser emitting at 355 nm (Q-Spark-A50). Emission was focused on a spectrograph and detected on a sensitive gated iCCD camera (Stanford Computer Optics) with sub-nanosecond resolution. Temperature photophysical measurements were conducted in the Janis CCS-450 closed-cycle helium cytostatic system (CTI-Cryogenics).

The delay and integration times are set at a time longer than the previous sum of delay and integration time to avoid overlap. As the next step, the curve is corrected by integrating the measured spectra to obtain a good luminescence decay profile. Every point represents the collected emission spectra of the respective emitting specie.

3.5. Electrochemistry

3.5.1. Cyclic Voltammetry

In this study, electrochemical measurements were carried out using a three electrodes electrochemical cell, using a platinum (Pt) disk electrode as WE, a Pt wire as CE, and a silver/silver chloride (Ag/AgCl) electrode as RE (calibrated against ferrocene), Bu_4NBF_4 as an electrolyte, and DCM as a solvent, under Argon (Ar) inert atmosphere, connected to potentiostats Biologic SP150 or CHI620 (CH Instruments), under $50 mVs^{-1}$ scan rate.

The energy levels of frontier orbitals, HOMO (E_{HOMO}) and LUMO (E_{LUMO}), associated to the Ionization Potentital (IP) and Electron Affinity (EA), which were estimated from oxidation (E_{ox}) and reduction (E_{red}) potentials, respectively, using the following equations: $E_{HOMO} = E_{ox} + 5.1$; $E_{LUMO} = E_{red} + 5.1$.

3.5.2. UV-Vis Spectroelectrochemistry

The UV-Vis spectroelectrochemical investigation was carried out using a quartz cuvette with a 2 mm optical path, ITO coated glass as WE, Ag/AgCl electrode as RE (calibrated against ferrocene) and a Pt coil as RE, with the help of a Potentiostat Autolab PGSTAT20 and Ocean Optics spectrometer with QE6500 and NIRQuest detectors. The solutions containing the analyzed compounds, electrolyte and solvent were placed into the cuvette, together with the ITO, Pt and Ag/AgCl electrodes. In the case polymer analysis, the ITO containing the polymeric film was placed into the cuvette along with CE, RE and electrolyte solution. The whole system was submitted to five electrochemical cycles at a 50 mV s^{-1} scan rate while UV-Vis and NIR spectra were recorded every 0.5 seconds in a potentiodynamic system.

It is important to mention that the WE used in this technique is ITO coated glass. There are some limitations caused by the stability of the ITO material upon a particular potential. In this case, spectroelectrochemical UV-Vis is only used to determine oxidation processes with potential values up to 1.1 V *vs.* ferrocene.

3.5.3. Potentiostatic EPR

Potentiostatic EPR analyses were performed by a JES-FA 200 (JEOL) spectrometer, and a Potentiostat Autolab PGSTAT20 controlled the potential difference. The compounds' solutions were placed in a custom made cuvette, with 1 mm diameter Pt wire as WE, Ag wire as RE (calibrated against ferrocene) and Pt coil as RE. EPR spectra were recorded stepwise, every 100 mV, to fully characterize the compounds' charge carrier species.

3.6. Devices Assembly

3.6.1. Electrochromic Devices

Electrochromic devices are electrochemical cells containing two electrodes separated by electrolyte ions. For the observation of colour and intensity changes in emission, optically transparent ITO coated glasses are used in this case.[83]

Thin films of the emitters were prepared onto the ITO's surface using a drop-coating technique for small molecular weight compounds. Next, polymeric films were formed onto the ITO's surface under electropolymerization. Prepared films exhibit 1 cm^2. Finally, electrolyte gel, formed by Lithium perchlorate (LiClO$_4$) and poly(methyl methacrylate) (PMMA) dissolved in propylene carbonate, was added on top of the emitters' films. To close the electrochromic cell, another ITO was placed on top of the electrolyte gel, and the whole arrangement was encapsulated with UV resin.

LiClO$_4$ 99.99% was purchased from Sigma Aldrich, PMMA (M.W. 35,000) from Acros Organics, propylene carbonate from Aldrich and UV RESIN XNR 5570-B1 was acquired from Nagase ChemteX Corporation.

3.6.2. Electroluminescent Devices

Different chapters in this study present slight variations in device composition.

Electroluminescent devices in Chapter 5 were fabricated using HAT-CN (1,4,5,8,9,11-Hexaazatriphenylenehexacarbonitrile) as HIL, NPB (*N,N′*-di(1-naphthyl)-*N,N′*-diphenyl-(1,1′-biphenyl)-4,4′-diamine) as HTL, TPBi [2,2',2"-(1,3,5-Benzinetriyl)-tris(1-phenyl-1-H-benzimidazole)] as ETL. Lithium fluoride (LiF) and aluminium (Al) were used as cathode electrode and CBP (4,4′-bis(*N*-carbazolyl)-1,1′-biphenyl) was chosen as host for all emitters.

In Chapter 6, the devices were assembled with NPB as HTL and HIL, TPBi as ETL, LiF and Al as a cathode electrode, with 10% of the emissive compounds dispersed in the CBP host.[10]

OLEDs from Chapter 7 were fabricated with NPB as HIL and HTL, TSBPA (4,4'-(Diphenylsilanediyl)bis(*N,N*-diphenylaniline)) as EBL, TPBi as ETL and LiF and Al as cathode electrode.[82]

In all cases, organic semiconductors and aluminium were deposited at a rate of 1 Ås^{-1}, and the LiF layer was deposited at 0.1 Ås^{-1}. All materials were purchased from Sigma Aldrich or Lumtec and were purified by temperature-gradient sublimation in a vacuum. OLEDs have been fabricated on pre-cleaned, patterned ITO coated glass substrates with a sheet resistance of 20 Ω/sq and ITO thickness of 100 nm. All small molecules and cathode layers were thermally evaporated in a Kurt J. Lesker SuperSpectros 200 evaporation system under pressure of 10^{-7} mbar without breaking the vacuum. The sizes of pixels were 4 mm^2, 8 mm^2 and 16 mm^2. Each emitting layer has been formed by co-deposition of dopant and host at the specific rate to obtain 10% content of the emitter. The characteristics of the devices were recorded using a 6-inch integrating sphere (Labsphere) inside the glovebox connected to a Source Meter Unit and Ocean Optics USB4000 spectrometer.

4. Investigation of Impact of C-C Bond Insertion in Donor-Acceptor Structures

4.1. Introduction

Research studies seeking TADF emission rely strongly on compounds presenting D-A or D-A-D frameworks. The extensive use of D-A molecules is explained because such systems allow the extent of control of overlap between the frontier orbitals involved in the transition leading to the compounds' excited states. Minimum overlap implies a spatial separation of HOMO and LUMO, which are mostly placed on the donor and the acceptor moieties, respectively.[9]

Therefore, energy absorption in such structures induces electron density transfer from donor to acceptor's part of the molecule, resulting in CT excited states. The detection of CT states involved in emission processes is characteristic of most TADF materials investigated so far.[49] Molecular structures presenting strong intramolecular CT character besides achieving HOMO and LUMO separation usually exhibit a small energy split between S_1 and T_1 excited states (ΔE_{ST}), which is one of the most important requirements for the observation of TADF behaviour.[50]

The obtention of small ΔE_{ST} is not the only achievement in the structural point of view when using D-A or D-A-D systems, the conformational angle between donor and acceptor moieties has a strong influence on the observed overall emission, allowing to promote or quench TADF emission, for example. Chen *et al.* noticed that the simple change in position of a methyl group substituent, from donor to acceptor group, leads to entirely different emission pathways, from RTP to TADF.[15] Okazaki *et al.* demonstrated how the application of mechanical forces produced many distinct conformers for the same D-A-D molecule, resulting in emissions varying from red to orange, yellow and even green.[52]

A better understanding of D-A systems and the photophysical properties involved in TADF behaviour is important for designing and developing novel and improved materials. With that in mind, compounds "A" and "B" were synthesized by Dr Marcin Lindner's group, situated at the Institute of Organic Chemistry Polish Academy of Sciences in Warsaw – Poland. Both compounds contain the same acceptor and donor

moieties, the only difference between them is incorporating an extra bond in "B"'s structure, as seen in Figure 14.
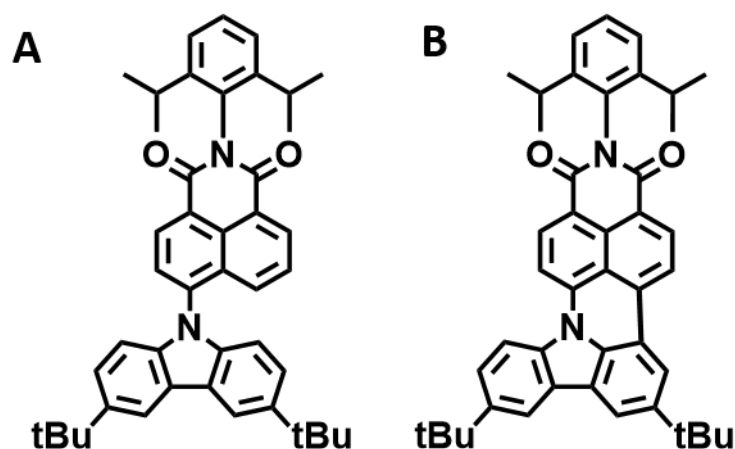
*Figure 14. Molecular structures of D-A compounds **A** and **B**.*

Compound "A" presents a molecular structure with the possibility of free rotation around the C-N bond between donor and acceptor. However, the presence of an extra bond in compound "B" hampers the mobility of the *tert*-butylcarbazole donor group, forcing a more strict configuration and most likely increasing the electron conjugation along with the molecular structure.

These compounds were characterized by electrochemical, UV-Vis spectroelectrochemical and potentiostatic EPR measurements. Additionally, a complete photophysical study was carried out to investigate the radiative pathways involved in compounds "A" and "B" emission, disclosing the influence of the appropriate angular position between donor and acceptor moieties in the emergence of TADF behaviour.

4.2. Results and Discussion

4.2.1. Electrochemical Studies

The Cyclic Voltammetry (CV) technique was used for the electrochemical investigation of compounds "A" and "B", and the acquired voltammograms are displayed in Figure 15.
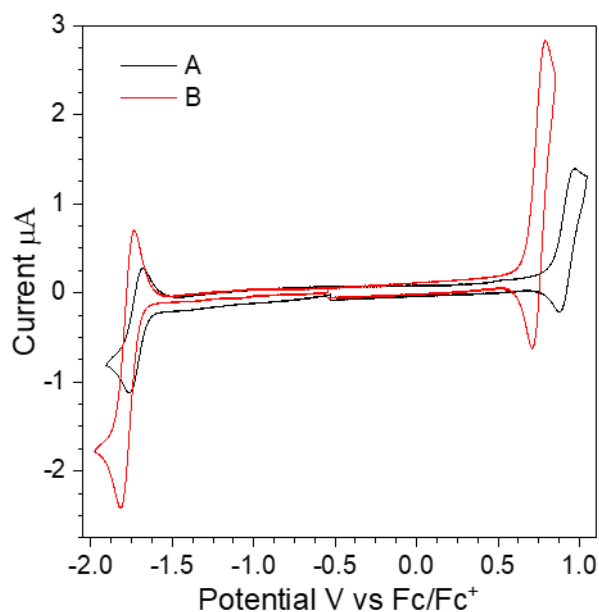
*Figure 15. Cyclic voltammograms of 1 mM of compounds **A** (black) and **B** (red) in DCM containing 0.1 M Bu₄NBF₄ as electrolyte. With Pt disk working, Pt wire as counter and Ag/AgCl as reference electrodes, at 50 mv s-1 scan rate.*

Both compounds display good stability during the measurement of multiple scans, each exhibiting only one reduction and one oxidation process. As shown in Figure 15, the potential of the reduction peaks is very similar. At the same time, the most significant difference noticed in the voltammograms is given by the oxidation potentials of "A" and "B", being 0.97 and 0.79 V, respectively.

From these CV measurements, the energy levels of HOMO and LUMO were determined for compounds "A" and "B", as shown in Figure 16.
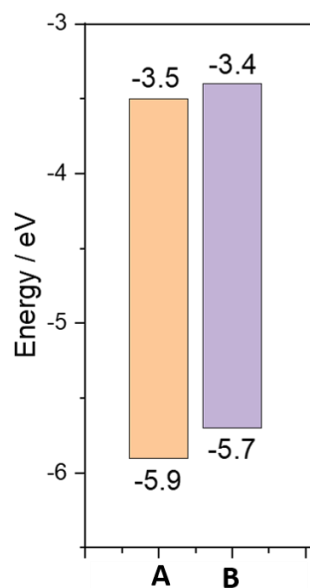
*Figure 16. Diagram of HOMO and LUMO energy levels of compounds **A** and **B**.*

A slightly smaller energy bandgap is observed for compound "B", leading to the conclusion that the configuration induced by the presence of an extra bond between donor and acceptor moieties, increasing the conjugation of the whole structure, affects mainly the HOMO, reducing its energy by increasing of molecule conjugation length.

4.2.2. Spectroelectrochemistry UV-Vis-NIR

To characterize the charge carrier species of compounds "A" and "B" and investigate by-products that side reactions may produce, spectroelectrochemical measurements were carried out by coupling a UV-Vis-NIR spectrometer and a potentiostat. The acquired spectra are displayed in Figure 17. It is important to remember that ITO as WE limits the study to observing only oxidation, but not reduction processes.
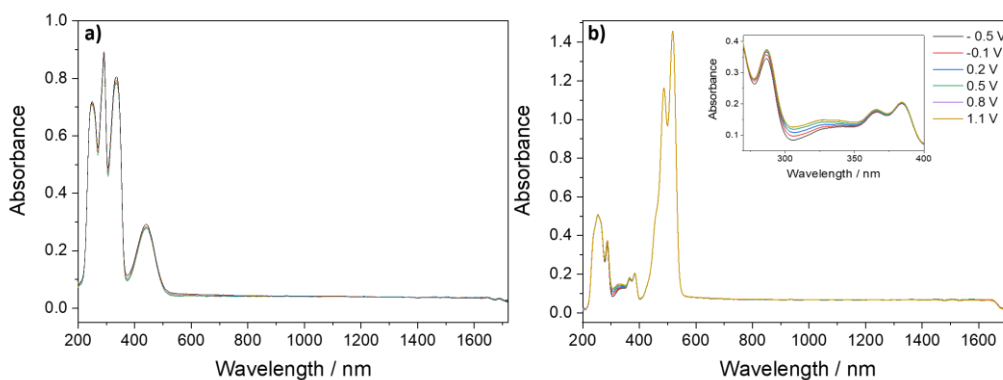
Figure 17. Potentiodynamic UV-Vis-NIR spectroelectrochemical analysis of doping process during oxidation of compounds a) "A" and c) "B". Measurements were carried out using 0.25 mM of compounds in DCM Bu$_4$NBF$_4$ (0.1 M) electrolyte, with ITO as working, Pt wire as counter and Ag/AgCl as reference electrodes, at 50 mv s^{-1} scan rate.

There are no noticeable changes in spectra of compound "A" (Figure 17a) during UV-Vis spectroelectrochemical measurements. On the other hand, compound "B" presents the rise of a band around 320 nm in the doping process (Figure 17b), which stays stable during dedoping.

UV-Vis-NIR absorption can also characterize the optical bandgap, attributing the least energetic band (highest wavelengths) to the least energetic electronic transition at the neutral species' spectrum. A comparison between bandgap values obtained by CV and UV-Vis measurements are depicted in Table 1.

*Table 1. Comparison between electrochemical and optical bandgaps of compounds **A** and **B**.*

Compounds	Electrochemical bandgap /eV	Optical bandgap /eV
A	2.47	2.45
B	2.37	2.29

In CV measurements, the reduction and oxidation processes consist of adding or removing electron(s) from the frontier orbitals, LUMO and HOMO. In this way, the electrochemical bandgap is acquired by the energy required for the ionization process to

occur. During UV-Vis-NIR spectroscopic measurements, the use of photoexcitation generates electron-hole pairs (excitons), which combine and give origin to excited states. The energy difference between ground and excited states is the optical bandgap. Due to the solvation and Coulombic effects, it is impossible to expect a straightforward comparison between optical and electrochemical bandgaps.[84]

4.2.3. Potentiostatic EPR

To complement the spectroelectrochemical UV-Vis and NIR studies and fully characterize the formation of charge carries species, potentiostatic EPR measurements were carried out for compounds "A" and "B" (Figure 18). During stage of the oxidation (Figure 18a), compound A exhibits the appearance of a signal related to charge formation at 1.1 V. Perhaps that is why there were no changes noticed in spectra during UV-Vis spectroelectrochemical measurements. The hyperfine split signals represent the formation of charge in different nitrogen atoms, indicating that distinct conformations contribute to stabilising such positive charge, formed through the oxidation of compound "A". The appearance of an EPR signal occurs at 1.1 V, which increases until the end of the doping process (Figure 18a), followed by a decrease and almost disappearance during dedoping (Figure 18c).

Compound "B" displays the emergence of a signal, referring to the formation of paramagnetic species at 0.7 V (Figure 18b). Such a signal becomes very intense through the doping stage, and even after a slight decrease caused during dedoping (Figure 18d), it stays stable even after the end of the analysis. The same good stability of the charge carrier species was also observed during UV-Vis spectroelectrochemical studies.
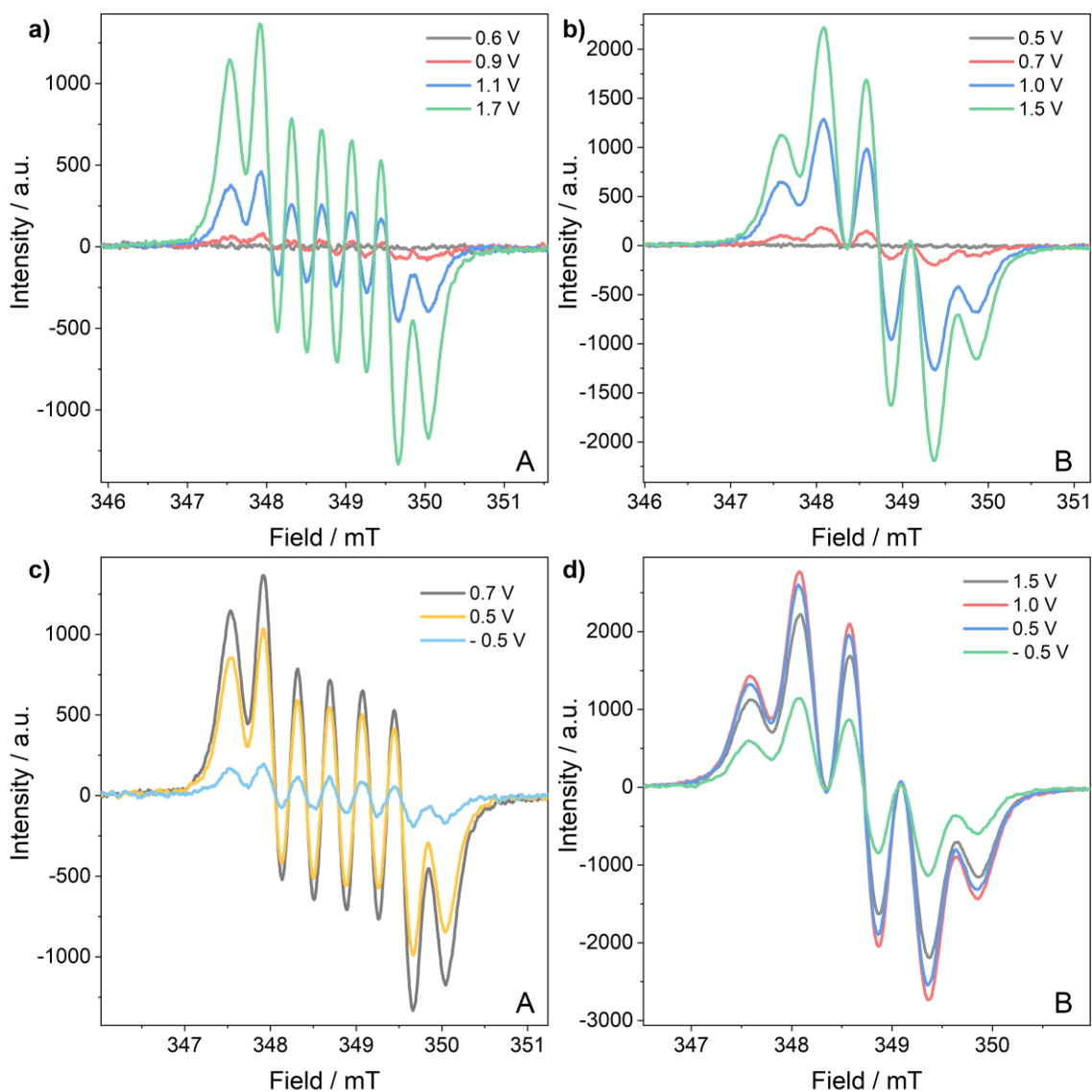
Figure 18. Potentiostatic EPR spectroelectrochemistry of oxidation processes during doping of compounds a) "A", b) "B", and dedoping of c) "A" and d) "B". Pt wire working, Pt wire as counter and Ag/AgCl as reference electrodes, at 50 mv s^{-1} scan rate.

Moreover, EPR spectra acquired during the reduction of materials "A" and "B" are displayed in Figure 19. The two compounds present the emergence of low-intensity signals with hyperfine splitting during the doping process (Figures 19a and 19b). However, through the dedoping of compound "B" (Figure 19d), the EPR signal undergoes a sudden rise of 5x its intensity, followed by a rapid decrease at 1.5 V and higher potentials. In both cases, "A" and "B", signals disappear at the end of the dedoping processes (Figures 19c and 19d).
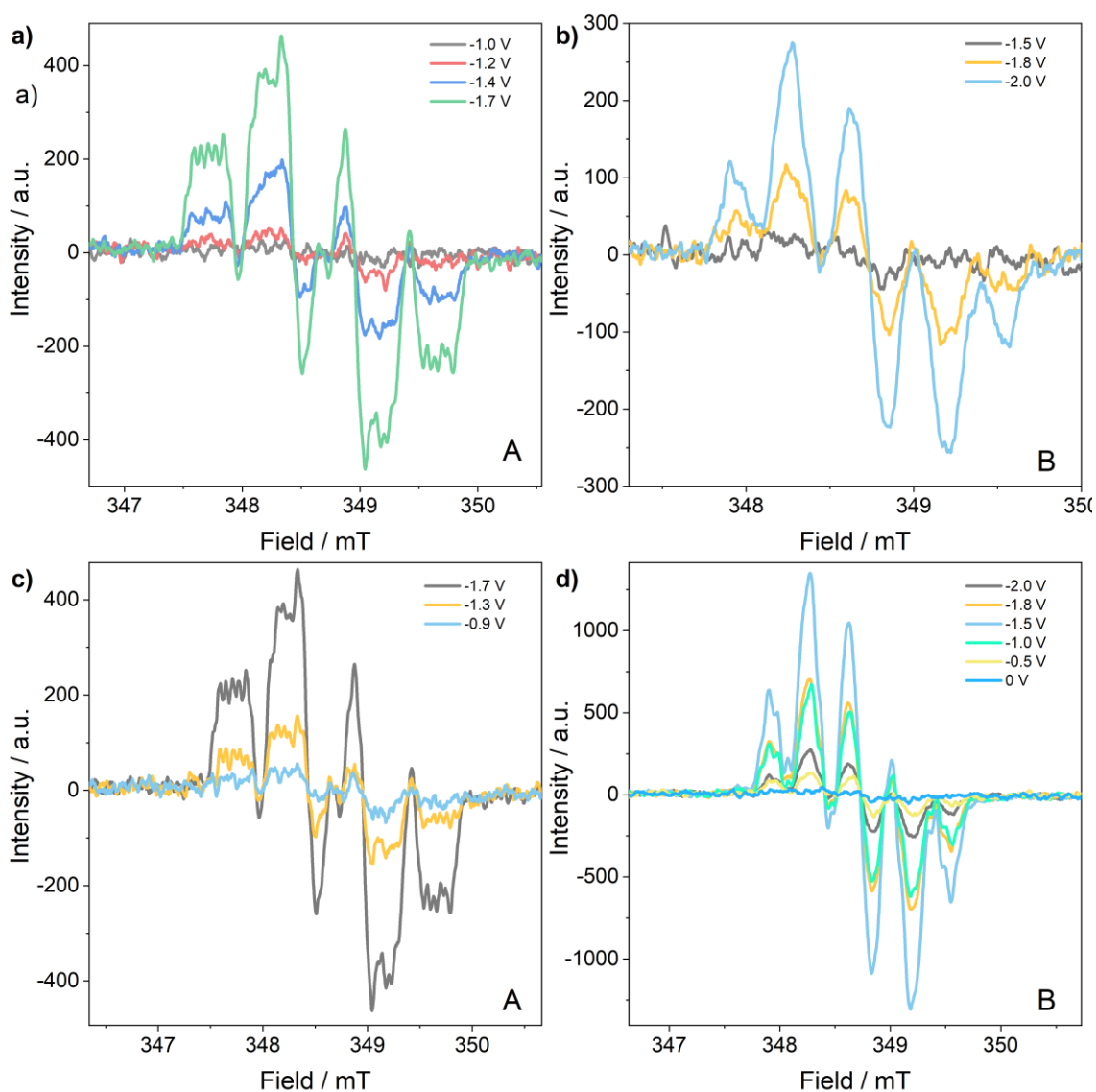
Figure 19. Potentiostatic EPR spectroelectrochemistry of reduction processes during doping of compounds a) "A", b) "B", and dedoping of c) "A" and d) "B". Pt wire working, Pt wire as counter and Ag/AgCl as reference electrodes, at 50 mv s⁻¹ scan rate.

4.2.4. Photoluminescence

The first step of photophysical characterization is UV-Vis absorption measurements (represented as dotted lines in Figure 20) to be able to characterize the electron transition that requires the least amount of energy, located at the highest wavelengths. Such transitions are most likely to occur and are most likely related to the emission transition.
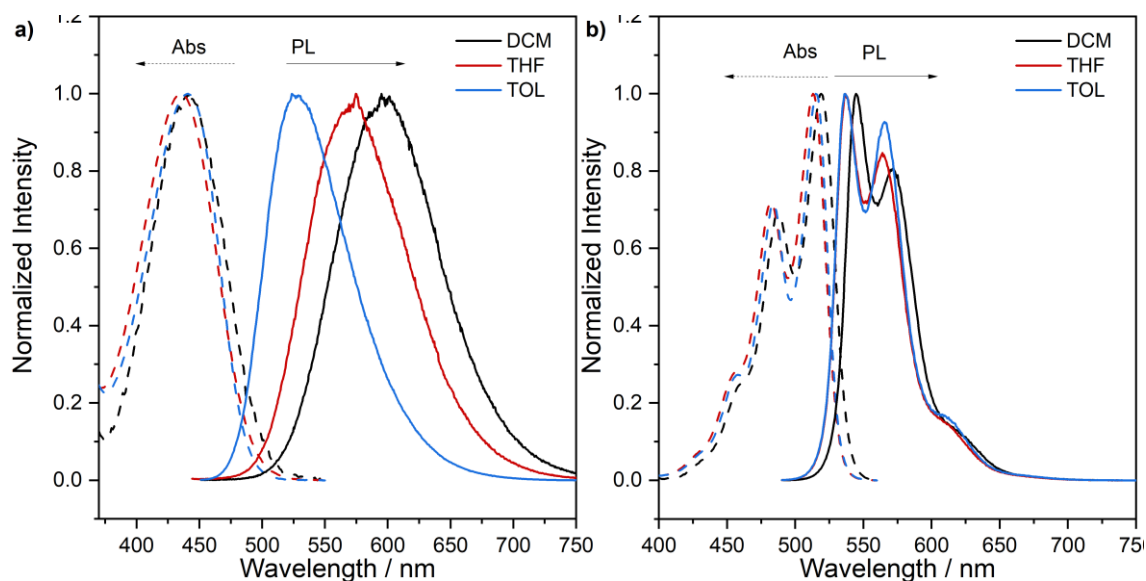
*Figure 20. UV-Vis absorption (dotted lines) and photoluminescence (PL) (solid lines) spectra of 100 μM solutions of (a) **A** and (b) **B** in three different organic solvents (λ_{ex} = 355 nm).*

The solvatochromism study consists of the analysis of emission spectra in solvents of different polarity. Through the acquired photoluminescence spectra, noticed as solid lines in Figure 20, it is possible to observe a significant difference in the behaviours of both compounds. For example, spectra of compound **B** (Figure 20b) diluted in DCM, THF and toluene exhibit similar emission wavelength, while compound **A** (Figure 20a) displays a red shift with increasing solvent polarity. Such shift is characteristic of the presence of ICT excited states involved in the radiative decay.

Through the emission spectra analysis under a degassed environment, it is possible to detect the presence of triplet exited states involved in the radiative emission. Figure 21 displays the comparison of emission spectra of compounds "A" and "B" in the presence of oxygen (in black) and under vacuum (in red) conditions.
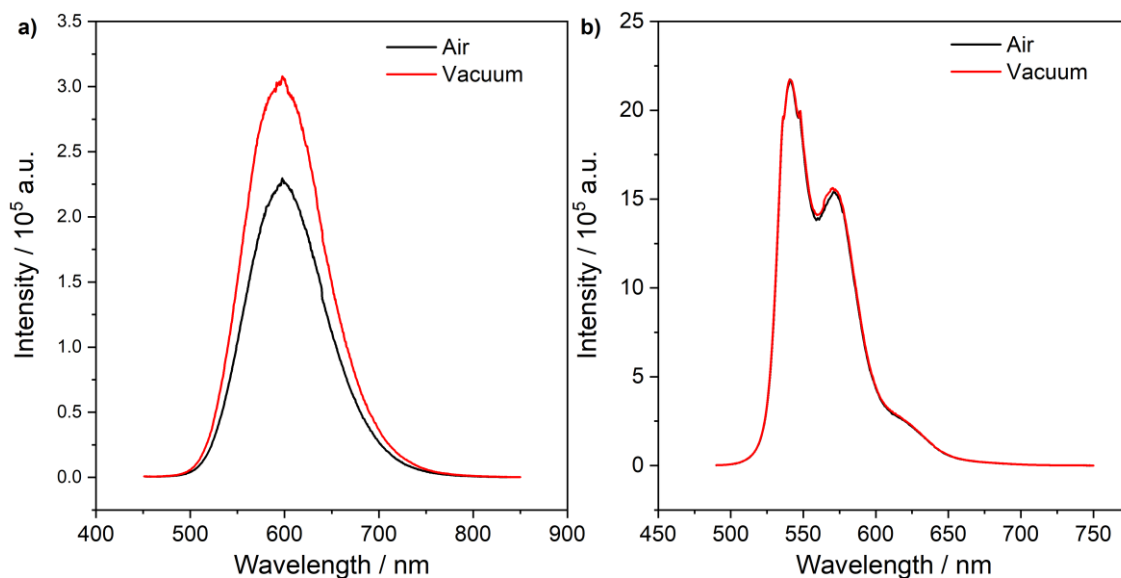
*Figure 21. Emission spectra of compounds a) "A" and b) "B" under airy (black) and vacuum (red) conditions. Solid samples contain 1 wt% of compound **A/B** in Zeonex®️ matrix (λex = 355 nm).*

Compound "B" presents no change in emission between airy and degassed environments. In contrast, compound **A** shows a significant increase (1.3x) of emission intensity, which correlates with the solvatochromism study indicating the possibility of a delayed fluorescence behaviour.

4.2.5. Time-Resolved Spectroscopic Analysis

Using a He cryostat and an iCCD-gated camera, phosphorescence spectra of the two compounds were measured at 10 K. Prompt fluorescence measurements are obtained at room-temperature (300 K). Through the analysis of the acquired spectra (Figure 22) and especially from the onset (beginning) of phosphorescence and fluorescence emission signals, the energy of triplet and singlet excited states are calculated, respectively.
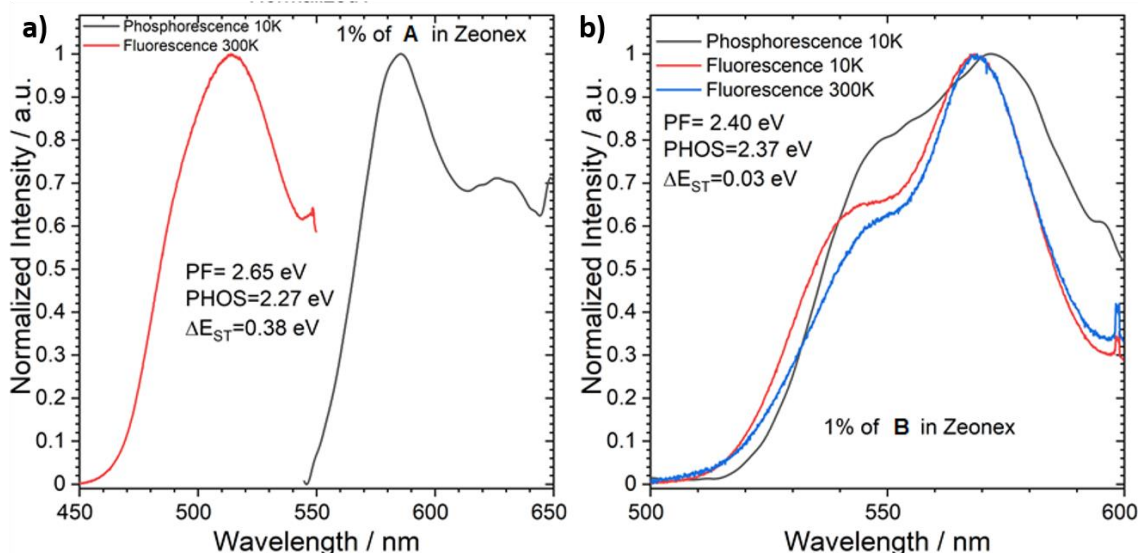
*Figure 22. Time-resolved spectra of 1 wt% of compounds a) **A** and b) **B** in Zeonex®*
matrix, at varying delay times at 300 K and 80 K.

Compound "B" (Figure 22b) presents a very small ΔE_{ST} value (30 meV), while the calculated bandgap for compound "A" (Figure 22a) is 10 times higher (380 meV). The small energy split for compound "B" is noticed as a close overlap at the beginning of fluorescence and phosphorescence spectra, represented as red and black lines in Figure 22b. While compound "A" exhibits fluorescence and phosphorescence spectra in very distant wavelengths (Figure 22a).

As a result of the plot of emission intensity *vs.* delay times, it is possible to determine the decay times and observe different types of radiative processes, as shown in Figure 23. For example, compound "B" (Figure 23b) displays only one type of radiative decay through prompt fluorescence. However, compound "A" (Figure 23a) exhibits the prompt fluorescence along with phosphorescence and a delayed fluorescence component noticed at the ms range.
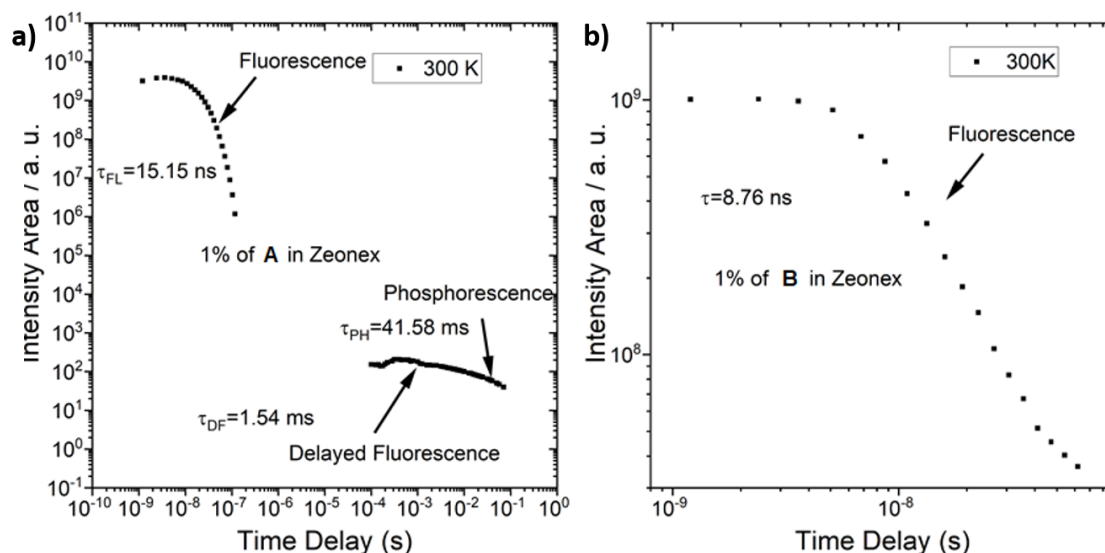
*Figure 23. Transient decay of 1 wt% of a) **A** and b) **B** in Zeonex® matrix at 300 K.*

Compound "A" (Figure 23a) presents a significantly larger value of ΔE_{ST} (380 meV) for the requirements for observing TADF behaviour,[9] although it displays delayed fluorescence emission with a 1.54 ms lifetime. Unfortunately, the ms time regime is considered long-lived to form an efficient OLED device due to the increasing roll-off effect and polaron quenching mechanism in emission processes with significant delay times.

As noticed in Figure 23b, compound "B" is a perfect example that only small values of ΔE_{ST} are not enough to observe delayed fluorescence behaviour. Its rigid conjugated structure does not allow the existence of an ICT state, characteristic of TADF emission. Therefore, as shown in Figure 22b, compound "B" exhibits only prompt fluorescence at 300 K and phosphorescence at extremely low temperatures (10 K) like most common organic emitters.

4.3. Conclusions

The analysis of compounds "A" and "B" resulted in a very didactic comparative study between two molecules containing the same acceptor and donor groups, with only one specific slight difference in structure, leading to different radiative decay pathways.

The investigation of these two compounds confirms the importance of angular position between donor and acceptor moieties to detect TADF emission. Compound "A" exhibited

delayed fluorescence emission due to its more flexible structure, allowing larger oscillation between donor and acceptor moieties, increasing the rate of the charge transfer process. In contrast, compound "B", with a very rigid structure, only presents prompt fluorescence emission at room temperature.

This study demonstrated that although minor energy splitting between the lowest singlet and triplet excited states is an essential requirement for achieving TADF behaviour, without the presence of ICT character, no TADF emission can be observed.

5. Electrochemical and Spectroelectrochemical Properties of Dibenzophenazine Based TADF Emitters

5.1. Introduction

In 2016 and 2017, Prof. Monkman and Prof. Minakata published a collaborative study of a family of dibenzophenazine-based TADF emitters, in a total of seven novel compounds, all containing a donor-acceptor-donor (D-A-D) flexible structure. Where they presented the synthetic route, as well as structural, electrochemical and photophysical characterization of the emitters. Moreover, it revealed a complete study of the TADF properties, detecting very small values of ΔE_{ST}. Finally, these compounds were applied in the manufacture of OLED devices, achieving high EQEs (up to 16.8%). Surprisingly two of these compounds, derived from phenothiazine donor groups, displayed mechanochromic luminescent properties as well. In these studies, it was acknowledged the high influence of the twisted D-A-D structure, and the movement between donor and acceptor moieties, both in the efficiency of TADF emission and in the mechanochromic behaviour.[52,85]

Nevertheless, it failed to disclose the properties of electropolymerization of two of those compounds. Which herein, in this chapter, are studied in detail. The formation of dimers and polymers can cause degradation, increasing roll-off efficiency in OLEDs[10,29], which is the opposite of what we look for in optimising devices.

As presented in Figure 24, in addition to the seven previously published molecules, a novel one was synthesized (compound **5**), containing carbazole donor groups, for a better comparison study. The synthesis was performed by Prof. Takeda's research group at Osaka University in Osaka – Japan.
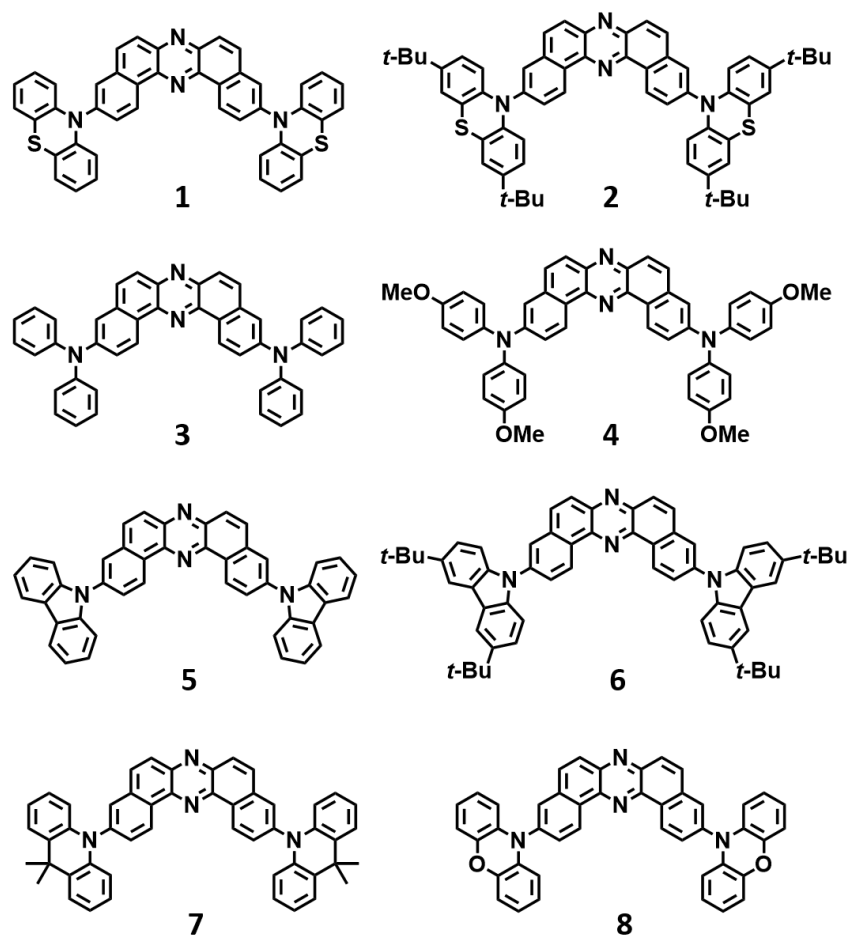
*Figure 24. Molecular structures of compounds **1**-**8** based on the dibenzophenazine core*

From these eight molecules here studied (Figure 24), compounds **3**, **5** and **7** display the ability to undergo electropolymerization reactions. Conducting and semiconducting polymers are widely used in electronic devices.[86–88] The polymeric films can be prepared by different methods such as spin-coating,[89] inkjet printing,[90] drop-casting[91] and electrochemical polymerization (EP).[92] However, electropolymerization has not been employed in the fabrication of OLEDs, although its use affords significant advantages: during the formation of the film, it is possible to control its growth rate and thickness,[93,94] and it is a low-cost process, and in comparison to traditional polymer synthesis, the generation of films is much simpler, although it is hard to result in very uniform films.[95,96]

As discussed before, in the construction of optoelectronic devices, it is important to understand better the nature of the emitter under applied voltage, especially the side reactions that may occur. Those reactions can provide by-products that could interfere with the device's efficiency, causing deterioration of the optical and electronical performances.[29]

One of the disadvantages of the electropolymerization of emitters already applied in OLEDs, in this case, is a result of the high conjugation length in the polymer formed, the product has a planar structure. In a planar configuration, donors and acceptors lose the appropriate angle between each other to achieve TADF properties.[9]

To determine the future applicability in devices, spectroelectrochemical techniques were used to understand better follow-up processes observed in these compounds.

This Chapter presents the full study of electrochemical and spectroelectrochemical properties and electropolymerization behaviour of the dibenzophenazine- based TADF emitters family and the polymers formed. CV measurements were conducted with this series of D-A-D compounds (Figure 24) to study electrochemical properties. Additionally, spectroelectrochemical UV-Vis and potentiostatic EPR investigated the formation of polarons and bipolarons of monomers and polymers.

As almost all compounds used in this study were previously reported for the application of OLED devices,[52,85] all presenting TADF properties yielding considerably good efficiencies, herein in this study, once again, electroluminescent devices were assembled to compare the OLED characteristics of the novel material (compound **5**) with the others already known.

Materials containing electrochromic properties are characterized by the ability to vary colour emission and/or transparency towards the light, resulting from an applied electrical field. When such materials exhibit such variation inside the visible range of spectra, meaning that we can detect such changes with our eyes, they become highly interesting for the application in optoelectronic devices.[83]

Electrochromic devices take advantage of such specific behaviour of colour variations under the application of small currents (1-5 V). Among some types, the most commonly used electrochromic device nowadays is the smart windows, which may control the amount of sunlight that passes through the window glass (or other material) due to a change in transparency caused by the applied voltage.[97] Such new technologies, if right implemented, can reduce extensively the energy costs related to air-conditioning.[83]

In this study, some of the compounds analyzed by UV-Vis spectroelectrochemical measurements presented very interesting active electrochromic properties in the NIR region. These results showed the proof of concept of multi usability of TADF emitters.

In the course of my work, I proved the use of the selected compounds in OLEDs and electrochromic windows. Electrochromic devices were manufactured with compounds **1-8** and the polymers **P3**, **P5** and **P7**.

5.2. Results and Discussion

5.2.1. Electrochemical Studies

The electrochemical behaviour of compounds **1** – **8** was analyzed through CV measurements to evaluate the HOMO and LUMO energy levels, electrochemical bandgap, and stabilization conditions (Figure 25).
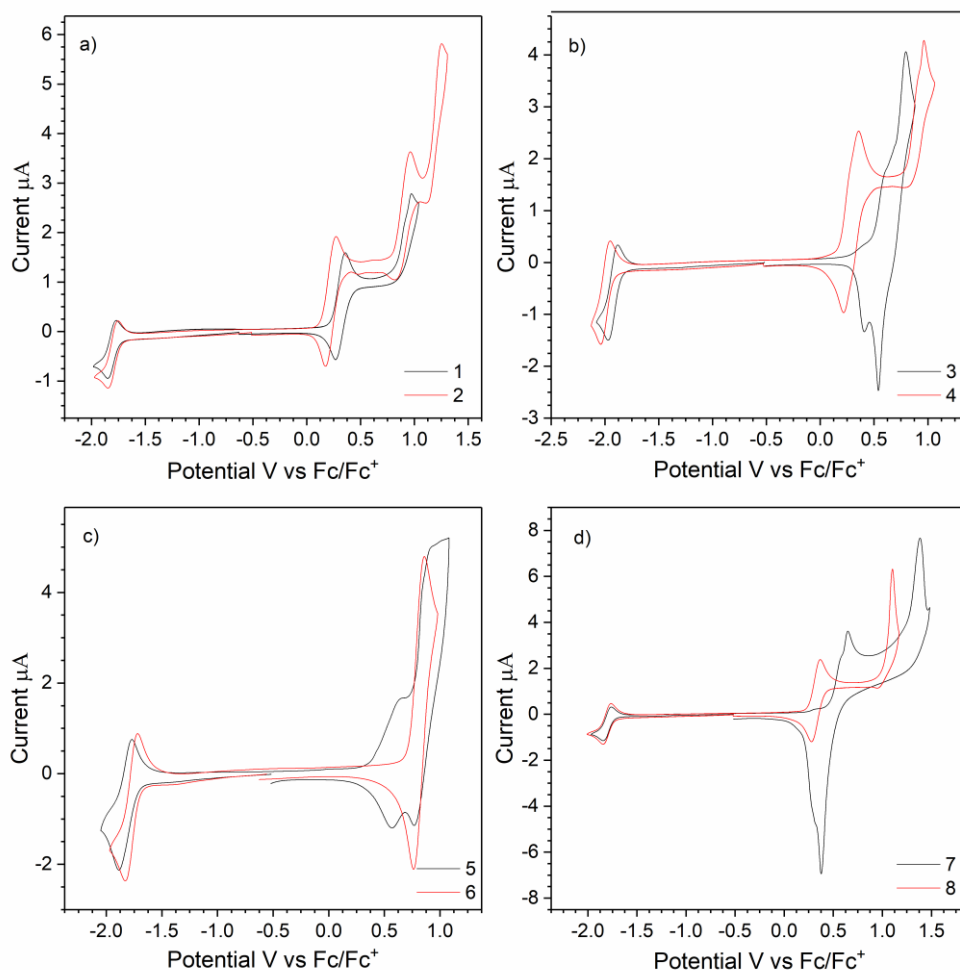
Figure 25. Cyclic voltammograms of 1 mM of compounds a) 1 and 2, b) 3 and 4, c) 5 and 6, d) 7 and 8 in DCM containing 0.1 M Bu₄NBF₄ as electrolyte. With Pt disk

Determining compounds' oxidation and reduction potentials is the first step of electrochemical studies. In Figure 25, it can be observed the first cycle of oxidation and reduction analysis of CV. As it is first noticed, all compounds present only one reversible reduction peak, seen at negative potentials, very similar to each other, representing that the change in donor groups has a very low influence on the electrochemical properties of the acceptor group.

Considering the oxidation signals shown in the positive range of potentials in Figure 25, all compounds present a first oxidation signal with reversible characteristics. Most of them exhibit a second oxidation stage, and compounds 2 and 7 undergo a third oxidation stage. The oddly shaped voltammograms **3**, **5** and **7** are the first indication of electropolymerization processes.

As depicted in Figure 26, black lines represent 10 scan cycles of compounds **3**, **5** and **7**, where it can be noticed in the second and following scans the emergence of new peaks at lower potentials. The emergence of new peaks is evidence of the formation of new species generated from an electrochemical reaction. The lower oxidation potential represents a higher conjugation character than the initial monomer. The constant increase of current between consecutive scans indicates the successful electrodeposition of the materials onto the electrode's surface. The red line in the voltammograms in Figure 26 represents the first scan of the CV measurement of the polymer, in the absence of monomer solution, using the same potential boundaries. We can determine the monomer's and polymer's oxidation potentials and starting polymerization potentials through these measurements.

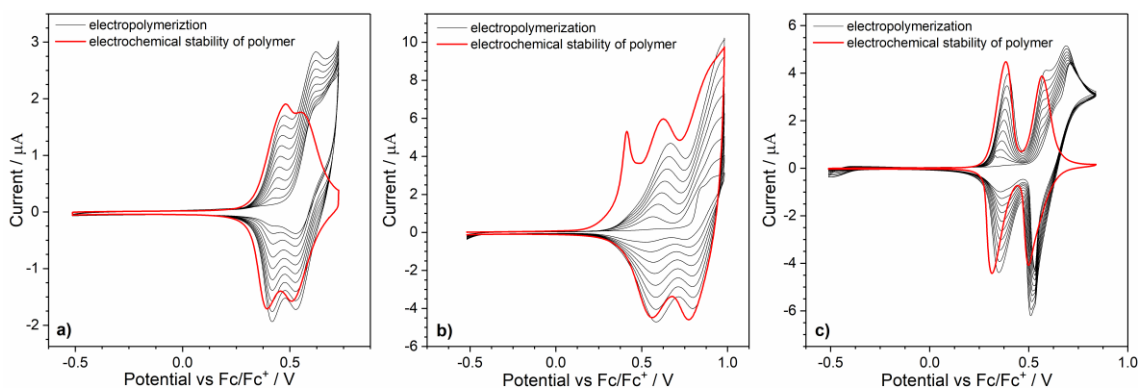*Figure 26. Cyclic voltammograms for the electropolymerization (black line) of 1mM solutions of compounds a) 3, b) 5, and c) 7; and for the oxidation of the polymeric films (red line) formed in the electrode surface. Measurements were carried out in 0.1 M Bu$_4$NBF$_4$ solution in DCM at a 50 mV s-1 scan rate.*

In all cases, the starting polymerization potential was slightly higher than the monomer's first oxidation potential. This indicates that the minimum amount of positively charged species generated from the monomer undergoes an efficient polymerization reaction, producing enough polymeric material to be noticed by the CV technique.

It is essential to mention that the signal at the lowest potential value in Figure 26b is associated with an effect called charge trapping due to the consecutive succession of applied potential cycles on the electrode's surface. However, it only appears in the first scan of the electrochemical stability of the polymer and is not present in all the following scans (2-10), therefore, it is not related to the polymeric material analyzed.

During the first scan of electrochemical analysis of electropolymerizable compounds, the measurement occurs on the bare electrode, and the oxidation signal is referent only to the monomer present in the solution. Through the following steps, being the reverse reduction and the successive cycles, the electrode's surface is covered at least partially by the deposited polymer. At this stage, recorded voltammograms are generated from 10 continuous scans, represented as the black lines in Figure 26.

In another step, after the polymeric films are already deposited on the electrode's surface, the electrode was rinsed with solvent to remove the soluble monomer and placed into an electrochemical cell containing only electrodes and electrolyte solution. The recorded voltammogram of the first oxidation cycle of this stage is displayed as the red lines in Figure 26. The reduction voltammograms of the polymers are shown in Figure 27,

through where it can be determined the electrochemical parameters and stability of the polymer formed.
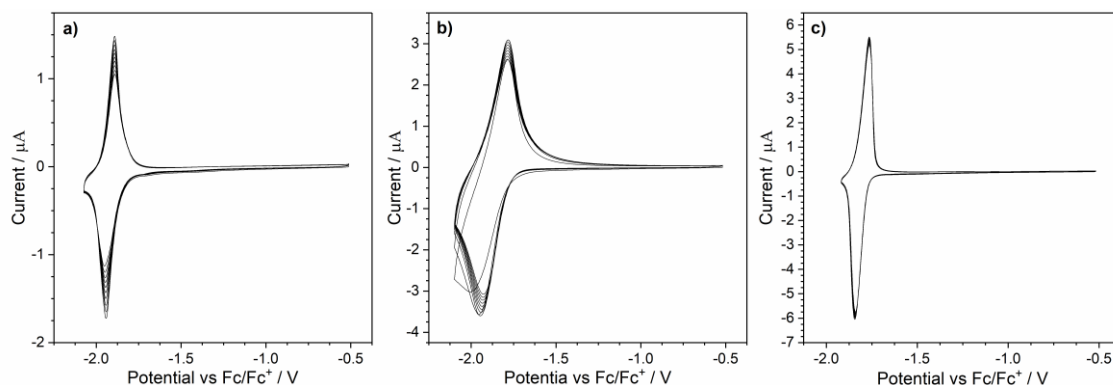
Figure 27. Cyclic voltammograms of the reduction of the polymeric films a) P3, b) P5, and c) P7 in DCM Bu₄NBF₄ (0.1 M) electrolyte.

As a result of the electrochemical investigation, we can determine HOMO and LUMO energy levels and electrochemical bandgap by employing the potential values of the first oxidation and first reduction processes. These values are presented in the diagram in Figure 28.
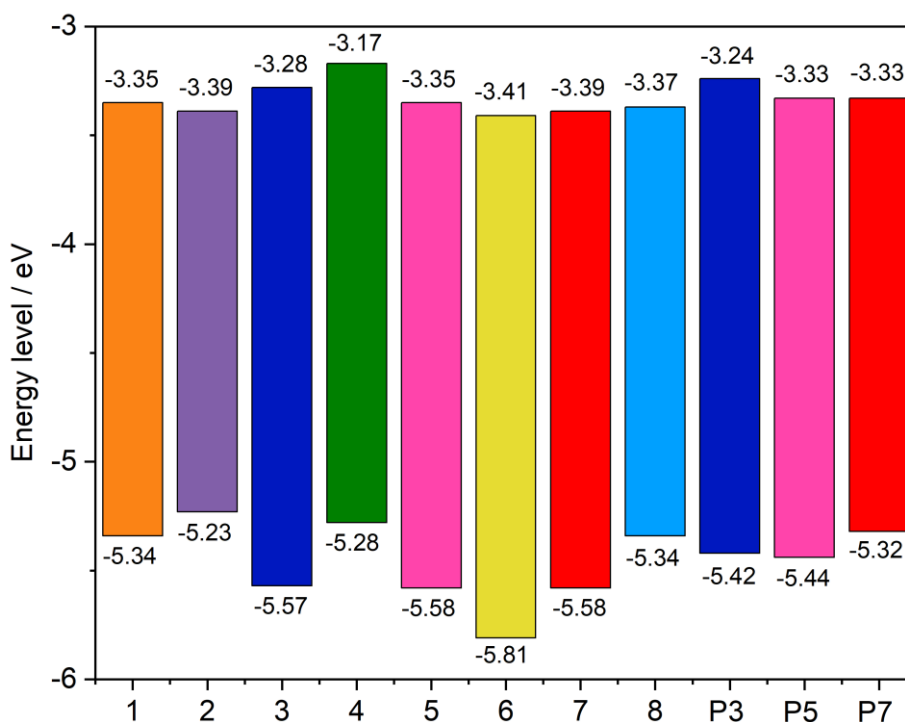
Figure 28. HOMO and LUMO energy levels and electrochemical bandgap values for compounds 1 – 8, and Polymers P3, P5 and P7.

All the compounds share the same acceptor, the dibenzophenazine group. Thus, all the LUMO levels are similar, ranging from -3.17 to -3.41 eV. Furthermore, the highest LUMO value was found for compound **4**, containing diphenylamine derivative with methoxy substituents. In contrast, the lowest LUMO value was attributed to compound **6** with *tert*-butylcarbazole donor groups, followed by compounds **2** and **7**, implying the effect of radical substituents on stabilizing LUMO energy levels.

The smallest bandgaps are from compounds **2** and **5**. Compounds **1** and **8** have very similar LUMO and HOMO energy levels, between all of the compounds, these two are the most identical in molecular structure, the donor group of compound **1** is phenothiazine and compound **8** is phenoxazine, being sulfur and oxygen similar in electronical structures, belonging to the same family in the periodic table.

Higher HOMO energy levels and smaller bandgaps are found for the polymeric materials compared to their precursor monomers, which may be induced by the higher conjugation length, meaning that higher potential values are required for the first oxidation process to occur.

5.2.2. Spectroelectrochemical UV-Vis

The electrochemical analysis provides the potential necessary for the generation of positive and negative charges and for the electropolymerization to start. Furthermore, with the help of spectroelectrochemical techniques, it is possible to characterize the absorption properties of all these species formed during applied potential.

The solution containing the analyzed compounds was submitted to the procedure detailed in Section **3.5.2.** in the previous Chapter of Materials and Experimental Methods.

In electrochemical studies, when the potential is applied up until the selected potential boundary, it is called the doping process. The stage of returning to the initial potential value, as at the beginning of the measurement, can be called the dedoping process.

High concentrations of emitter compound are necessary for this study so that the formation of charge carrier species can be noticed once the spectral changes attributed to these species are not very intense in absorptivity.

The compounds that do not exhibit the ability to polymerize were also analyzed by spectroelectrochemical UV-Vis measurements, as displayed in Figure 29, the doping

(29a, 29b, 29e, 29g and 29i) and dedoping (29b, 29d, 29f, 29h and 29j) processes of compounds **1**, **2**, **4**, **6** and **8**.

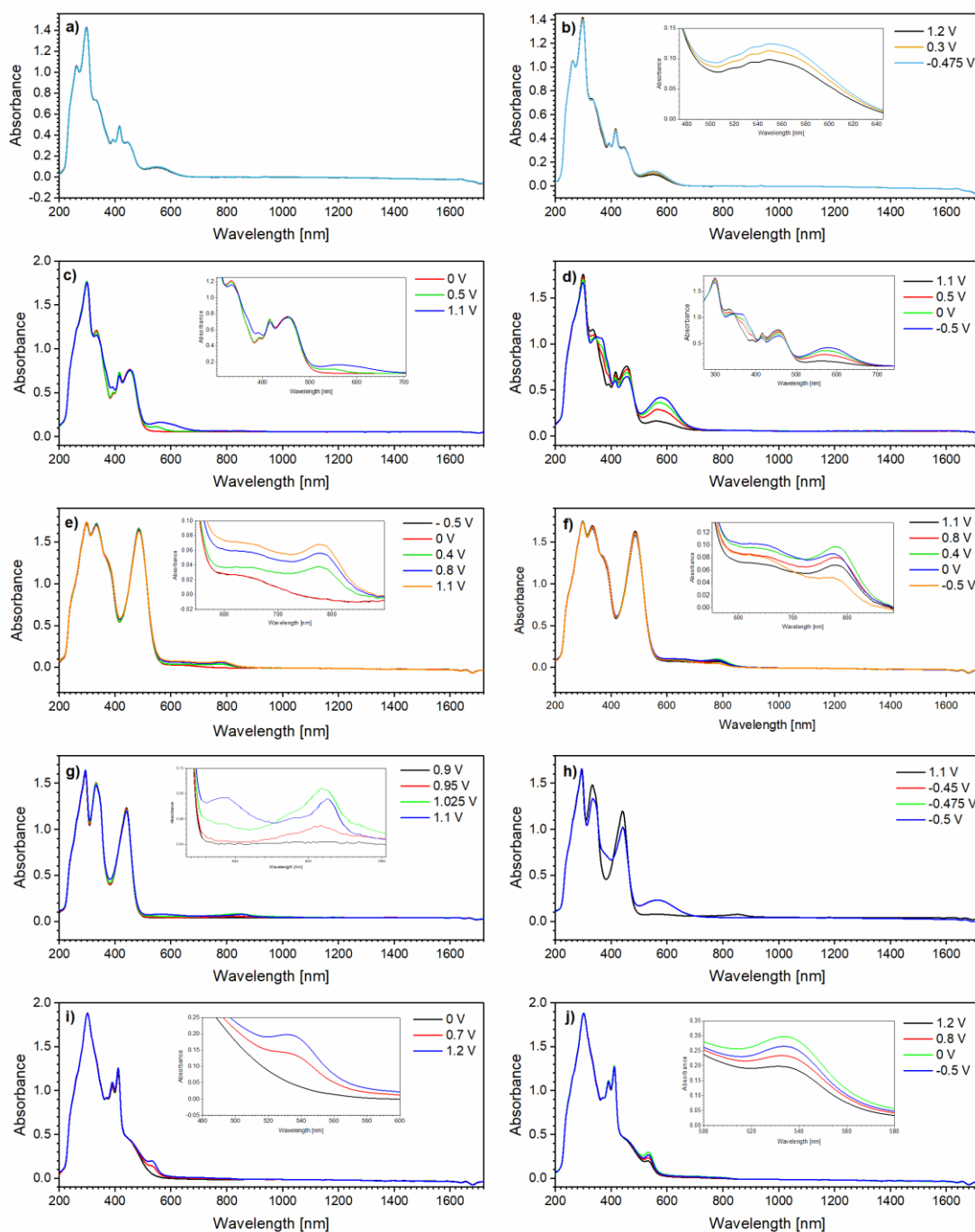*Figure 29. Potentiodynamic UV-Vis-NIR spectroelectrochemical analysis of doping process of compounds a) 1, c) 2, e) 4, g) 6, and i) 8; dedoping process of compounds b) 1, d) 2, f) 4, h) 6 and j) 8. Measurements were carried out using 0.25 mM of compounds in DCM Bu₄NBF₄ (0.1 M) electrolyte, with ITO as working, Pt wire as counter and Ag/AgCl as reference electrodes, at 50 mv s⁻¹ scan rate.*

The spectral changes during the first electrochemical scans of compound **1** are barely noticeable, only in the fifth (and last) cycle a slight increase in the band at 551 nm can be observed during the dedoping in Figure 29b.

For compound **2**, in Figure 29c, during the doping process, it is possible to observe the emergence of a broad band between 500 and 700 nm, which turns into a more defined signal with a maximum of absorbance at 578 nm in the reverse reduction process (Figure 29d). Additionally, in Figures 29c and 29d, we can observe the appearance of two signals together at 350 and 366 nm at the same time that the 334 nm signal decreases until it is barely noticed and becomes the shoulder of those two signals. During the dedoping process, it is possible to observe three isosbestic points at 347, 406 and 484 nm. The presence of an isosbestic point at 986 nm indicates the formation of bipolarons directly from polarons since while the concentration of one decreases, the other increases.

In Figure 29e, we observe the appearance of two signals between 550 and 900nm during the doping process of compound **4**, one more defined signal at 777 nm and another broad band on its left. Such signals slightly increase during dedoping in Figure 29f but begin to decrease until are almost disappeared, characterizing a polaron formed in a reversible system. It is essential to mention that there may be a little delay in the observed processes on such potentiodynamic measurements once everything happens fast, at a scan rate of -0.5 V s^{-1}, and the solution requires time to reach equilibrium.

In the case of compound **6**, during its doping process (Figure 29g), one signal arises around 850 nm up to 1 V, until when at 1.1 V, another signal around 575 nm emerges with very low intensity. Then, it becomes intense during the dedoping process (Figure 29h), and it stays for a while, representing a stable species being formed.

Compound **8** presents only one small spectral change, the appearance of a signal at 534 nm in the doping process (Figure 29i) that increases the intensity during the beginning but starts to decrease at the end of the dedoping process (Figure 29j). Associated with the small reversibility of charge carrier formation leading to a slow process.

On the other hand, compound 3 presents a unique behaviour during spectroelectrochemical studies. As shown in Figure 30, two broad signals appear during the first doping process (Figure 30a), which decrease during dedoping (Figure 30b) until one of the signals, at 780nm, disappears, however, one very defined signal at 618 nm stays stable during all the successive cycles. Developing a very stable signal is associated

with product formation during electrochemical measurement. At the same time, the disappearance of 780 nm signal is noticed, while another broad signal emerges around 1425 nm. These changes are more easily noticeable with the cyclovoltabsorptiometric analysis presented in Figure 30e.

Since there is polymer formation, in this case, any observed spectral changes are always associated with both to monomer's and polymer's charge carriers. Still, it is possible to gather more knowledge about the spectral characteristics of the pure monomer when looking at the behaviour of compound **4** (Figure 29e and 29f), once the molecular structures of **3** and **4** are very similar, having **4** an alkyl group blocking the position where the polymerization could occur. With that in mind, the signal around 780 nm is characterized as the monomer's charge carrier, and the signal around 1425 nm is related to the polymer's charge carrier species.

Figure 30. Potentiodynamic UV-Vis-NIR spectroelectrochemical analysis of doping process of a) 0.25 mM of compound 3 and c) polymer P3; dedoping process of b) 0.25 mM of compound 3 and d) polymer P3 in DCM Bu$_4$NBF$_4$ (0.1 M) electrolyte. Cyclovoltabsorptiometric measurement of e) electropolymerization of 3 and f) electrochemical stability of the polymer P3. With ITO working, Pt wire as counter and Ag/AgCl as reference electrodes, at 50 mv s^{-1} scan rate.

Polymeric films were formed on the ITO's surface, resulting from the first stage of the UV-Vis spectroelectrochemical measurements. The ITO is then rinsed with solvent to remove the monomer compound and placed in a cuvette containing only the electrolyte solution. The second stage of the analysis is the potentiodynamic measurements of the pure polymeric film, the acquired spectra are presented in Figures 30c and 30d.

62

Once the analysis of spectral characteristics of polymerizable compounds is impaired by the presence of the polymer's charge carriers, the polymer's measurements provide a lot more information.

The observed spectral changes are attributed as polaron bands at the initial potential increase. With the continuing increase of the potential, polaron bands start to decrease, and it is observable that another band's appearance at a lower wavelength represents the second stage of oxidation while forming bipolarons.

In Figure 30c, it is possible to notice at the beginning of the doping process the emergence of a polaronic band around 1500 nm, which soon starts to decrease, while at the same time, a band at 762 nm arises, referent to the bipolaronic species. In its neutral form, polymer P3 exhibits two signals in 339 and 485 nm that disappear right after the doping process begins, and at that exact moment, a band in 419 nm appears. The spectra exhibit four isosbestic points at 401, 430, 540 and 980 nm during the doping process. All the spectral changes are more easily tracked using the plot of cyclovoltabsorptiometric analysis in Figure 30f, where it can be observed the full reversibility of the charge carriers formation and the confirmation of the polaronic feature of the signal at 1491 nm, which exists for a short time during both doping and dedoping processes.

The spectroelectrochemical behaviour of Compound **5** is presented in Figure 31. The cyclovoltabsorptiometric plot in Figure 31e displays that the signal around 790 nm appears at the end of the doping process and disappears through the dedoping. Such a signal can be observed as a broad band arising in Figure 31a. During the dedoping stage (Figure 31b), the appearance of a new band is noticed at 541 nm, which stays stable through the successive cycles. This stable signal is an indication of the electropolymerized product.
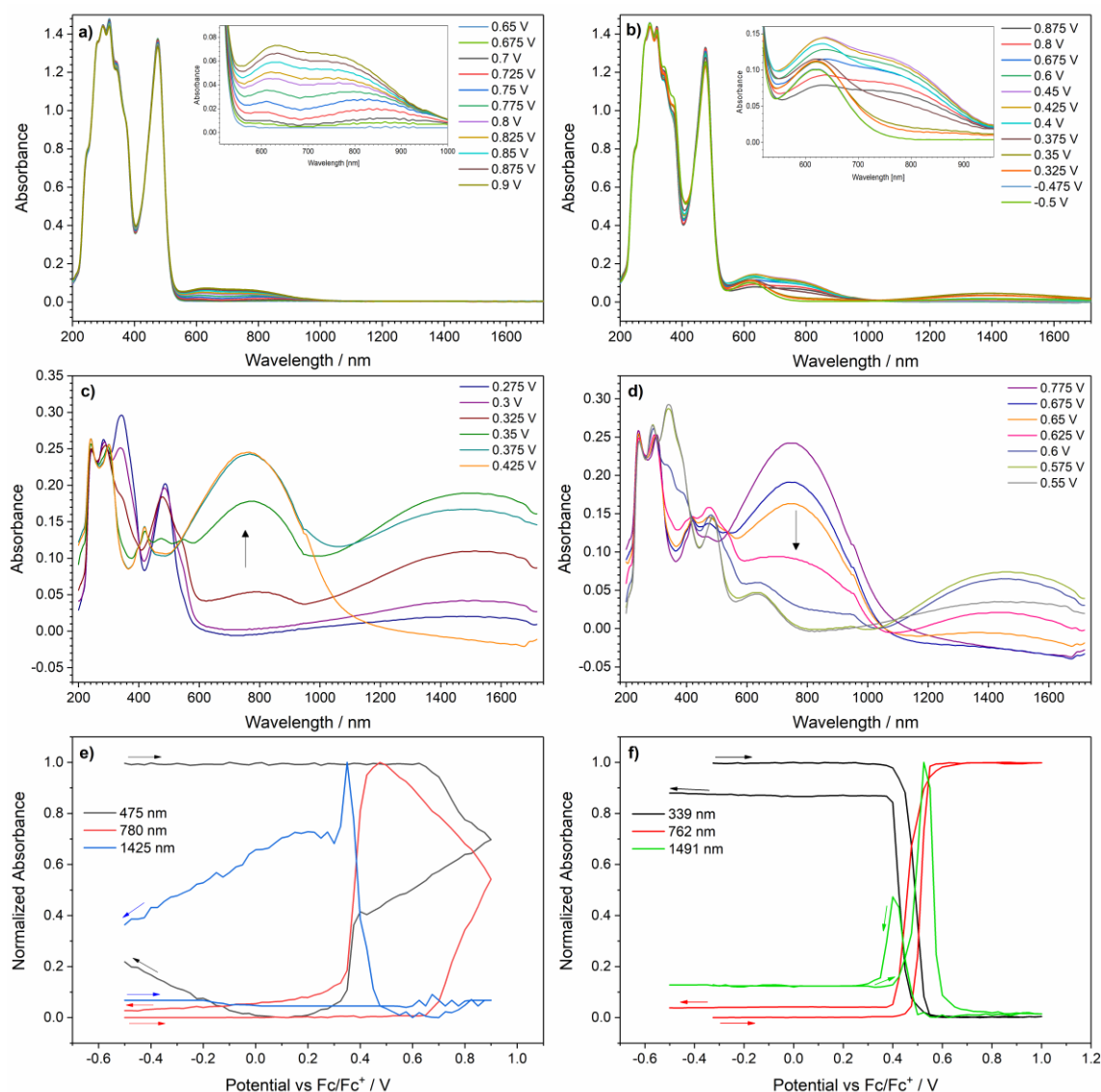
Figure 31. Potentiodynamic UV-Vis-NIR spectroelectrochemical analysis of doping process of a) 0.25 mM of compound 5 and c) polymer P5; dedoping process of b) 0.25 mM of compound 3 and d) polymer P5 in DCM Bu$_4$NBF$_4$ (0.1 M) electrolyte. Cyclovoltabsorptiometric measurement of e) electropolymerization of 5 and f) electrochemical stability of the polymer P5. With ITO working, Pt wire as counter and Ag/AgCl as reference electrodes, at 50 mv s^{-1} scan rate

Unfortunately, spectra acquired from the polymeric films containing **P5** were unsatisfactory, as presented in Figures 31c and 31d. It is assumed that the reason for such a poor film deposition is due to the very low solubility of compound **5**, which brought some challenges during this study. The result of spectroelectrochemical analysis of polymer **P5** does not acquire much information. A broad range of wavelength (from 800 – 1700 nm) exhibits an increase during doping, like a big broad band, and disappears

through dedoping. Additionally, there is a specific change in spectra, at the last stage of the dedoping process (Figure 31d), the emergence of a band at 580 nm can be noticed. Such band is very similar to the one observed at 541 nm for the electropolymerization of compound **5** (Figure 31b). However, the poor quality of the analysis, monitoring the cyclovoltabsorptiometric study presented in Figure 31f, confirms the polaronic features of the significant broad signal.

At last, the behaviour of electropolymerization of compound **7** and the spectral behaviour of the formed polymer (**P7**) are presented in Figure 32.
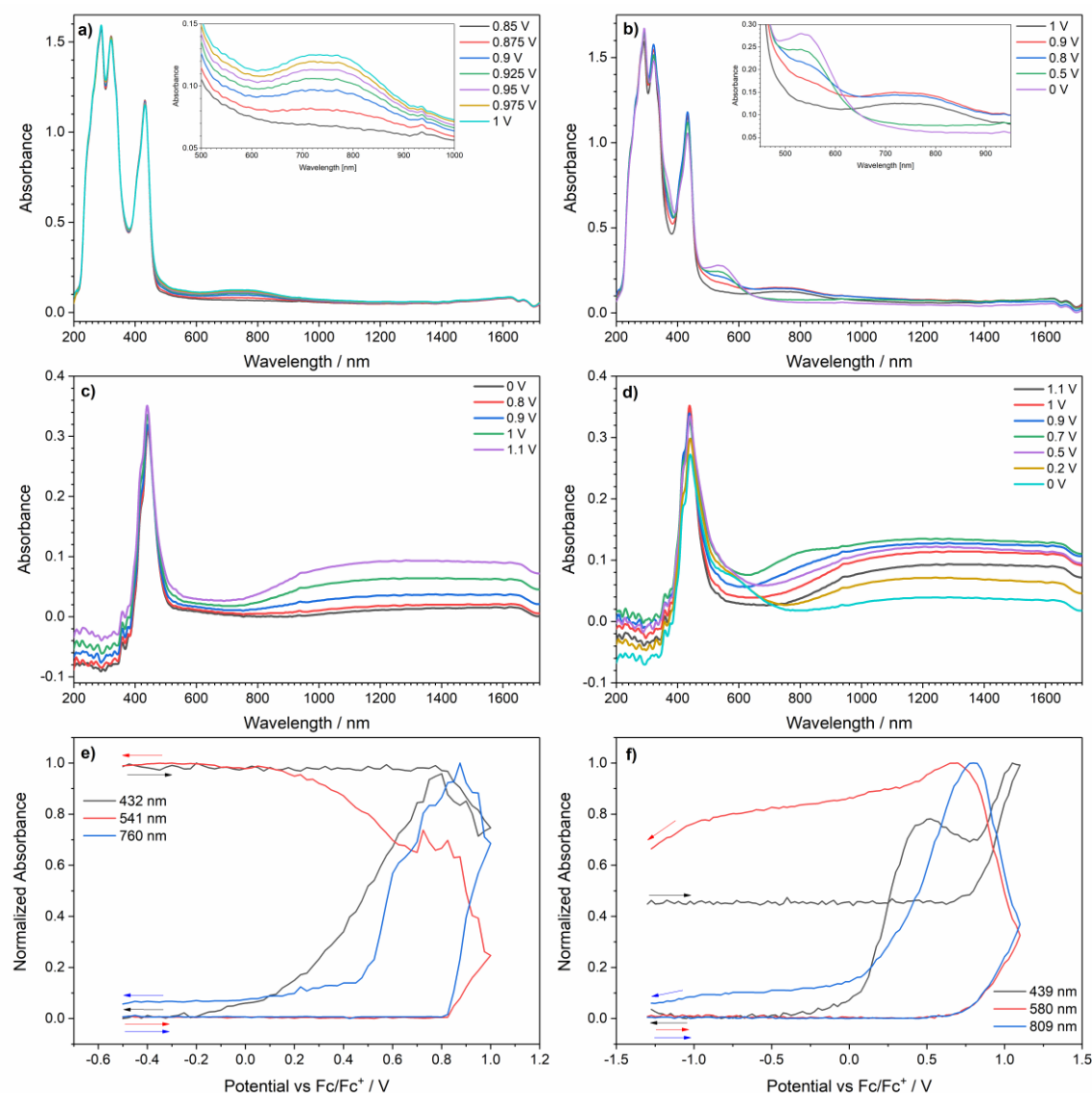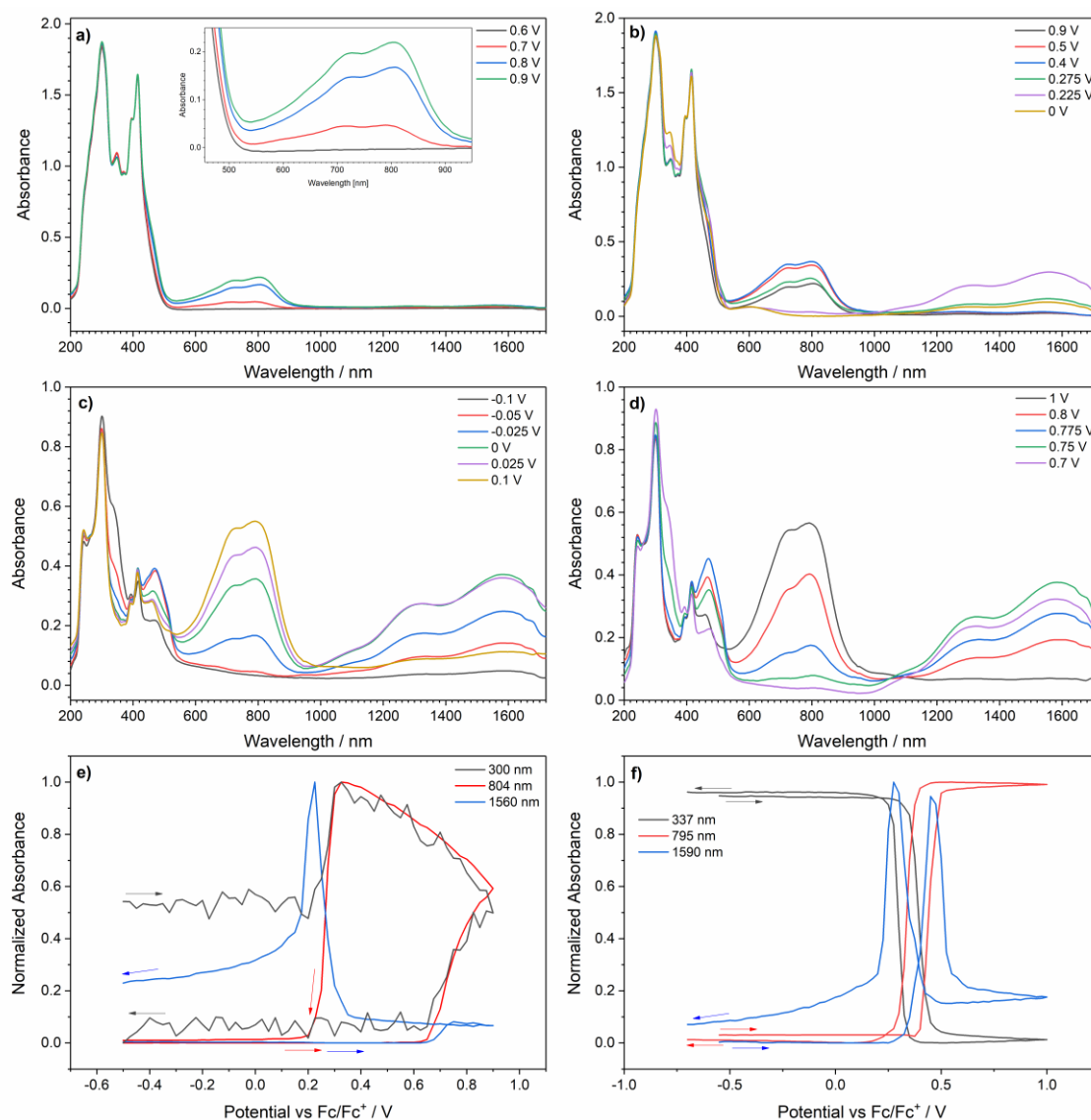

Figure 32. Potentiodynamic UV-Vis-NIR spectroelectrochemical analysis of doping process of a) 0.25 mM of compound 7 and c) polymer P7; dedoping process of b) 0.25 mM of compound 7 and d) polymer P7 in DCM Bu$_4$NBF$_4$ (0.1 M) electrolyte. Cyclovoltabsorptiometric measurement of e) electropolymerization of 7 and f)

In the first stage of doping compound **7** (Figure 32a), two close signals overlapping each other arise, with absorption maxima at 720 and 804 nm. Both signals slightly increase at the beginning of the dedoping process (Figure 32b), followed by a sudden decrease until disappearance. At the same time, two other overlapped bands emerge, with maxima at 1300 and 1560 nm. In that way, the band at higher wavelengths present polaronic features, while the signals around 800 nm are characterized as bipolaronic bands.

Still, there is no way of separating the spectral responses of monomer and polymer, and just by looking at Figure 32, it can be noticed that the spectral changes are all very similar for compound **7** and polymer **P7**.

Figure 32a shows two indications of polymer formation during compound 7 measurements: the appearance of absorbance signals at higher wavelengths, in this case, 1560 nm, only after the reverse reduction process; and the neutral monomer signal, at 300 nm, has its intensity decreased at 0.3 V and it continues decreasing after dedoping (Figure 32b), confirming that the monomer concentration has been consumed to form the polymer.

At cyclovoltabsorptiometric analysis (Figure 32e), it can be observed that at the oxidation potential for monomer **7** (0.64 V), at that same potential, the intensity of the signal at 804 nm starts to increase and only decrease in the dedoping process after 0.2 V, just before the polymer's polaronic signal in 1560 nm starts to appear, meaning that the 720 and 804 nm bands are most likely related to both monomer's and polymer's charge carriers.

Polymer **P7** has very similar behaviour to its original monomer, compound **7**. The polymer displays two polaronic bands in 1367 and 1583 nm that begin to appear at the beginning of the oxidation process (Figure 32c) and start to decrease at higher potentials, and two bipolaronic bands in 730 and 791 nm emerge when the polaronic band disappears. In addition, there are two defined isosbestic points at 523 and 984 nm (Figure 32d). The neutral form of **P7** exhibits a band in 479 nm, which starts to increase when the doping process begins and dislocates itself to 469 nm while achieving its maximum intensity, and one band in 339 nm starts to decrease and disappears.

As well as CV measurements, UV-Vis absorbance spectra can also give us information about the difference between HOMO and LUMO energy levels. In Table 2, values of bandgaps acquired from CV and UV-Vis spectroscopic measurements are presented, which are called electrochemical and optical bandgaps, respectively.

Table 2. Comparison between electrochemical and optical bandgaps of monomers and polymers.

Compounds	Electrochemical bandgap (eV)	Optical bandgap (eV)
3	2.29	2.35
P3	2.18	2.20
5	2.19	2.62
P5	2.11	2.44
7	2.19	2.48
P7	1.99	2.36

Compound **3** and polymer **P3** have very similar values for the two types of bandgap determination. The other compounds, in comparison, present values a little bit more distinct, which are not unusual since there are differences in the processes that occur during electrochemical and optical measurements.[84]

5.2.3. Potentiostatic EPR

As mentioned before, spectroelectrochemical studies can be carried out by coupling any spectral technique with an electrochemical potentiostat. In this case, potentiostatic EPR detects the formation of charge carrier species (with paramagnetic properties) at specific chosen potential values.

Figure 33 displays the potentiostatic EPR spectra of compounds **1**-**8**. Although, at first sight, the most significant difference that can be noticed is the number of signals, only compounds **3** (Fig. 33c), **5** (Fig 33e), and **7** (Fig. 33g) do not present any splitting. The absence of hyperfine splitting effect may be an indication that for compounds **3**, **5** and **7,** the radical species formed on this oxidation step have the charge located on a Carbon

atom. The higher conjugation in the polymeric film can also cause electron interaction among a larger number of protons, leading to overlap of individual lines, appearing as lack of visible splitting.
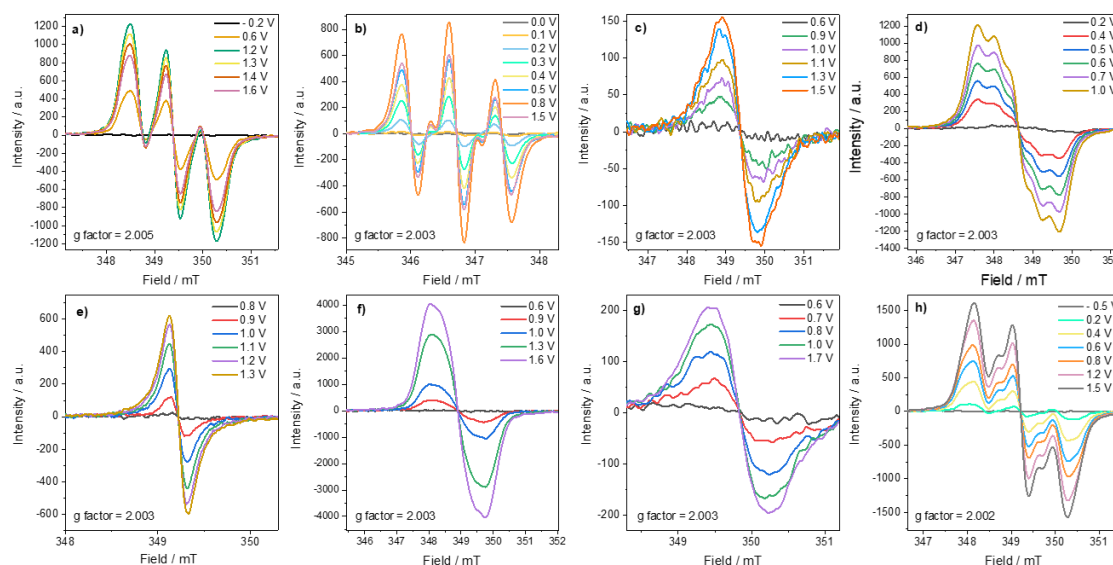
Figure 33. Potentiostatic EPR spectroelectrochemical analysis during doping process of oxidation of 0.5 mM solutions of compounds a) 1, b) 2, c) 3, d) 4, e) 5, f) 6, g) 7, and h) 8 in DCM Bu$_4$NBF$_4$ (0.1 M) electrolyte, with Pt wire as working, Pt wire as counter and Ag/AgCl as reference electrodes, at 50 mv s^{-1} scan rate.

The other compounds, **1**, **2**, **4**, **6** and **8**, present all kinds of different shapes, which is expected in EPR measurements. If there is a charge located in a Carbon atom, one signal is obtained, although if there are two charges found in two Carbon atoms (which are not spatially symmetric), it can be observed two signals, most likely overlapped, like in the case of compound **6** (Figure 33f). If the compound has a charge located at a nitrogen atom, the EPR signal will be split by 3, still, if there are two charges located in two different nitrogen atoms, it should be observed two signals with triple splitting overlapped in the most diverse ways, like in the case of compounds **1** and **2** (Figures 33a and 33b). In some cases, the spectra are not so clear, like the example of compound **8** (Figure 33h).

The EPR signal for compound **1** (Figure 33a) undergoes a rapid growth after 0.6 V, although at potentials higher than 1.2 V, the signal starts to decrease. This sudden drop in the signal's intensity may be attributed to the formation of bipolaronic species, which are doubly-charged species with non-paramagnetic properties, therefore, are not detected by the EPR measurement.

Compound **2** (Figure 33b) has very similar behaviour. Presents an intensity growth after 0.2 V, which is related to its first oxidation peak, with onset at 0.13 V. And during potentials higher than 0.8 V, the signal starts to decrease its intensity, which can represent that bipolarons are beginning to form at the second oxidation process (potential onset = 0.8 V). Compound 2 presents the presence of triple hyperfine splitting in two different types of nitrogen atoms.

The analysis of compound **4** displays the emergence of overlapped signals with only one inversion of phase. Therefore, no particular conclusion about the charge location can be drawn from these results. The signals appear at 0.4 V (Figure 33d), potentially related to its first oxidation peak, with its maximum at 0.35 V.

Compound **6** presents the rise of a broad signal starting at 0.9 V (Figure 33f), which keeps increasing during doping. It is noticeable that two different signals overlapped, followed by a decrease during dedoping, under potentials lower than 1.0V until they almost disappeared.

EPR spectra for the analysis of compound **8** display the appearance of a very broad triplet signal after 0.2 V, which keeps increasing to form better defined (although overlapped) signals. Such signals are very stable and do not disappear after the dedoping process, attributed to the irreversibility of the second stage of oxidation (Figure 25d).

Compounds **3**, **5** and **7** present a similar behaviour during the potentiostatic EPR analysis, as shown in Figure 34. However, compounds 3 and 7 (Figures 33a and 34g) present a little broad signal with very low intensities during the doping stage. On the other hand, these three compounds exhibit high intensity, very sharp and well-defined signals during the dedoping process (Figures 34b, 34e and 34h). Those intense sharp signals are associated with polymer deposition on the electrode's surface, which are only observed after the end of the first oxidation cycle.

During doping of compound **3** (Figure 34a), the broad signal's appearance and rise are noticed at 0.9 V until the beginning of the dedoping process (Figure 34b), where, at 0.5 V and following lower potentials, it becomes a very sharp signal and a sudden increase in intensity. This coincides with the return reduction potential of the redox pair of the oxidation peak at the oxidation of compound 3 (Figure 23a), which is the first evidence of polymer formation during CV measurements.

On the other hand, compound **5** displays the emergence of a signal at 0.9 V during the doping process (Figure 23d), which increases a little bit more at the start of dedoping (Figure 23e) up till 0.7 V, where there is a sudden decrease in intensity until it disappears at 0.2 V.
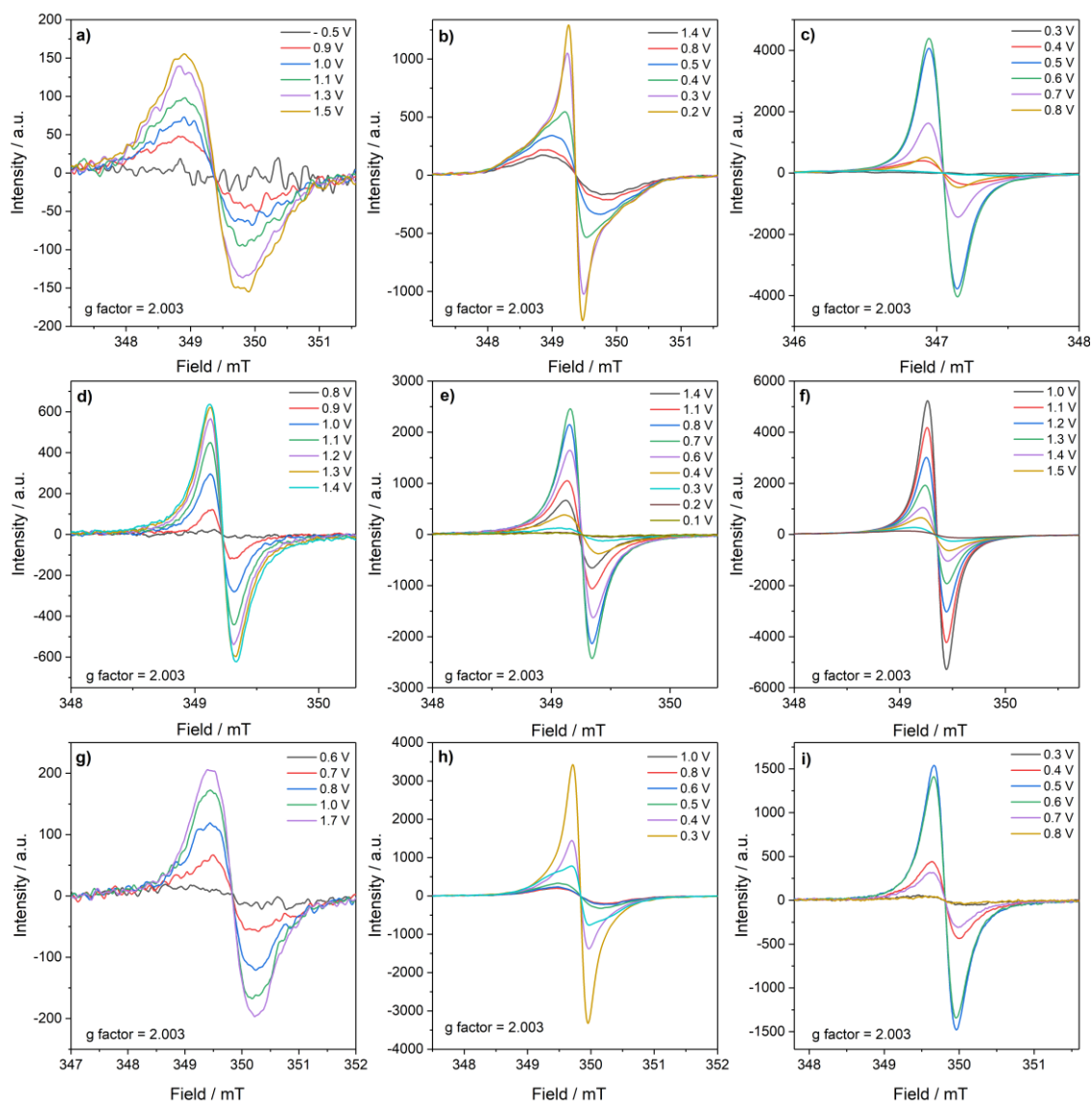
Figure 34. Potentiostatic EPR spectroelectrochemistry of oxidation during doping process of a) 0.5 mM of compound 3, c) polymer P3, d) 0.5 mM of compound 5, f) polymer P5, g) 0.5 mM of compound 7, and i) polymer P7; dedoping process of b) 0.5 mM of compound 3, e) 0.5 mM of compound 5 and h) 0.5 mM of compound 7. Pt wire working, Pt wire as counter and Ag/AgCl as reference electrodes, at 50 mv s-1 scan rate.

In Figure 34g, it can be noticed the doping of compound **7**, with the formation of a broad and low-intensity signal at potentials higher than 0.6 V. During the dedoping process

(Figure 34h), the signal continues to rise slowly, just before 0.4 V, where it suddenly becomes a very sharp and intense signal, just like in the case of compound **3** (Figure 34b), indicating the deposition of the polymeric film on the electrode's surface. At the end of the dedoping process (Fig 34h), the signal decreases in intensity, although it does not lose its sharp profile, characteristic of polymers.

From these polymeric materials formed onto the WE's surface, after the compounds 3, 5 and 7, potentiostatic EPR measurements were carried out with immersion of such electrode on pure electrolyte solution under the same stepwise conditions the monomers' analysis. As a result, the doping process of the oxidation of the polymeric films **P3**, **P5** and **P7** are displayed in Figures 34c, 34f and 34i, respectively.

Figure 34c displays the EPR spectra of doping of polymer **P3**, exhibiting the emergence of a signal at 0.4 V and sudden signal intensity growth up to 0.6 V, followed by its decrease and disappearance at 0.9 V. The signal disappearance is confirmed through the observation of the CV measurements of **P3** in Figure 26a, where, 0.6 V has noticed the second oxidation stage, forming a bipolaronic double-charged species, which will not be detected by the EPR equipment, confirming the disappearance of the signal. The potential of signal emergence is also in accordance with the first oxidation peak on CV (Figure 26a), which starts at 0.37 V.

The doping process of polymer **P5** (Figure 34f) presents the rise of a signal at 0.6 V, reaching its maximum intensity of 0.9 V, gradually decreasing from 1.0 to 1.9 V, where it completely disappears. Just like in the case of polymer **P3**, CV measurements (Figure 26b) display two stages of oxidation processes that material **P5** can undergo, the first one is generating a polaron species, detectable in EPR spectra, while the second stage creates bipolaronic non-paramagnetic species as the product.

At last, doping of polymer **P7** (Figure 34i) exhibits the same behaviour as the other two polymeric materials: an intensity increase at the start of the doping process (0.4 V) followed by a sudden decrease up to complete disappearance, in this case at 0.8 V. Also in agreement with the CV voltammogram displayed at Figure 26c, where two very distinct oxidation processes can be observed, at 0.4 V and 0.6 V.

Gathering all the information acquired so far by the CV, spectroelectrochemical UV-Vis and potentiostatic EPR measurements, we can propose structures for the polymers

generated under the electrochemical analysis of compounds **3**, **5** and **7**, shown in Figure 35.
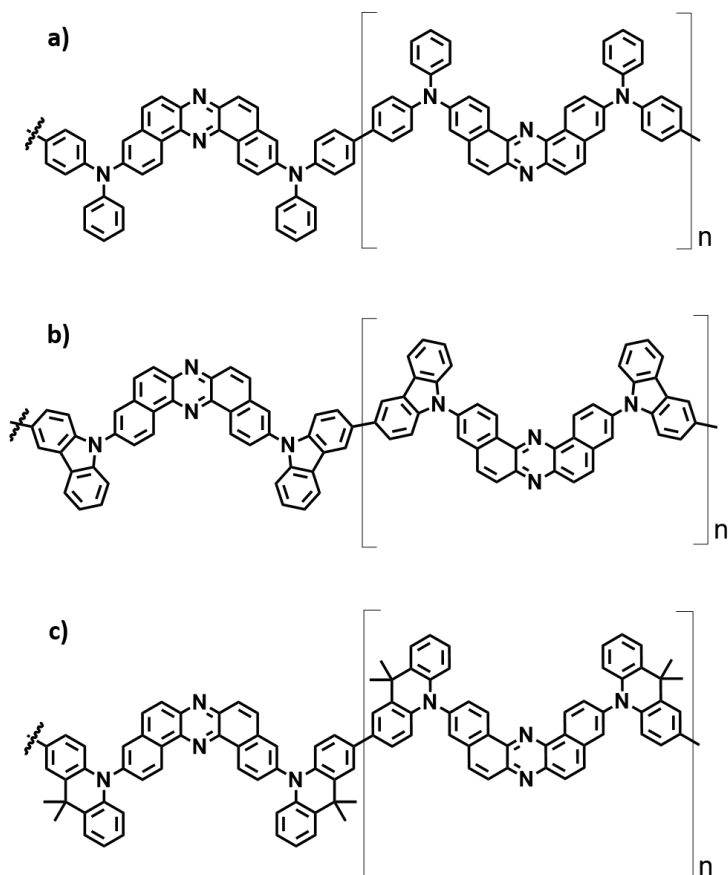
*Figure 35. Proposed structures for polymers a) **P3**, b) **P5**, and c) **P7**.*

Compounds **4** and **6** are the most similar molecular structure to the polymerizable compounds **3** and **5**, respectively. The most significant difference is the addition of alkyl chains in similar electronic positions on the structures of compounds **4** and **6**, which cannot electropolymerize. This result is attributed to the "blockage" caused by the addition of alkyl groups in the exact position in which the polymeric reaction would occur. Such effect is confirmed by EPR studies, which show that compounds **3**, **5** and **7** form oxidized radicals located over Carbon atoms, while the non-polymerizable compounds form charges placed mostly on nitrogen atoms.

As the electropolymerization reactions all happened in the measurement of oxidation processes of the materials, never during reduction, at this part of the study, the most significant focus was on the potentiostatic EPR analysis of oxidation of the compounds. Nevertheless, EPR studies were also carried out for these materials' reduction processes.

However, not all the compounds generated detectable spectra in this case. Figure 36 displays some of the acquired EPR spectra.

Considering that all the compounds share the same acceptor unit, the dibenzophenazine group, for a better comparison study, the potentiostatic EPR measurement was carried out for the dibenzophenazine acceptor itself (Figure 36a).

Compounds **1** (Figure 36b), **2** (Figure 36c), **4** (Figure 36d), **5** (Figure 36e), **6** (Figure 36f), **7** (Figure 36g) and the dibenzophenazine acceptor (Figure 36a) presented the appearance of a signal during doping of the reduction process, followed by a gradual increase up until the maximum negative potential reached in each measurement.

Compounds **5** and **7** (Figures 36e and 36g) display EPR spectra with a very similar shape to the isolated dibenzophenazine group (Figure 36a). Almost all the acquired spectra exhibit hyperfine coupling, indicating that the charge position must be located at different nitrogen atoms.

The only compound which not present hyperfine coupling during reduction spectra was polymer **P3** (Figure 36h). During the beginning of the doping process, a signal is detected at -2.2 V, which rapid increases up to -2.3 V. At -2.4 V and lower potentials, there is a decrease in signal intensity until it almost disappears. Such effect is not explainable by the CV measurements of **P3**'s reduction, where only one visible reduction process involves only 1 electron, it can be caused by degradation.
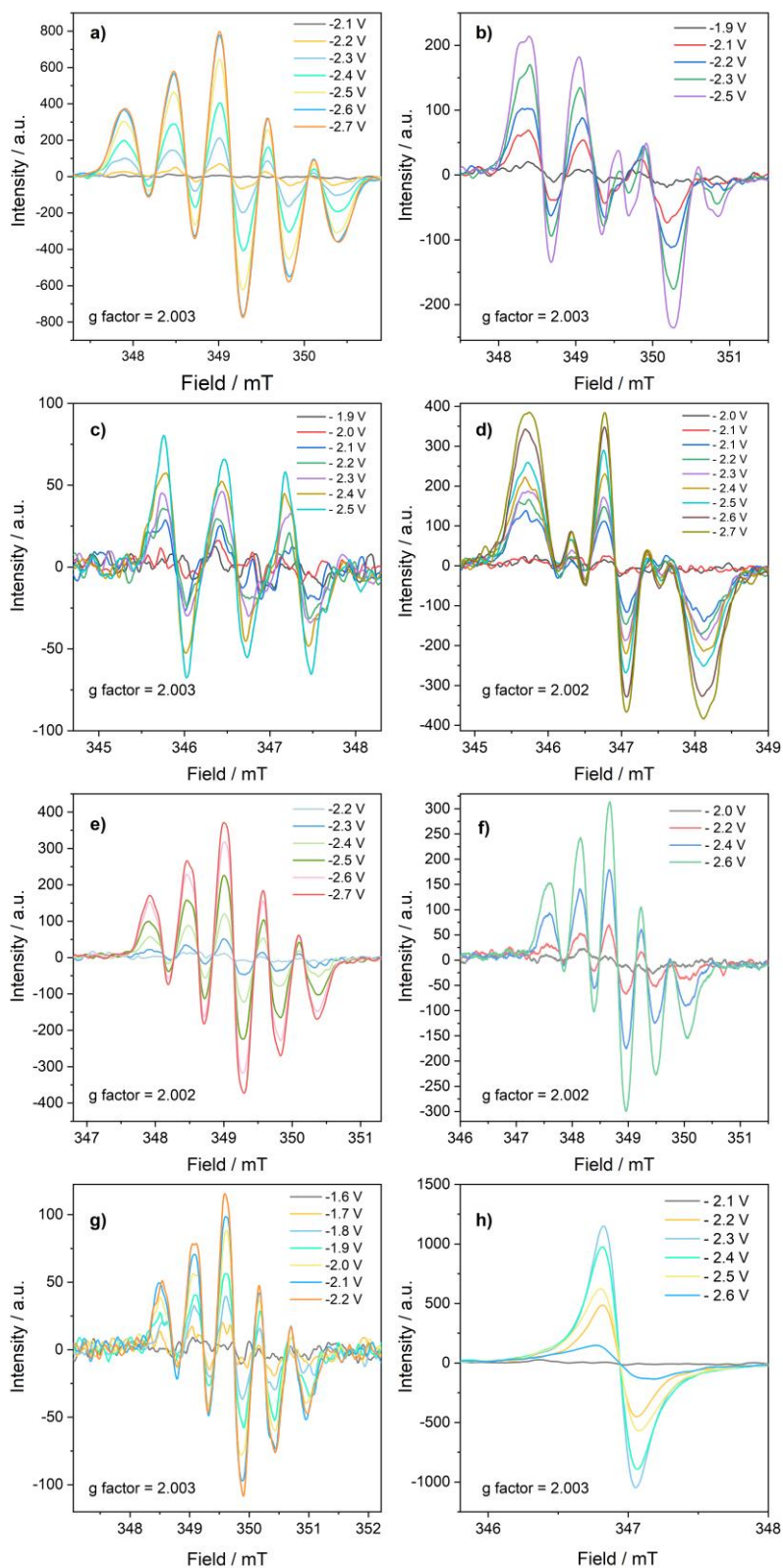
Figure 36. Potentiostatic EPR spectroelectrochemical analysis during doping process of reduction of 0.5 mM solutions of a) dibenzophenazine, b) 1, c) 2, d) 4, e) 5, f) 6, g) 7, h) polymer P3 in DCM Bu₄NBF₄ (0.1 M) electrolyte, with Pt wire as working, Pt wire as counter and Ag/AgCl as reference electrodes, at 50 mv s-1 scan rate.

5.2.4. Electroluminescent Devices

Nearly all of the compounds studied in this Chapter have been published in the application of TADF-based OLED devices.[52,85] However, since compound **5** is a novel material, OLED devices were manufactured containing compounds **1-8** for a complete comparison study of the emitters' behaviours.

The devices were structured as follows: ITO | HAT-CN(10 nm) | NPB(30 nm) | CBP co 10% **1-8** (30 nm) | TPBi (50 nm) | LiF (0.8nm) | Al(100 nm)   (Device **1-8**). The characteristics of these TADF-based OLED devices are presented in Figure 37.
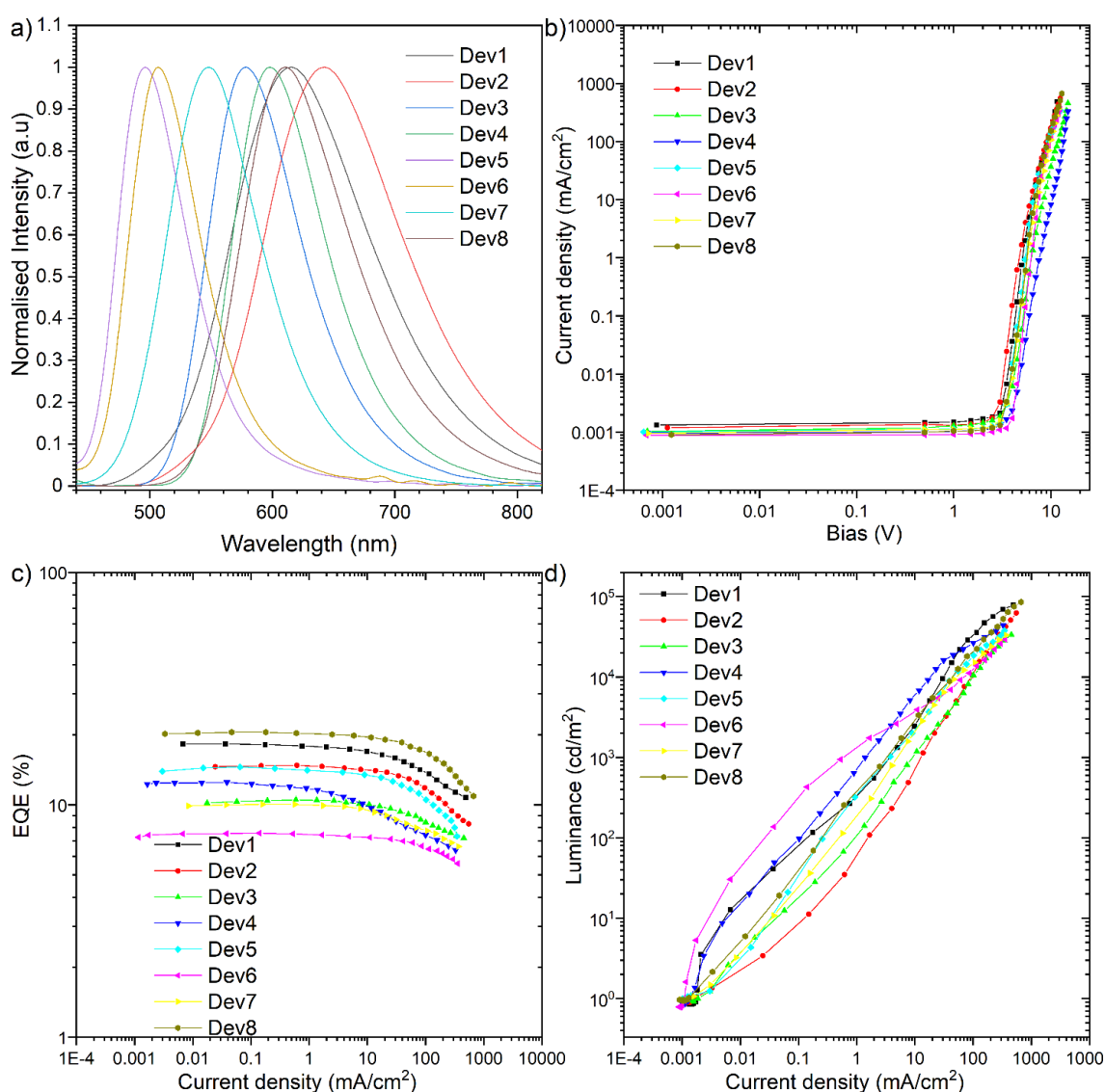
Figure 37. OLED device characteristics: a) electroluminescence spectra; b) current density vs. voltage characteristics; c) EQE vs. current density; d) luminance vs. current density.

The electroluminescence spectra for devices **1-8**, shown in Figure 37a, display emission in a wide spectral range, exhibiting emission maxima from 494 nm (Device **5**) to 642 nm (Device **2**). Compounds **1** and **8** present a similar maxima wavelength, sharing a similar structure, varying from sulfur to oxygen heteroatoms at the donor moieties. However, comparing compounds with their substituted analogous, such as **1** and **2,** for example, it is noticed a redshift for the substituted materials **2**, **4** and **6** in comparison to **1**, **3** and **5,** respectively.

All devices presented a very small roll-off, which can be observed by the slight decrease in efficiency with an increase of current density in Figure 37c. Compounds **1**, **2**, **4**, **7** and **8** improved their EQEs and luminance values compared to previous reports.[52,85] Device **8**, based on phenoxazine donor, achieved an EQE value of 20.5%, being the highest efficiency of the devices. The lowest efficiency was observed for Device **6**, with 7.5% EQE, containing a *tert*-butylcarbazole based emitter. The use of an improved device structure resulted in higher efficiency and stability for all the previously reported compounds.[52,85] Apparently, the electropolymerization ability of compounds **3**, **5** and **7** are not leading to device degradation.

An interesting comparison can be made between compounds **5** and **6**, containing carbazole and *tert*-butylcarbazole. In Figure 37c, a significant increase in the OLED efficiency is observed for compound **5**, with the absence of the alkyl group, presenting 14.5% EQE. This increase can be attributed to removing the TTA process, observed for emitter **6** in the previous report.[85] The existence of the TTA process limits the emission efficiency, whereas its removal could influence the TADF behaviour.

Figure 37d displays device luminance *vs.* current density, where the highest OLED luminance was observed in device **8**, based on phenoxazine donor, presenting up to 85 000 cd/m^2. The second highest luminance was measured for device **1**, containing the phenothiazine donor group, with 77 000 cd/m^2.

5.2.5. Electrochromic Properties

In this study, the polymeric materials formed by electropolymerization exhibit significant changes in the near-infrared (NIR) region of the spectra gathered through

spectroelectrochemical analysis. Such changes upon applied potential are very interesting for using electrochromic devices in the NIR region.

Electrochromic devices using organic polymers active in the NIR region possess long-term stable films and achieve high colour contrast devices with high conductivity, fast switching, and low cost of production. Particularly polymers containing donor-acceptor skeletons are considered the most successful method for tuning the HOMO and LUMO bandgap, resulting in a 99% colour contrast ratio.[98]

The analysis of electrochromic devices manufactured with compounds **1**-**8** and the polymers formed during this study are summarized in Table 3.

Table 3. Electrochromic properties of investigated compounds. λ – investigated wavelength; Tox – transmittance of oxidized film at given wavelength λ; Tred – transmittance of neutral film at given wavelength λ; ΔOD – a difference of optical density between neutral and oxidized film at given wavelength λ; QD – charge density calculated in a chronocoulometric experiment; CE – colouration efficiency; CR – contrast ratio.

Compound	λ /nm	T_{red} /%	T_{ox} /%	ΔOD	Q_D /mC·cm^{-2}	CE /cm^2·C^{-1}	CR (-)
1	551	99.31	77.62	0.107	0.83	128.28	1.28
2	578	98.86	28.84	0.535	1.26	423.97	3.43
3	621	99.54	52.48	0.278	1.45	191.29	1.90
4	781	98.86	67.61	0.165	1.37	120.73	1.46
5	768	97.95	60.26	0.211	1.07	197.75	1.63
6	559	99.54	58.88	0.228	1.76	129.60	1.69
7	804	99.77	22.39	0.649	3.72	174.33	4.46
8	532	99.31	33.11	0.477	1.44	330.15	3.00
P3	759	99.54	35.48	0.448	0.96	466.47	2.81
P5	1183	99.77	67.61	0.169	5.53	30.57	1.48
P7	787	95.50	15.14	0.800	1.79	446.68	6.31

To quantify the performance of electrochromic devices is necessary to acquire the optical density change (ΔOD), percentage transmission (T$_X$%), and colour ratio (CR), among

other parameters. The colour efficiency (CE) is used as a standard method to measure the effective change in optical transmission caused by applied potential. For the mathematical determination of CE, we need charge density (Q_D) values attributed to the applied charge divided by the device's electrode area.[99]

The best results of colour efficiency values were attributed to compounds **2**, **8**, **P3** and **P7**, being all over 300 cm^2 C^{-1}. Such high values of CE are very promising for future structural optimization.

If we think about the NIR application, it is unfortunate that the device with the highest wavelength achieved (**P5** – 1183 nm) exhibits a relatively small CE value (30.57 cm^2 C^{-1}).

Compounds **2**, **8**, **P3** and **P7** present colour efficiency values (CE>300) promising for future structural optimization.

The characterization does not result in desired parameters for the application of such devices. However, with the use of an improved structure, they may present more interesting properties. For example, the polymeric films used for the electrochromic devices containing **P3**, **P5** and **P7** were deposited by electropolymerization, which usually results in layers with very low uniformity. Perhaps, using more sophisticated solution process methods may result in devices with improved efficiencies.

5.3. Conclusions

Herein, an investigation of a group of dibenzophenazine D-A-D electroactive compounds was presented, where their electrochemical and spectroelectrochemical parameters and stability were analyzed and discussed. In addition, a complete study of electropolymerization properties was carried out with some compounds. Charge carrier species of monomers and polymers were characterized by UV-Vis spectroelectrochemical and potentiostatic EPR measurements.

The compounds investigated in this study were applied in the manufacture of electrochromic and electroluminescent devices, which were characterized and compared among them. Unfortunately, the electrochromic devices did not exhibit interesting

features in the way they were assembled, although they may be improved by structure modification.

With an improved structure of electroluminescent devices used in this work, all the previously reported[52,85] compounds increased the EQEs and luminance values. The TADF-based OLED devices were fabricated to compare the novel compound (**5**) to all the others. The device based on compound **5** displays intermediate EQE among its analogous, exhibiting 14.5%.

6. Photophysical and Spectroelectrochemical Characterization of D-A-D Iminostilbene and Iminodibenzyl Derivatives.

6.1. Introduction

Carbazole (Cz) is an organic aromatic compound consisting of three cycles fused together, being two six-membered rings on the edges and a heterocyclic five-membered ring with a nitrogen atom in the middle. It is found naturally in fossil fuels, such as coal.[100] Its extensively used in many distinct applications,[101–103] and as a consequence of its rich electron density and high reactivity in synthesis, it is easily inserted in organic structures.[104] Optoelectronic materials containing Cz units are used as hole-transporting materials and organic semiconductors.[105,106]

With its planar, rigid and aromatic characteristics, Cz generates donor-acceptor structures with a twisted character around the C-N bond, leading to excited states with reduced ΔE_{ST}, which benefits the observation of TADF behaviour.[107–109]

Furthermore, Cz analogues iminostilbene (ISB) and iminodibenzyl (IDB) consist in very similar structures, with a C2-insertion in the middle ring comprising two six-membered rings fused on either side of a seven-membered nitrogen-containing ring.[110]

Although their use in twisted donor-acceptor skeletons is way less explored and studied, Pashazadeh *et al.* reported, in 2018, that compounds containing IDB and ISB donor groups, with donor-acceptor-donor skeletons, presenting unique mechanochromic luminescence properties, as well as dual TADF and RTP emission.[111]

Also, in 2018, another report inserting IDB donors in donor-acceptor-donor structures compared to other structures, applying analogues donors while using the same acceptor, provided a series for studying the effects of rigidity/flexibility of chromophores on the efficiency of TADF behaviour. They demonstrated that IDB donor presents an intermediate impact between diphenylamine and dihydroacridine, combining relatively strong electron donor efficiency and flexibility.[112]

Recently, Jhun *et al.* disclosed a comparison study of donor-acceptor structures containing coumarin as acceptor moiety along with different donors, including IDB. The main idea was to investigate dual emission properties, including TADF behaviour however, the long wavelength emission of the IDB containing product did not exhibit delayed fluorescence due to a not efficient rISC process.[113]

Another work, published in 2020, demonstrating the synthesis and photophysical characterization of donor-acceptor compounds containing IDB and ISB as donors, presented aggregation-induced emission. In addition, the IDB derivative displayed dual emission strongly dependent on solvent polarity as well as mechanochromic character.[114]

Through the use of a tilted face-to-face alignment with an optimal distance synthesis approach, Kusakabe *et al.* accomplished to obtain the desired molecular conformation between donor and acceptor moieties, optimizing the rISC rate, observing a strong TADF emission with high photoluminescence quantum yield.[115]

Nevertheless, compared with the Cz group, there are few studies or systematic studies of the photophysical properties of donor-acceptor compounds containing IDB and ISB as donor groups and their influence on TADF behaviour.

With all these exciting possibilities in mind, for achieving interesting emission properties with such compounds, in collaboration with Prof. Takeda's group at Osaka University, was conducted a complete study of the photophysical properties of IDB and ISB derivatives (**9a** and **9b**, Figure 38) with donor-acceptor-donor skeletons containing dibenzophenazine as acceptor, to probe the influence of installing 7-membered diarylamines instead of carbazoles, on the emission properties. Such work was presented as a publication in Chemistry - A European Journal in 2021.[10] Herein, I would like to present my contribution to this study.
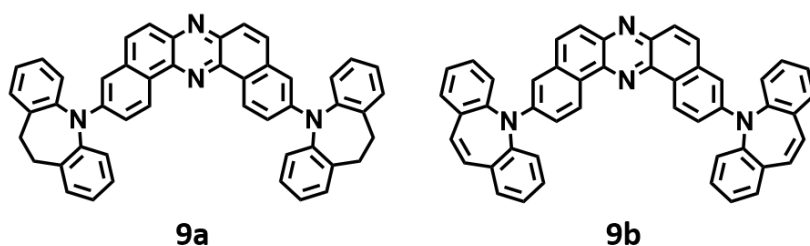

*Figure 38. Molecular structures of compounds **9a** and **9b**, IDB and ISB derivatives.*

6.2. Results and Discussion

6.2.1. Electrochemical Studies

The electrochemical behaviour for compounds **9a** and **9b** were investigated through Cyclic Voltammetry (CV), as displayed in Figure 39. The compounds present one reduction and two oxidation peaks in the potential range in both cases. Therefore, it is possible to investigate using the combination of DCM and Bu_4NBF_4 (as solvent and electrolyte, respectively).

The obtained values of the onset potentials of first oxidation and first reduction were used to determine the energy of the frontier orbitals. All the potential values obtained and the calculated energy levels for HOMO and LUMO are presented in Table 4 as well as in the diagram shown in Figure 40.
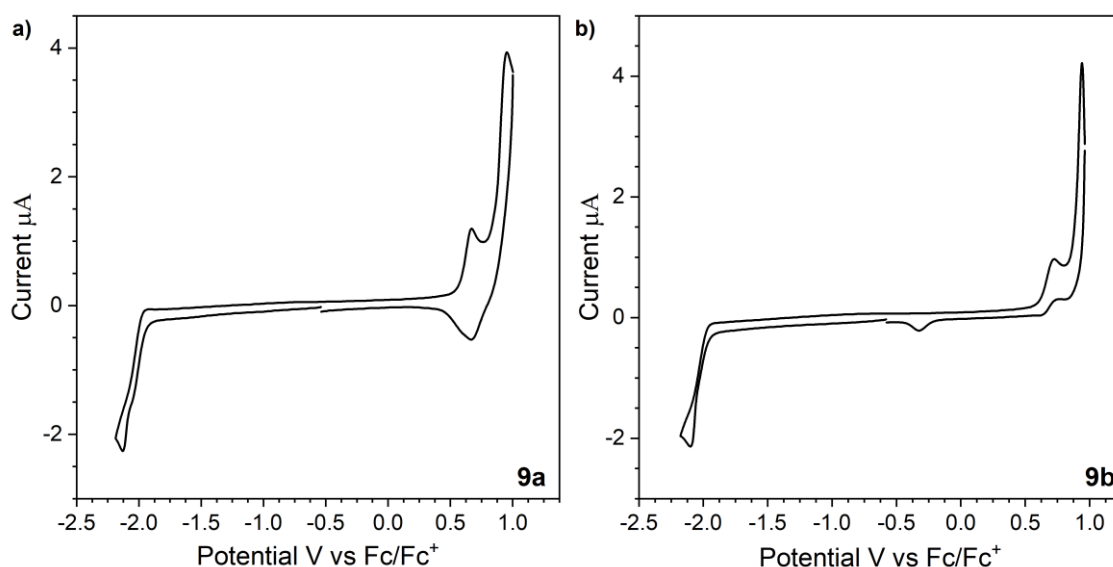
Figure 39. Cyclic voltammograms of a single scan of 1 mM of compounds a) **9a** *and b)* **9b** *in DCM containing 0.1 M Bu_4NBF_4 as electrolyte. Pt disk working, Pt wire as counter and Ag/AgCl as reference electrode, at 50 mv s^{-1} scan rate.*
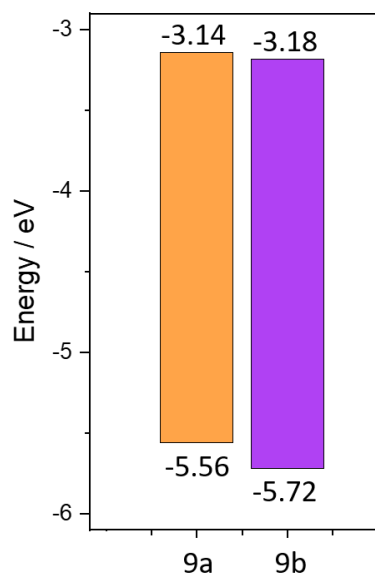
*Figure 40.Diagram of HOMO and LUMO energy levels of compounds **9a** and **9b**.*

Although both compounds presented 2-step oxidation with irreversible redox processes, during second and further scans of the CV of compound **9a**, containing the IDB donor, is observed a successive rise of peak current along with the shift of oxidation peak onset and the appearance of a peak on lower potential, as showed in Figure 41a. As discussed in Chapter 3, the rise of current indicates the deposition of conductive species on the electrode's surface; and the potential shift represents that such species, formed during the electrochemical process, may present higher conjugation of electron density, all characteristics of electropolymerization.
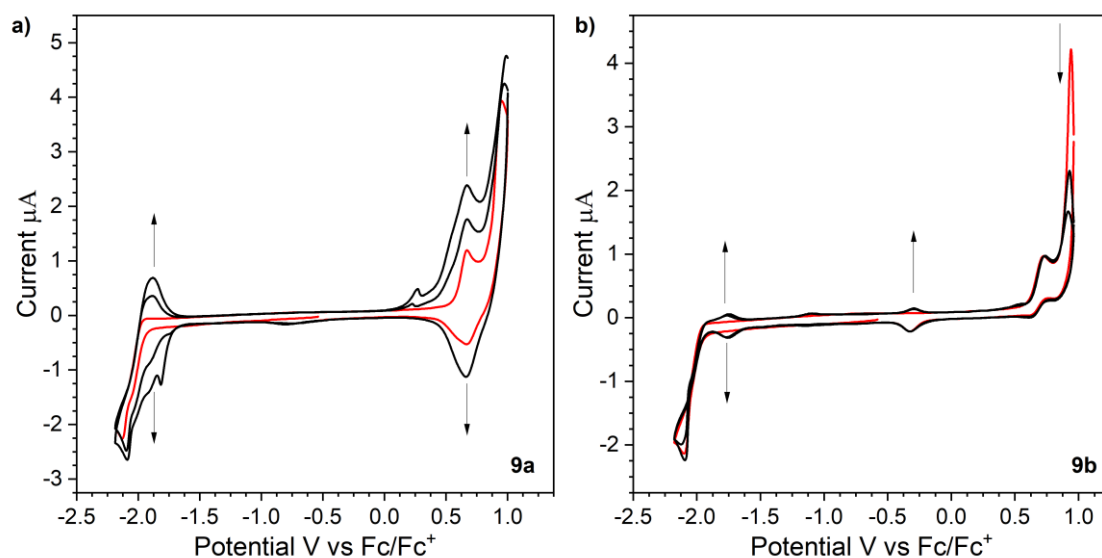
*Figure 41. Cyclic voltammograms of first (red) and following scans (black) of 1 mM of compounds a) **9a** and b) **9b** in DCM containing 0.1 M Bu₄NBF₄ as electrolyte. Pt disk working, Pt wire as counter and Ag/AgCl as reference electrode, at 50 mv s⁻¹ scan rate.*

For a better understanding of the polymerization reaction that occurs during the electrochemical measurements, a more detailed analysis was carried out, with different potential boundaries (Figure 42), as a way to identify the potential necessary for the polymerization to start, as well as the electrochemical stability and properties of the polymer formed. According to the follow-up analysis, the polymerization does not begin until the end of the first oxidation process (Figure 42b), indicating that it is necessary for the presence of a minimum amount of oxidized species to react and form the polymer, as it can be noticed in Figure 42a, where is shown the beginning of the first oxidation peak of the monomer, but no polymerization is seen. Even though the start of polymerization is noticeable after the first oxidation process, the electropolymerization reaction is only boosted when the second oxidation process starts (Figure 42c), producing the conjugated polymer with good electrochemical stability.
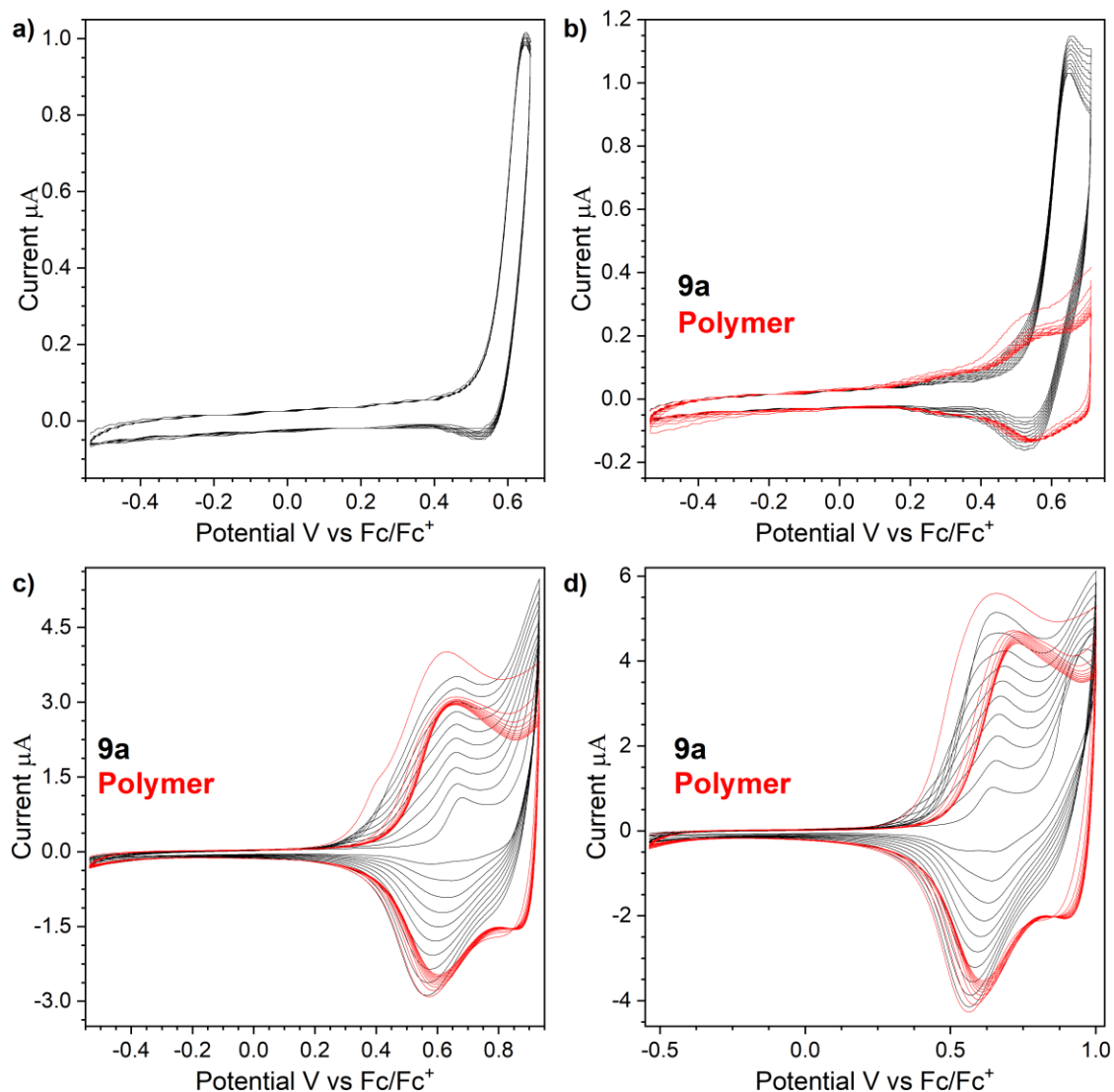
*Figure 42. Cyclic voltammetry of 1mM of **9a** in DCM Bu$_4$NBF$_4$ (0.1 M) electrolyte with different potential boundaries. a) at the first peak, b) after the first peak, c) at the second peak, d) after the second peak. Electropolymerization in black and the electrochemical stability of the polymer in red.*

The electrochemical stability of the polymer was carried out with the insertion of the Pt disc electrode with the electrodeposited polymer on its surface, on a solution of DCM containing only Bu$_4$NBF$_4$ as electrolyte. From the onset potentials of the first oxidation and reduction, the HOMO and LUMO energy levels of the resulting polymer were determined to be –3.31 eV and –5.38 eV, respectively (Figure 43). The calculated energy

levels of the frontier orbitals for the monomers **9a**, **9b** and the polymer formed from the electropolymerization of **9a** are summarized in Table 4.
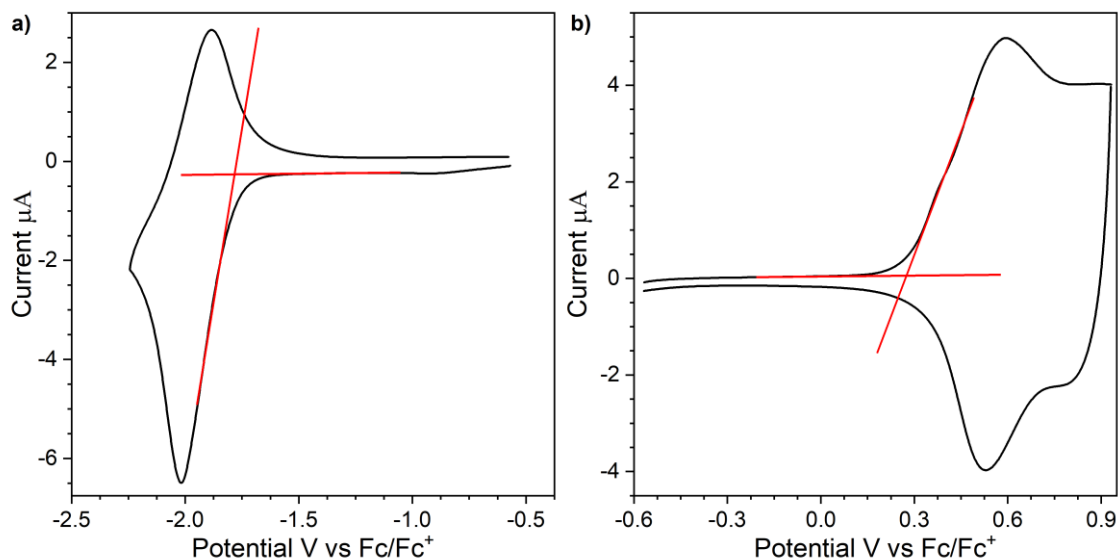
Figure 43. A single scan of cyclic voltammetry measurement of the deposited polymer a)reduction and b) oxidation processes (The delimitation of onset potentials in red). In DCM containing 0.1 M Bu₄NBF₄ as an electrolyte, Pt disk working, Pt wire as counter and Ag/AgCl as reference electrode, at 50 mv s⁻¹ scan rate.

Compound **9b** has an entirely different behaviour than compound **9a**. As shown in Figure 41b, during second and following scans of CV, the oxidation peak has a sudden decrease in current, while the appearance of new redox couple peaks in -0.29 and -1.75 V is observed, indicating the formation of new species during the electrochemical measurement. However, it does not follow the expected behaviour for forming conjugated polymers in this case. Such behaviour can be explained by the formation of sigma-dimers of compound 9b in the electrode's surface, an effect already observed and explained by Frank et al. in 1975.[116] Such sigma-dimers are responsible for the decrease of conductivity of the material, noticed by the decrease in current in the voltammogram. The sigma-dimers' formation is only observed after the second oxidation process of the monomer (Figure 44b), where the decrease of current of both oxidation peaks referring to the monomer, at 0.73 V and 0.94 V, and the appearance of the dimer oxidation peak at -0.25 V can be noticed. The proposed structure for the formed sigma-dimer is represented in

Figure 44c, and its calculated HOMO and LUMO energy levels are summarized in Table 4.

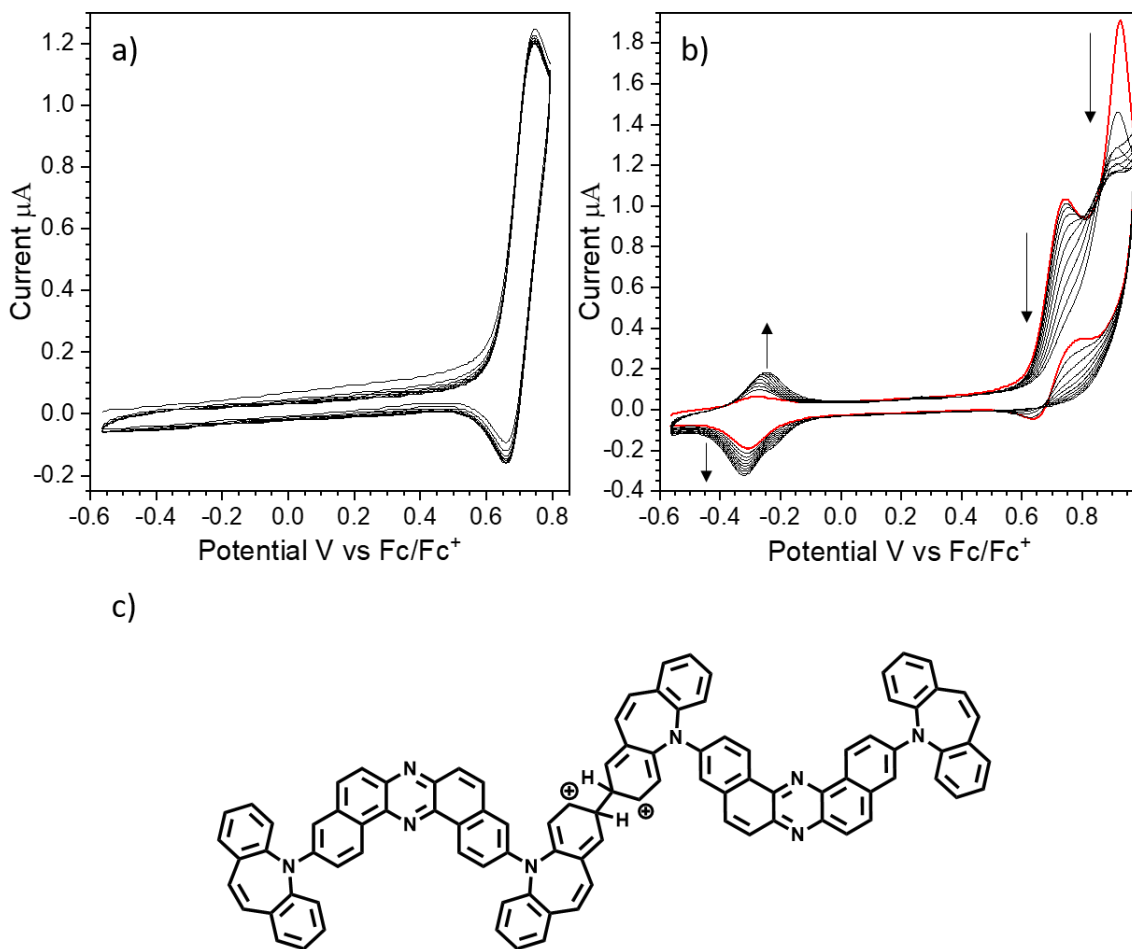*Figure 44. Cyclic voltammetry of 1 mM of **9b** in DCM Bu₄NBF₄ (0.1 M) electrolyte with different potential boundary conditions. a) cyclic oxidation up to the first peak, b) cyclic oxidation up to the second oxidation peak, and c) a possible σ-dimer structure.*

Table 4. Potential values for oxidation and reduction processes and HOMO and LUMO energy levels.

	E_{ox} / V	E_{ox2} / V	E_{HOMO} / eV	E_{red} / V	E_{LUMO} / eV
9a	0.67	0.95	-5.56	-2.13	-3.14
9b	0.73	0.94	-5.72	-2.10	-3.18
Polymer (9a)	0.59	-	-5.38	-2.01	-3.31
σ-dimer (9b)	-0.25	-	-4.75	-1.75	-3.46

The difference in the electrochemical behaviour of compounds **9a** and **9b** could be explained by the extra bond (C=C) present in the ISB group of **9b**, which might allow for the electron density delocalization when the (di)radical (di)cation is formed during the second stage of the oxidation process.

When comparing the HOMO energy levels of IDB (**9a**) and ISB (**9b**) derivatives with their analogues containing *t*-butylcarbazole (*t*-BuCz) and diphenylamine (DPA) as donor groups instead, is detected a higher similarity with HOMO energy levels of DPA (-5.59 eV)[52] than with *t*-BuCz (-5.59 eV)[85], which can be related to a consequence of conformational configurations. The LUMO levels, on the other hand, are way less affected by the change of donors once the expected overlap between HOMO and LUMO orbitals should be minimum in this type of donor-acceptor-donor structure, and the LUMO orbital is placed mostly over the acceptor part of the molecule, the dibenzophenazine group. The LUMO energy levels of *t*-BuCz and DPA analogues are -3.37[85] and -3.29 eV[52], respectively.

6.2.2. Spectroelectrochemical UV-Vis

The additional spectroelectrochemical analysis of the doping and dedoping processes was conducted to characterize the charge carrier species formed during electrochemical conditions. Spectroelectrochemical UV-Vis-NIR measurements require a transparent electrode to allow the passage of the light bean excitation through the solution, and in this study, ITO electrodes were used. However, only the oxidation processes were studied due to the instability of ITO coated glass at negative potentials.

During the UV-Vis and NIR spectroelectrochemical study of compound **9a**, the decrease of the bands at 306 and 470 nm is observed, referring to the neutral initial species, as shown in Figure 45a, upon increased potential. That is consistent with the idea that the monomer is undergoing an electrochemical reaction, forming the conjugated polymer, which is characterized by the appearance of new bands around 600 and 790 nm. The band at 600 nm keep increasing its intensity even during the dedoping process, accompanied by the appearance of another band at 365 nm. The polymeric film formed on the ITO's surface during the analysis of compound **9a** was also analyzed, being immersed in DCM solution containing Bu_4NBF_4, and it can be seen in Figure 45b.

Compound **9b** presented a very similar behaviour during the UV-Vis-NIR spectroelectrochemical measurements, showing the formation of a single broad band around 580 nm, which is referent to the generation of radical species (Figure 45c). No spectral changes were detected during the dedoping process of compound **9b**.

It is worth mentioning that any bipolaronic band formation was not observed for both compounds.
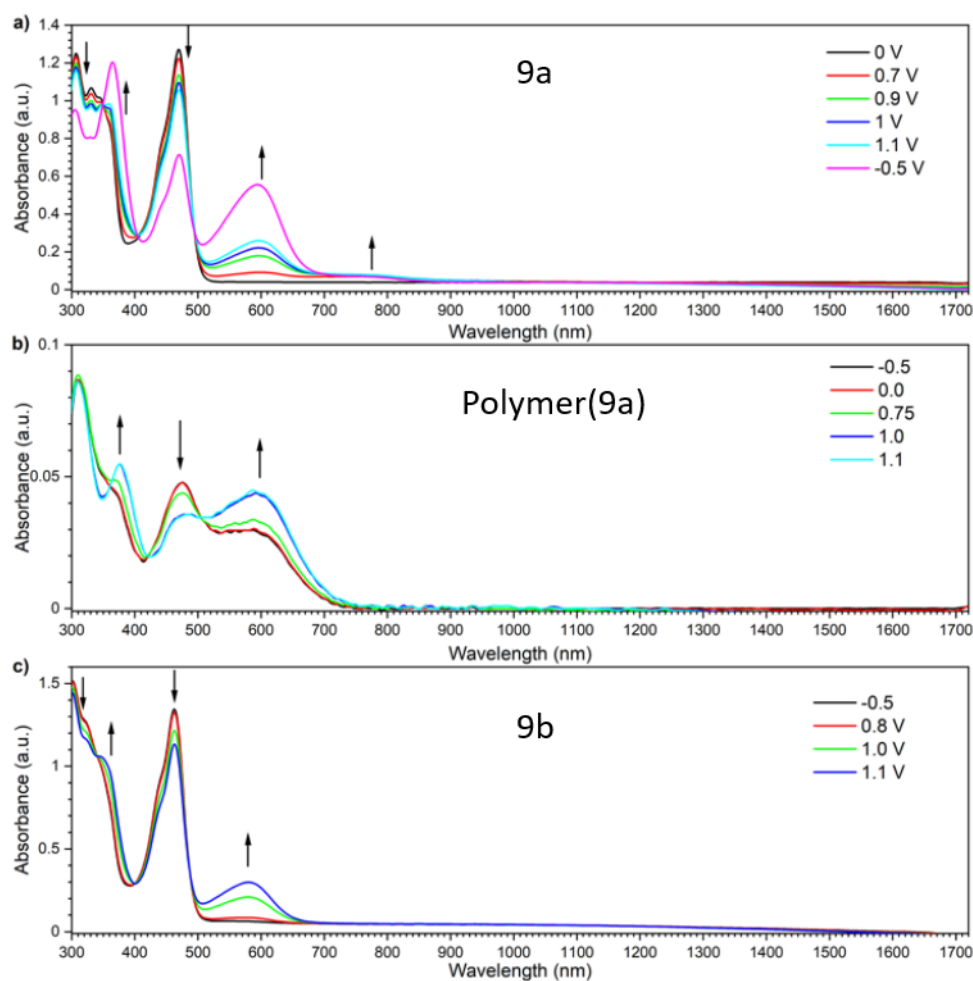
*Figure 45. UV-Vis-NIR spectroelectrochemistry of (a) **9a**, (b) Polymer**9a**, and (c) **9b** in DCM with Bu$_4$NBF$_4$ (0.1 M) as electrolyte. Concentrations of 9a and 9b are 1mM.*

Spectra acquired at neutral conditions, without voltage applied, give information about optical bandgap; thus, the minimum necessary energy for a transition occurs. Comparisons between optical and electrochemical bandgaps are displayed in Table 5.

*Table 5. Comparison between electrochemical and optical bandgaps of compounds **9a**, **9b** and polymer(**9a**).*

Compounds	Electrochemical bandgap (eV)	Optical bandgap (eV)
9a	2.42	2.25
Polymer(9a)	2.07	1.76
9b	2.54	2.50

6.2.3. Potentiostatic EPR

With the help of potentiostatic EPR measurements during oxidation and reduction processes, we can analyze the formation of charge carriers. For all compounds, **9a**, **9b** and the polymer formed from **9a**, the obtained spectra confirmed the formation of polaron species during oxidation and reduction. However, in oxidation, the spectra' intensity is very low, as shown in Figure 46.

During oxidation processes, the charged species formed are very stable, even during dedoping processes (Figure 46b and 46d), where there is no EPR signal's disappearance, which implies that the oxidation processes are irreversible, as confirmed by CV measurements.

The absence of hyperfine coupling in any EPR signals of oxidations processes indicates that the charges formed are localized mainly over Carbon atoms.

Figure 46. Potentiostatic EPR spectra for oxidation processes during doping of compounds a) 9a, c) Polymer(9a), and e) 9b; and during dedoping of compounds b) 9a and d) Polymer(9a).

Moreover, during the reduction processes, spectra show intense EPR signals for compounds **9a** (Figure 47a and 47b) and **9b** (Figure 47e and 47f) with triple hyperfine coupling, which indicates that the charge formed is located over nitrogen atoms on the acceptor moieties. However, EPR spectra for the polymer(**9a**) (Figure 47c and 47d) do not exhibit any hyperfine coupling, implying that the charge formation is localized over a Carbon atom. In all the cases, the EPR signals decrease or disappear during the dedoping, indicating the reversibility of the reduction process.
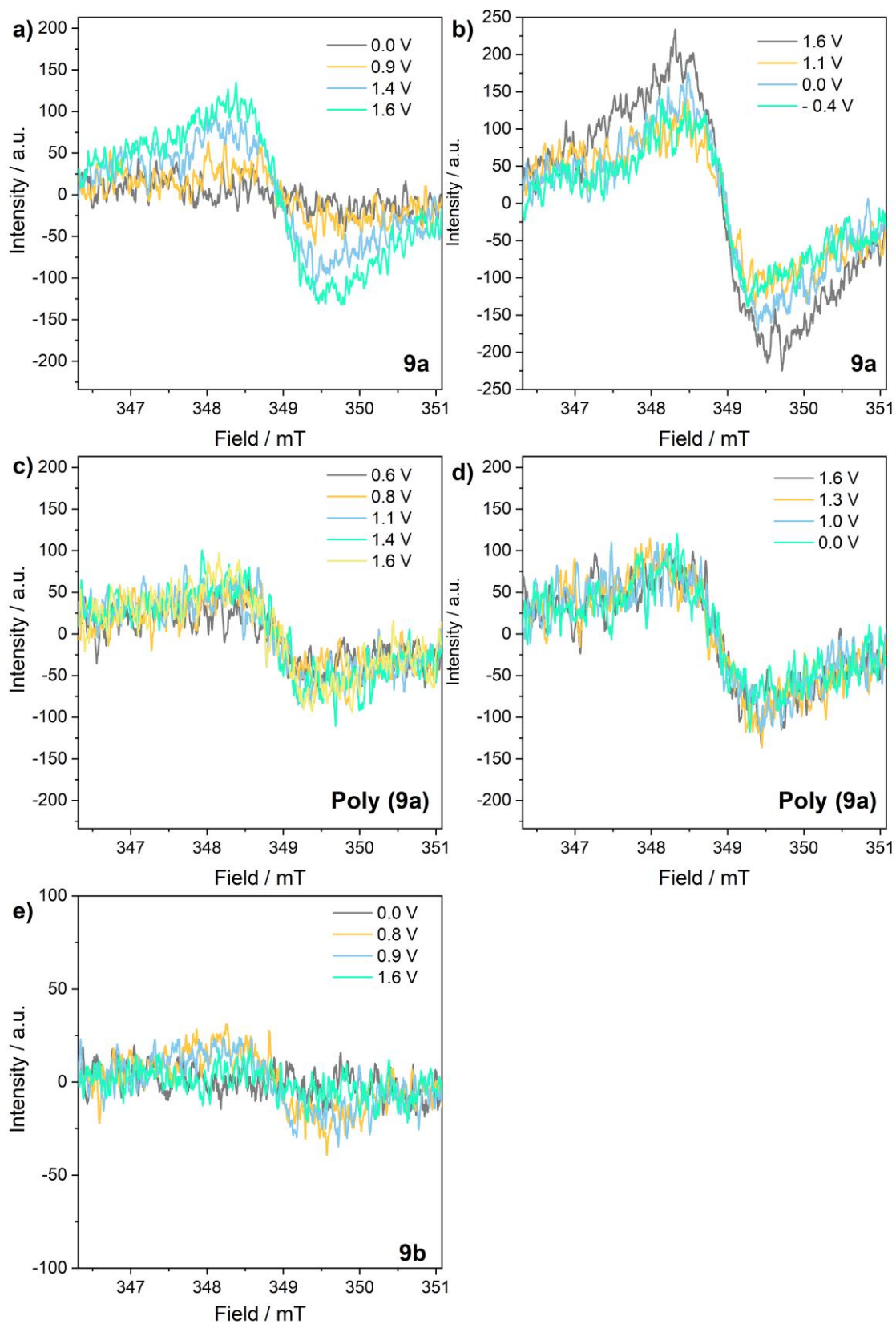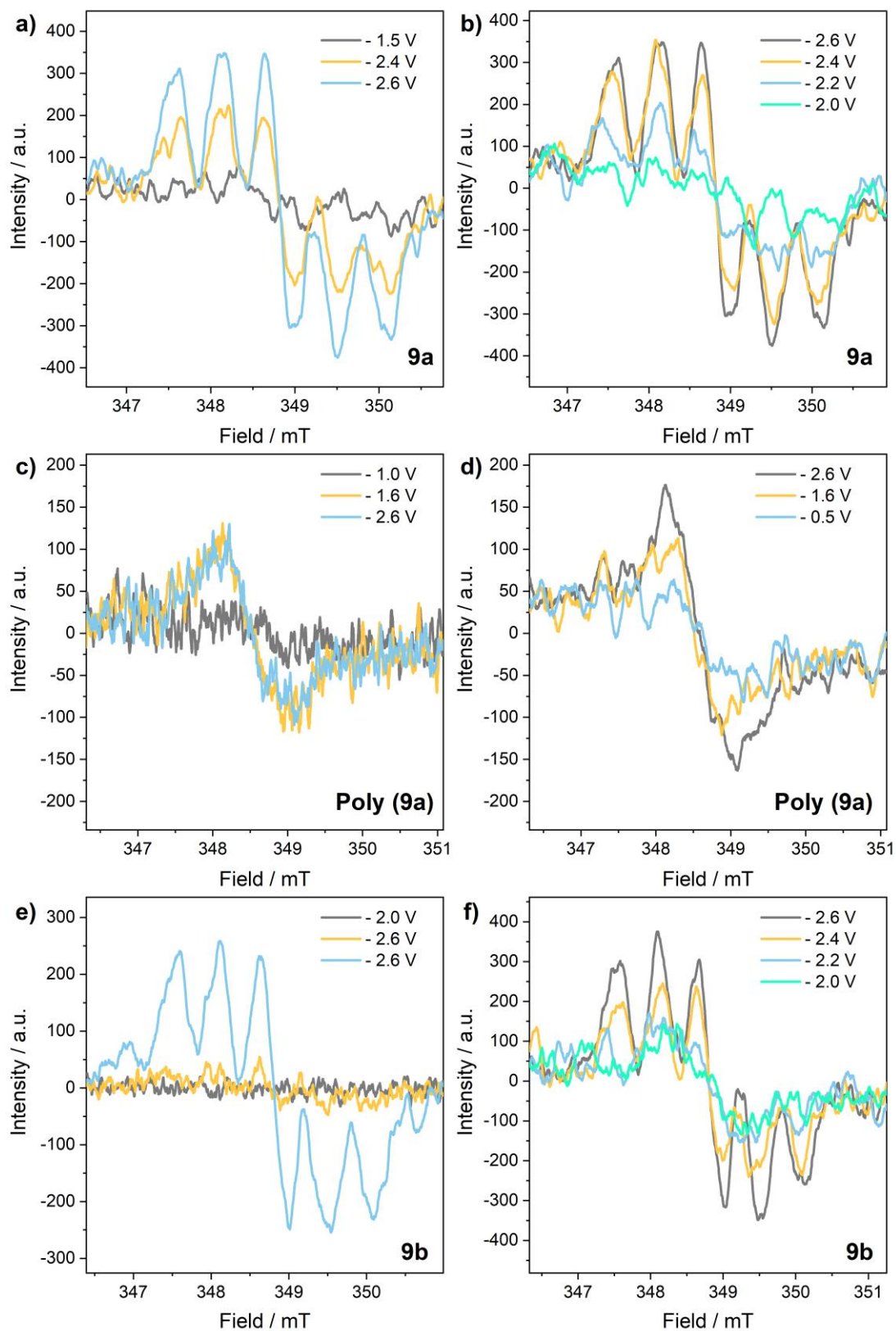
*Figure 47. Potentiostatic EPR spectra for reduction processes during doping of compounds a) **9a**, c) Polymer(**9a**) and e) **9b**; and during dedoping of compounds b) **9a**, d) Polymer(**9a**) and f) **9b**.*

6.2.4. Photoluminescence

6.2.4.1. Solution

Steady-state photophysical properties of compounds **9a** and **9b** in diluted solutions of four different solvents (Toluene, THF, DCM and DMF) were investigated by Prof. Takeda's group and are described in detail in the publication.[10]

However, it is worth mentioning for the discussion of this study that both compounds (i.e. **9a** and **9b**) exhibit shifts in emission wavelength with the change of solvent polarity, as shown in Figure 48, as well as a broadening of the emission spectra profiles with increasing polarity, which indicates the presence of a CT state, corroborating with the theory that CT excited states are stabilized by matrices with higher polarity since to form a CT state is necessary a charge transfer from HOMO to LUMO orbitals, which causes a change in the dipole moment of the compound's structure.
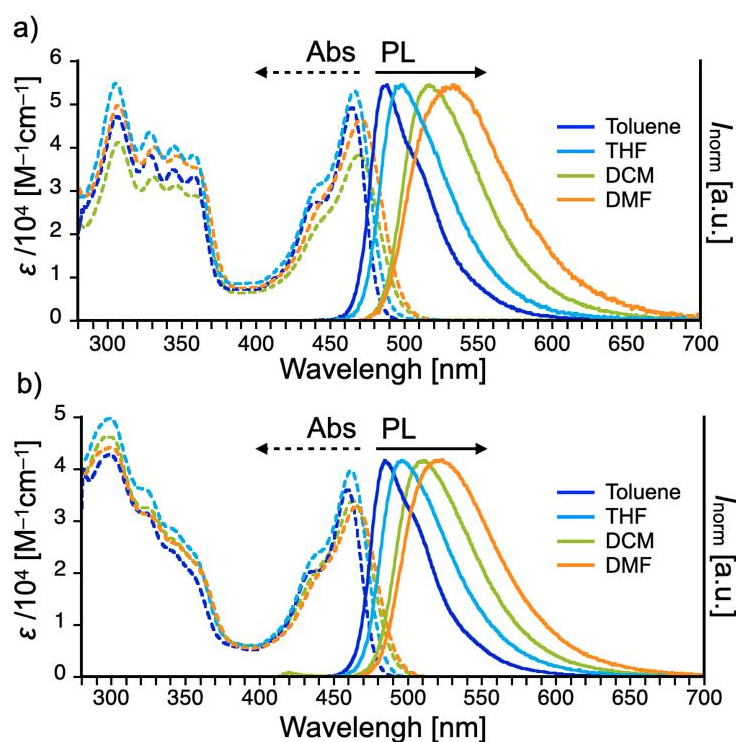
Figure 48. UV-vis absorption and photoluminescence (PL) spectra of diluted solutions of (a) 1 and (b) 2 in various organic solvents (c = 10–5 M, lex = 400 nm)[10]

6.2.4.2. Solid State

For the study of photophysical properties of compounds **9a** and **9b** in the solid-state, the polymer Zeonex® was chosen as a non-polar matrix, and [4,4'-bis(*N*-carbazolyl)-1,1'-biphenyl] (CBP) was selected as the polar matrix, due to the intent of future OLED applications. Furthermore, CBP was selected based on the relations between HOMO and LUMO energy levels of CBP and the compounds analyzed in this study.

Figure 49 displays the photoluminescence spectra of **9a** in **9b** in solid matrices. For both cases in the Zeonex® matrix, the presence of narrow single peaks indicates that the emission originated from a locally excited state (LE). However, in the CBP matrix, broader emission peaks can be observed, which is characteristic of photoluminescence processes that originate from CT excited states.

Although spectra shape and half-width are quite different between the two matrices, the shift in the maximum peak wavelength is very small. This could imply that there is a minimal disturbance in vibronic levels of the compounds even in a more rigid host, such as CBP.

*Figure 49. Photoluminescence spectra of (a) **9a** and (b) **9b** in Zeonex® and CBP matrices (λex=355 nm).*

6.2.5. Time-Resolved Spectroscopic Analysis

The investigation of photoluminescence decay times and ΔE_{ST} values for compounds **9a** and **9b** in Zeonex® and CBP matrices was carried out by time-resolved spectroscopic measurements, with the help of a cryostat, which is capable to reach extremely low temperatures (until 10 K), and an iCCD-gated camera that allows us to choose the desired specific time delays.
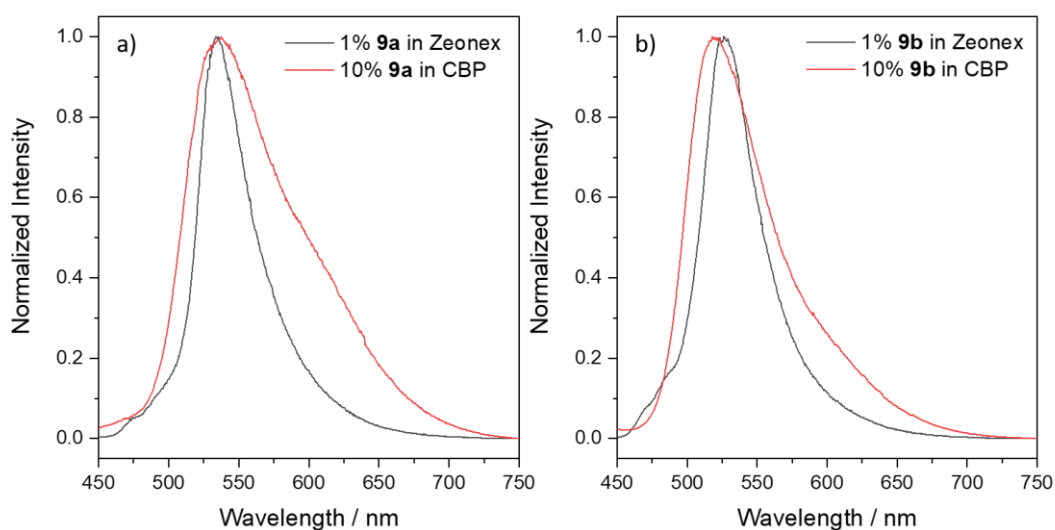
Figure 50 exhibits emission spectra in different time delays and different temperatures. From these spectra, more precisely from the onset wavelength of emission, the energy levels of S_1 and T_1 excited states can be estimated at room temperature (300 K) and 10 K, respectively, as well as the ΔE_{ST} values for compounds **9a** and **9b**. Furthermore, a significant difference in emission properties from the compounds in Zeonex® and CBP matrices can be noticed. Emission spectra observed in nanosecond (ns) time delays are usually attributed to prompt fluorescence (PF) emissions originating from S_1. In the case of measurements of compounds using the Zeonex® matrix (Figure 50a and 50b), at 300 K, a typical PF is observed regarding emission from the singlet localized excited state (^{1}LE). However, in the CBP matrix (Figure 50c and 50d), it can be noticed a very distinct emission wavelength still in the range of the ns regime (5.4 and 16.5 ns), which is attributed to an emission originating from a CT excited state. Such fast emission behaviour is not a usual effect, which may be explained by an emission irradiated from two different conformers with different angles between the two planes of the structure in the 7-membered donor units due to the flexible nature of IDB and ISB groups.
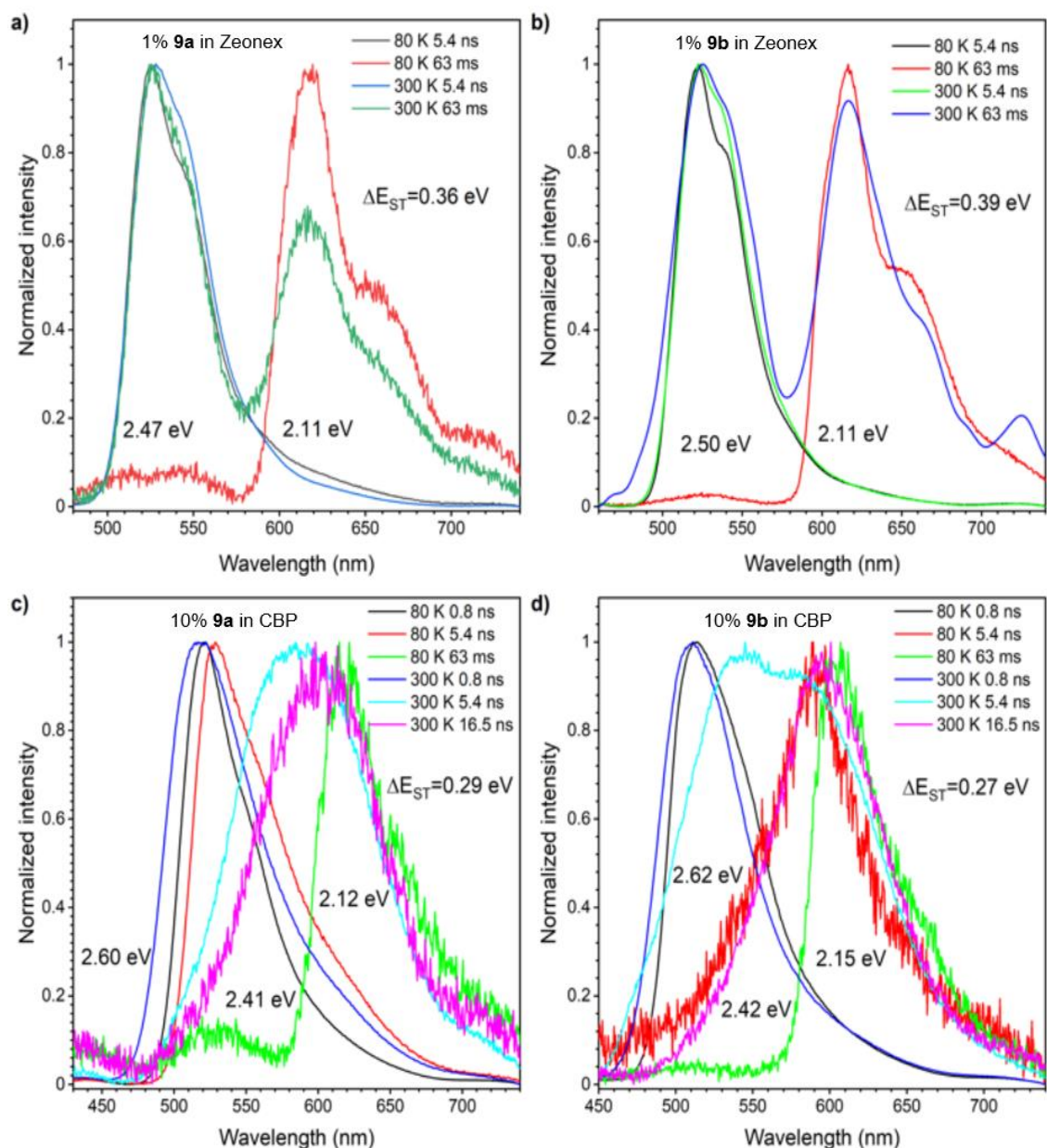
*Figure 50. Time-resolved spectra of 1 wt% of a) **9a** and b) **9b** in Zeonex® and 10 wt% of c) **9a** and d) **9b** in CBP matrix, at varying delay times at 300 K and 80 K.*

Figure 51 presents the plot of the intensity of emission *vs.* the time delays, where it can be easily noticed the two different time regions of photoluminescence decays of compounds **9a** and **9b**. For both compounds in the Zeonex® matrix, emission on the millisecond (ms) time regime was observed at low temperatures and 300 K. These long-lived emission components at 80 K should be attributed to phosphorescence from T_1, and at the onset of these spectra, the energy of the triplet state can be drawn as $E_{T1} = 2.11$ eV in both cases. Compared to analogous compounds containing *t*-BuCz[85] ($E_{T1} = 2.34$ eV)

and DPA ($ET1 = 2.33$ eV)[52] as donor groups, such value reveals a more effective conjugation length for IDB and ISB derivatives.

However, in the ms time regime at 300 K, samples in the Zeonex® matrix display a dual emission behaviour, as shown in Figures 50a and 50b, consisting of emission from the T_1 (i.e. RTP) and delayed fluorescence which probably originated from the singlet ^{1}LE state. Such emission started around 5 ms delay and was observed until 70 ms delay time (Figures 51a and 51b). For the characterization of the type of delayed fluorescence, were conducted measurements of laser pulse influence dependency *vs.* the delayed emission intensity integral (Figure 52), revealing a dependence of slope close to 2, which is characteristic of the bimolecular TTA process.[46]

Emission spectra of samples in the CBP matrix displayed a completely different behaviour. The energies of S_1 are higher when compared to the Zeonex® matrix, by around 0.1 eV, leading to smaller ΔE_{ST} values. Additionally, no delay component was observed in the ms time regime at 300 K (Figures 50c and 50b, Figures 51b and 51d), exclusively typical phosphorescence is noticed at this time regime, at 80 K, which is expected of most organic compounds. This means that no effective rISC occurs between the lowest ^{3}LE and ^{1}CT states, which is unusual for compounds with smaller ΔE_{ST} compared to the Zeonex® samples. Such effect may be explained by emission originating from two different molecular conformers, with no direct connection in between, which was also observed by the fast emission behaviour in Figure 50. In contrast, the *t*-BuCz analogue compound presented a moderate rISC, owning a similar ΔE_{ST} value (0.33 in CBP)[85], yielding TADF properties.
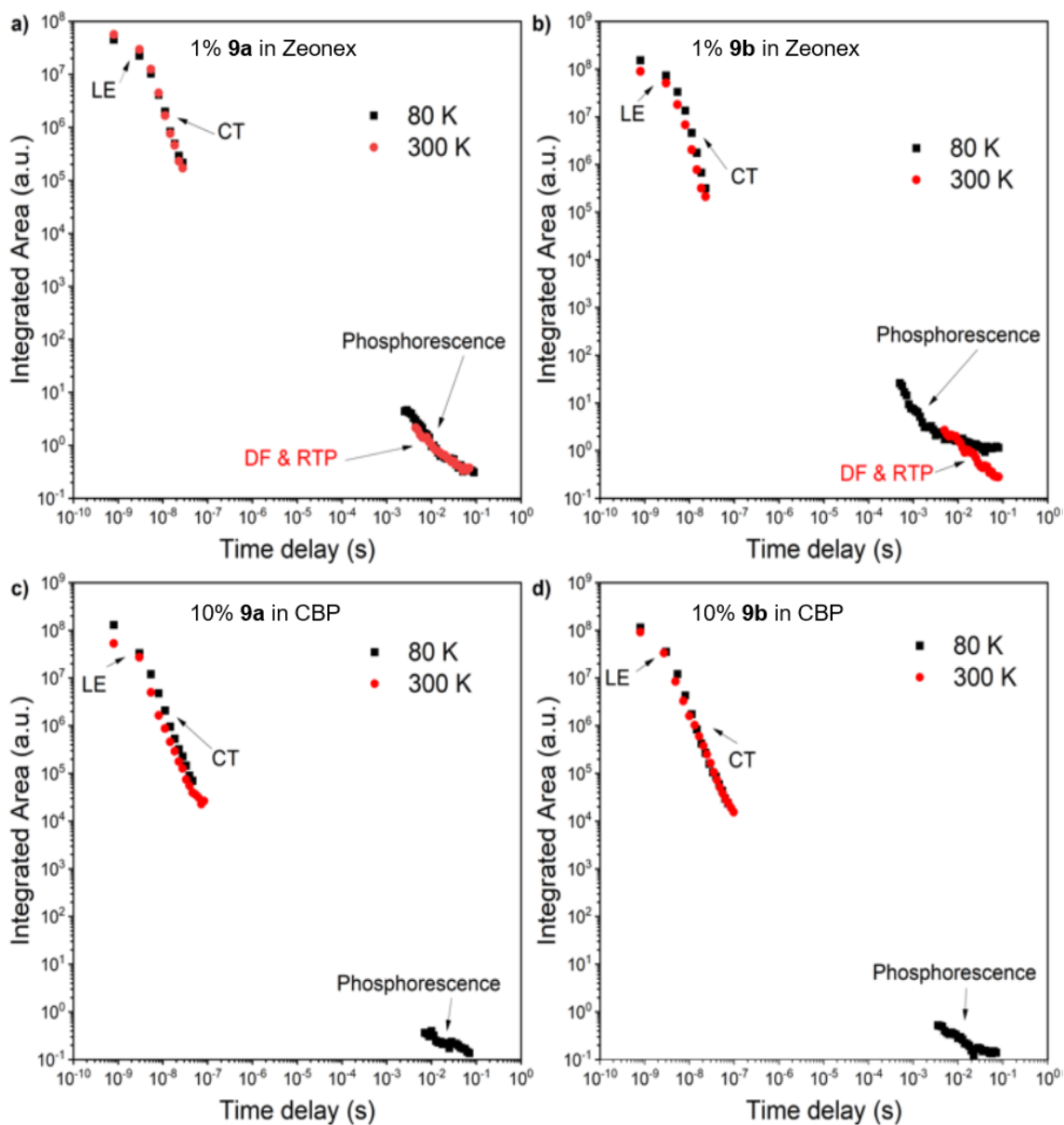
*Figure 51. Transient decay of 1 wt% of a) **9a** and b) **9b** in Zeonex® matrix, and transient decay of 10 wt% of c) **9a** and d) **9b** in CBP matrix at different temperatures.*
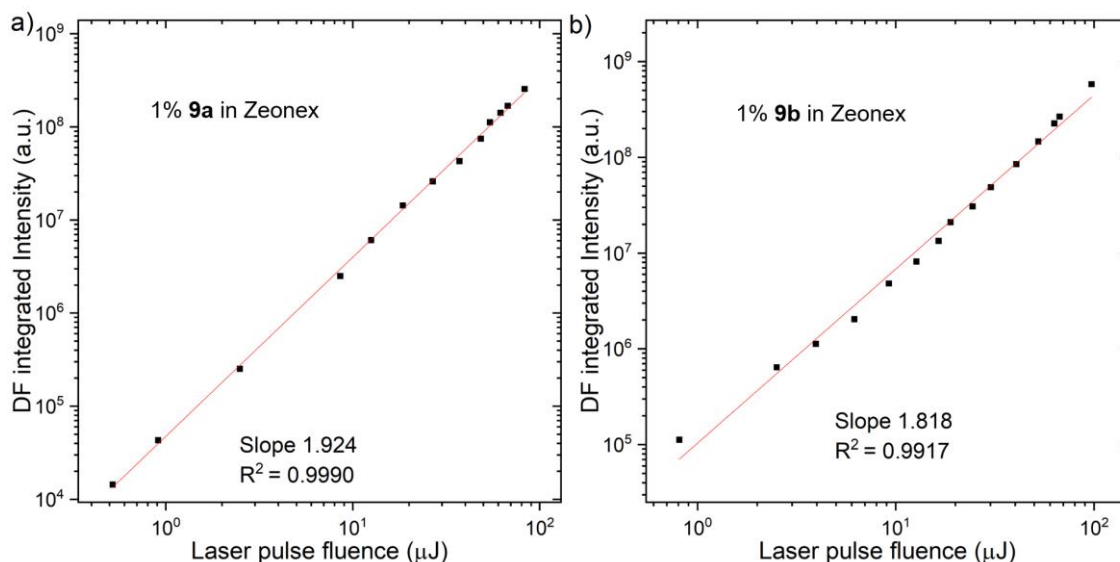
*Figure 52. Integrated emission intensity vs laser pulse energy (μJ) of 1% a) **9a** and b) **9b** in Zeonex® matrix at 300 K at a delay time of 5 ms.*

6.2.6. Electroluminescent Devices

OLED devices containing compounds **9a** and **9b** within the emitting layers were fabricated with the following configuration: ITO/NPB [*N,N'*-di(1- naphthyl)-*N,N'*-diphenyl-(1,1'-biphenyl)-4,4'-diamine] (40 nm)/10% 1 and 2 in CBP (20 nm)/TPBi. As seen in Figure 53, measurements of such devices' characterisation revealed moderate EQE values of 1.94% and 2.5% for **9a** and **9b,** respectively (Figure 53b). As well as higher EQE, the luminance of the device constructed with compound **9b** was also higher (6,300 cd/m^2) than that with compound **9a** (5,500 cd/m^2). Although unfortunately, the OLED device based on emitter **9b** presented a higher roll-off effect, which is observed by the faster decay on EQE for the red curve in Figure 53b, compared to the device containing compound **9a**. The more intense roll-off effect can be explained by the sigma-dimer formation inside the emitter layer during the device functioning, an effect already observed in different systems in previous reports.[29] Turn-on voltage values were found to be around 6.0 V for both OLED devices, which are slightly high values.

Compared to the OLED devices fabricated with the analogous compounds *t*-BuCz (EQE = 8%)[85] and DPA (EQE = 12%)[52], EQE values for IDB and ISB derivatives are quite low due to the lack of TADF properties.
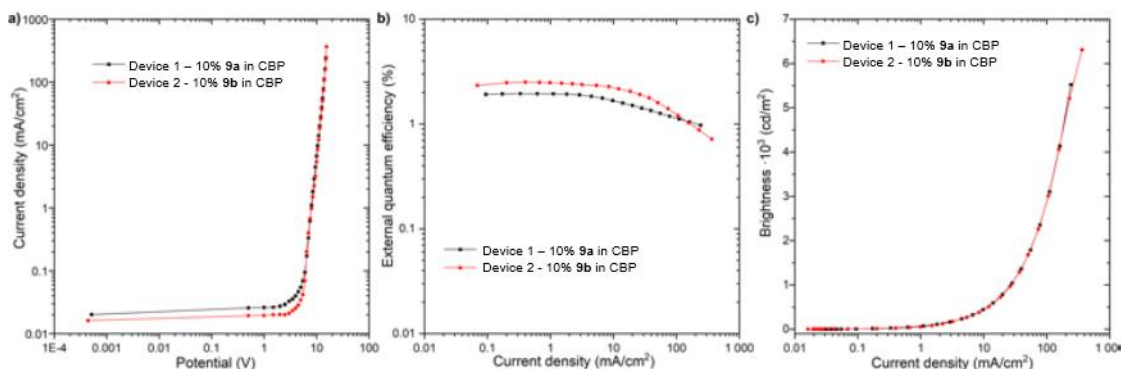
Figure 53. OLED device characteristics.

6.3. Conclusions

In collaboration with the group that synthesized the dibenzo[a,j]phenazine-cored donor–acceptor–donor (D–A–D) triads having C2-homologues of carbazole electron-donors, a complete study and investigation of their physicochemical properties was carried out, revealing the effect of replacing Cz with conformationally more flexible 7-membered aromatic amines (IDB and ISB).

This study presented a full electrochemical and spectroelectrochemical UV-Vis and NIR and potentiostatic EPR analysis, revealing the unique electropolymerization and dimerization phenomena of the studied D–A–D systems.

The insertion of the C2-bridge within the Cz donors granted a drastic change in the photophysical behaviour from a moderate TADF observed in the Cz analogue to a dual emission comprising RTP and delayed fluorescence caused by a TTA process.

Although compared to analogous compounds, the OLED devices fabricated did not present such interesting functioning properties due to the lack of TADF behaviour, this study might open up the way to understand and develop other stimuli-responsive organic functional materials in the future.

102

7. Photophysical Characterization of Organic Emitters Based on Concaved N-PAHs with Tunable TADF/RTP Properties

7.1. Introduction

Polycyclic aromatic hydrocarbons (PAHs) are nothing more than organic compounds containing only hydrogen and carbon, comprising multiple aromatic rings. With simple structures, as two aromatic rings fused, there is naphthalene, with three: anthracene, and so on, as presented in some examples in Figure 54.
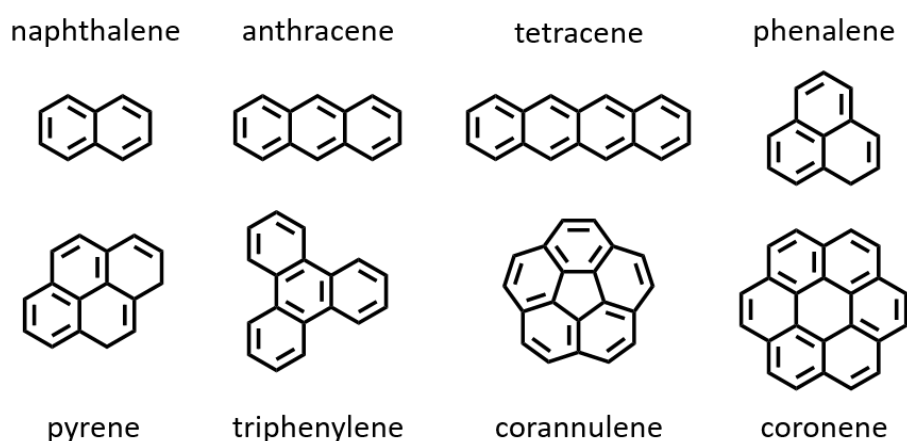
Figure 54. Example of polycyclic aromatic hydrocarbons (PAHs).

Due to strongly delocalized electrons in the aromatic rings, they became highly interesting for application in the most diverse areas, with remarkable potential for chemical sensors,[117] organic solar cells,[118] liquid crystals[119,120] and organic light-emitting diodes.[121]

In some cases, like naphthalene, anthracene and even coronene, all the hydrogen and carbon atoms share the same geometrical plane, forming a molecular planar structure. However, in some cases, molecules like corannulene, such as the 5-membered ring in the middle of the structure, force all the other atoms to a bowl shape structure to minimize the bond stress.[122]

One of the main reasons for observing non-planar geometry and conformation in such systems is the interaction of added substituents.[123] In fact, the addition of distinct substituents into PAH structures leads to changes in their fluorescence properties, modulating solubility in different solvents, emission intensity, and singlet-triplet energy gap (ΔE_{ST}).[124]

The molecular shape, size, and curvature of such materials have a great influence on fluorescence and electronic properties. Curved PAHs were found to produce strong dipole moments determined by the number of aromatic rings.[125] Through the investigation of charge-carrier conductivity of indenocorannulene derivatives, Wang *et al.* reported improved electronic transport characteristics due to the presence of carbon-rich π-bowls, stating interesting properties to serve as active materials in organic electronics.[126]

The introduction of nitrogen atoms to the centre of the polycyclic framework leads to concaved or bowl-shaped three-dimensional architectures. Nitrogen-doped (N-doped) PAHs present improved photophysical characteristics with interesting properties for application in organic electronic devices.[127,128]

As discussed in Chapter 3, TADF emission is extremely determined by structural modifications, especially by specific conformations in D-A systems. Through the simple addition of a methyl substituent into acceptor or donor moieties, it is possible to produce distinct conformers, allowing for tuning between different emission pathways, such as RTP and TADF, for example, as described in the work of Chen *et al.*, in 2018.[15] Additionally, it has been reported the significant influence of using nitrogen compounds as donor moieties, as the C-N bond gives the appropriate angular conformation to obtain the desired properties. And for that reason, nitrogen donors have been widely used in the search for TADF behaviour.[9,15,39,51,52]

Extensive research was done looking for the optimization of synthetic methodologies of N-doped curved PAHs,[129–132], resulting in the achievement of desired concaved and boat-like conformations with promising structural alignment.[133–136] However, deeper investigations in structural modifications are still missing, aiming to tailor excited states' energy to produce more efficient materials.

One of the fundamental criteria for the efficient design of novel TADF emitters is to achieve a small singlet-triplet gap (ΔE_{ST}) to induce a fast endothermic rISC process, converting triplets into singlet excitons, which is a spin-forbidden process. Materials with D-A π-conjugated structures with accurate angles between D and A moieties can provide such small gaps and mixed CT and LE character, which will assist rISC, increasing its probability and rate constant. Consequently, in the last decades, there has been a vast interest in small, planar and branched D-A compounds, which result in limited photophysical properties for the derived materials.[137]

As shown in Figure 55, a nitrogen atom positioned at the centre of the curved bowl-shaped frame consists of the donor moiety, which exhibits intrinsic electron-donating properties. The addition of slightly distinct strong acceptors containing different peripherical substituents results in Donor-Acceptor structures with minimal spatial overlap between frontier orbitals, assured by an anti-aromatic seven-membered ring (represented as green in Figure 55). Using such structures aims to achieve weak oscillator strength for HOMO – LUMO transitions.
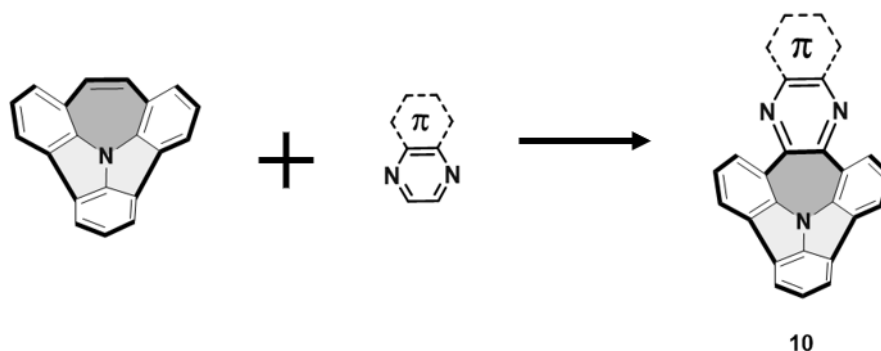
Figure 55. The structural idea of donor-acceptor compounds.

With the help of Dr Marcin Lindner's research group at the Polish Academy of Sciences in Warsaw – Poland, where they specialize in synthetic strategies of novel compounds, the synthesis of new nitrogen-based PAHs was developed with new nitrogen-based PAHs Donor-Acceptor electronic structures, compounds **10a-n**, presented in Figure 56. The main idea of such a study is to observe the influence of molecular structure modification on the photophysical properties as a way of being able to achieve tunable photophysical properties.
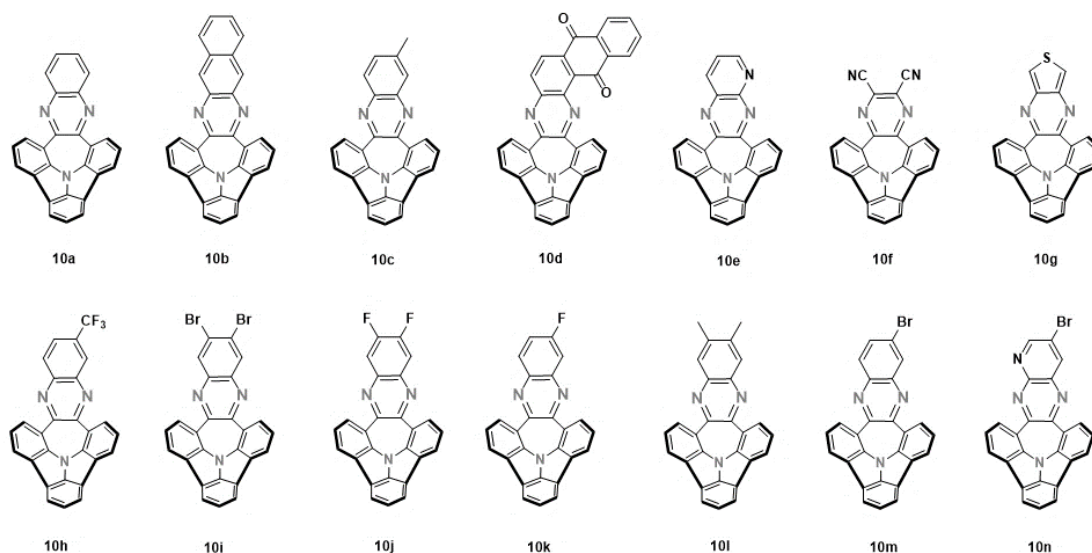
*Figure 56. Molecular structures of compounds **10a-n**.*

The project in partnership yielded an article, which was accepted in the Angewandte Chemie Internationa Edition. Herein in this chapter, my contribution to the study will be discussed, including mainly the photophysical characterization and the application of such compounds in the structure of optoelectronic devices and the discussion of the results.

7.2. Results and Discussion

7.2.1. Electrochemical Studies

As usual, the first step in investigating a new set of compounds is the study of electrochemical behaviour through CV measurements of compounds **10a**-**n**, as shown in Figure 57.
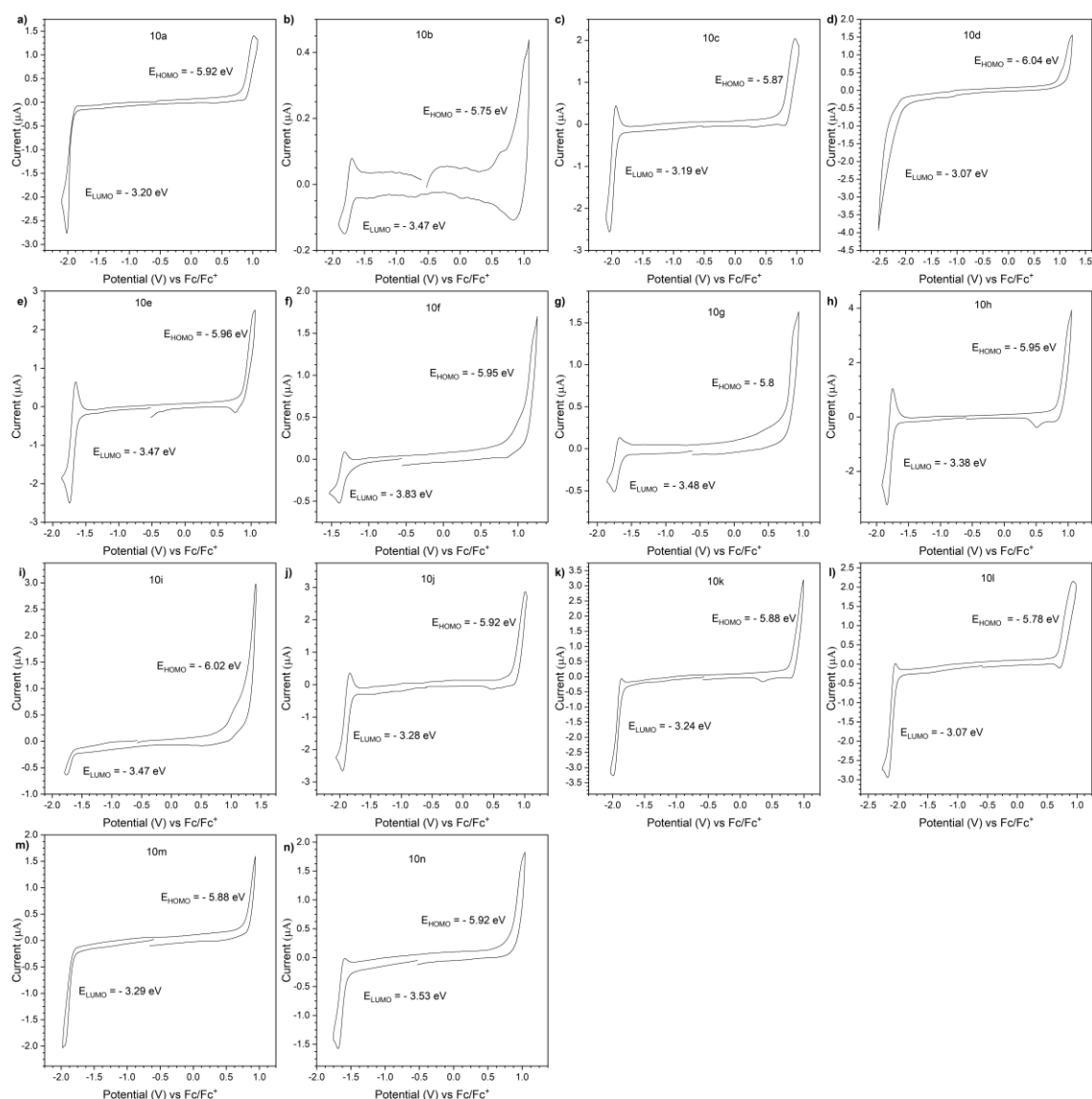
*Figure 57. The first scan of a CV of compounds **10a-n** in 0.1 M Bu₄NBF₄ in DCM electrolyte at the scan rate of 50 mV s⁻¹. Concentrations vary between 0.2 – 1 mM.*

As the first obstacle of this study, many compounds exhibit low solubility in DCM, DMF THF and acetonitrile solvents typically used for CV analysis.[70] The insoluble character of some compounds is noticed as low current, low resolution and noisy signals like the ones presented in Figure 57i (compound **10i**) or 57d, for example, regarding the most insoluble compounds of all, compound **10d**.

In the voltammograms in Figure 57, regarding the first cycle of oxidation and reduction for each compound, it can be noticed that half of the compounds (**10b**, **10c**, **10e**, **10f**, **10g**, **10h** and **10j**) displayed a reversible reduction peak. All compounds exhibit semi or completely irreversible oxidation peaks.

From the parameters obtained through CV measurements, it is possible to determine the HOMO and LUMO energy levels, as shown in the diagram in Figure 58.
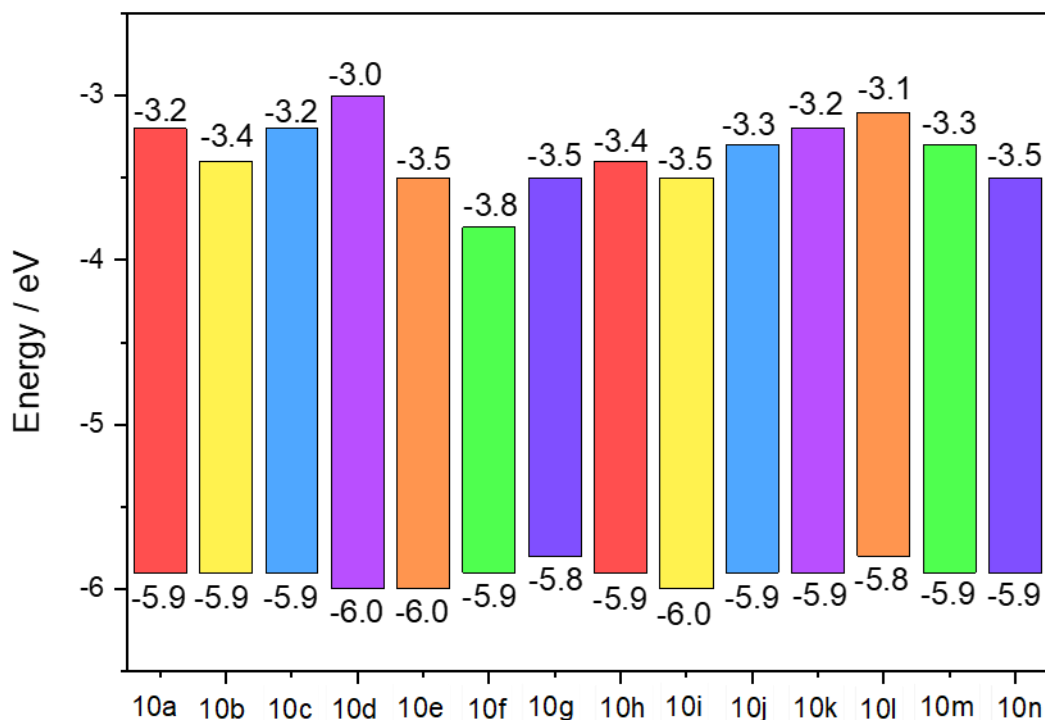
Figure 58. HOMO and LUMO energy levels of compounds 10a-n.

Arising out of the comparison between electrochemical behaviours, the effect of structural modification on the frontier orbital's energy levels can be estimated. Since this series of compounds is based on structures that share the same donor while varying the acceptor part, the values of HOMO energy levels are very similar for the 14 compounds, ranging only between -5.8 and -6.0 eV.

Compound **10a** is considered the primary structure, and all the other compounds can be compared to it, as substituents' presence will influence the acceptor's electronic character. The obtained values for LUMO levels exhibit a more considerable variation. The addition of a phenyl group (compound **10b**) increases the conjugation length, decreasing the energy of LUMO for -3.4 eV in comparison to compound **10a** (-3.2 eV). A stronger effect is observed for the presence of an additional nitrogen atom (compound **10e**), with -3.5 eV. Compound **10f** presents the lowest LUMO energy level (-3.8 eV), regarding the strongest acceptor character, deriving from two nitrile groups. The addition of halogen substituents exhibited lower LUMO levels, with a stronger effect for di-bromine (**10i**) and di-fluorine (**10j**) substitutions. The addition of one and two methyl groups (compounds **10c** and **10l**) does not influence the acceptor characteristic of the materials. Compound

10d displayed the highest LUMO level (-3.0 eV), having an anthraquinone as a substituent at the acceptor part of the structure.

7.2.2. Photoluminescence

7.2.2.1. Solution

As the first step of the photophysical characterization, UV-Vis absorbance measurements for compounds **10a-n** in 3 different solvents (DCM, THF and toluene) are represented as the curves at lower wavelengths in Figure 59. Next, the solvatochromism study was done by comparing the emission of these compounds in solvents of different polarities, as depicted in Figures 59a-n.

Most of the compounds present a slight red shift with increasing polarity, as well as a different profile shape noticed in toluene solutions, regarding the presence of two overlap signals. Such behaviour indicates that the emission originated from LE excited states; therefore, in toluene solutions, emission from ^{1}LE. On the other hand, emissions derived from CT states exhibit a shape of a Gaussian distribution, like the spectra acquired from solutions in solvents with higher polarity.[53] Hence, compounds **10a-n** in DCM and THF solutions present emissions from a ^{1}CT excited state. The small bathochromic shift related to different polarities can be justified by mixed character between ^{1}LE and ^{1}CT states involved in the emission process.

Compound **10d** (Figure 59d) is the only one to exhibit a significant red shift in DCM solutions, with CT character while presenting emission from ^{1}LE in THF and toluene solutions.
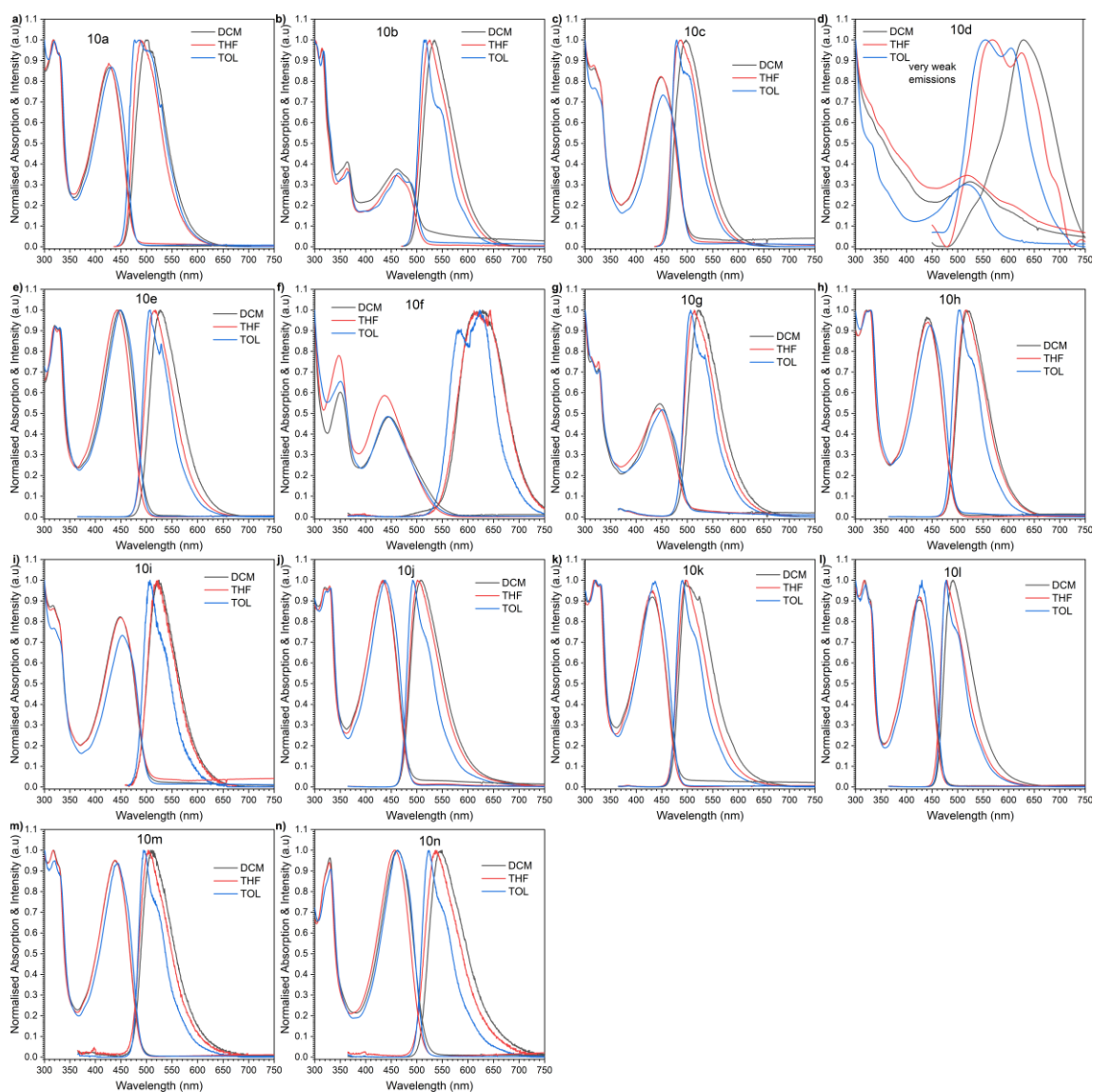
*Figure 59. UV-vis absorption and PL spectra of **10a-n** (c 10^{-5} M) diluted solutions in dichloromethane, tetrahydrofuran, and toluene solvents.*

Comparing the spectra of more similar compounds allows us to understand the influence of structure modification on excitation and emission properties based on the acceptor's electronic features. Shifts to higher wavelengths represent emission processes that require less energy to occur. For example, there is a significant bathochromic shift from **10a** to **10b** (Figures 59a and 59b), with additional phenyl groups leading to an increase in conjugation. When comparing **10a** with **10e** (Figures 59a and 59e), the same effect is noticed now with the addition of a nitrogen atom in the acceptor's structure. Compounds with halogen substitutions exhibit less significant shifts. However, it can be seen that the presence of two bromine groups (compound **10i**, Figure 59i) led to two times larger shift than the mono substituted compound (**10m**, Figure 59m). Mono- and di-fluorine

substituted compounds, **10k** and **10j** (Figures 59k and 59j), respectively, present similar behaviour. The highest bathochromic shift was observed due to the addition of nitrile groups in compound **10f** (Figure 59f).

7.2.2.2. Solid State

The confirmation that triplet excited states are involved in the emission mechanism is done by means of degassing experiments. In this case, the degassing study was carried out in solid layers of 1 wt% of compounds **10a**-**n** in Zeonex® matrix, deposited in sapphire disc substrates, and the resulted spectra are displayed in Figure 60.

Nearly all compounds exhibit a significant increase in emission intensity under degassed environments, although compounds **10f** and **10i** (Figures 60f and 60i) did not. More significant increases are related to the higher contribution of triplet excited states in the overall emission.[49] The largest rises were observed for compounds **10b**, **10d,** and **10e** (Figures 60b, 60d, and 60e), regarding acceptor moieties containing an extra phenyl group, anthraquinone and nitrogen atom, respectively.

An interesting effect is observed in compounds **10j** and **10m** (Figures 60j and 60m). Under vacuum conditions, only one of two signals exhibits an intensity rise, which may indicate RTP character. In the case of TADF behaviour, the emission signal can be observed in airy environments and increases substantially under a vacuum. In contrast, RTP emission is barely noticed until there is no presence of oxygen, which in that case will appear as a signal with normal intensity, as seen in the example in Figure 60m.
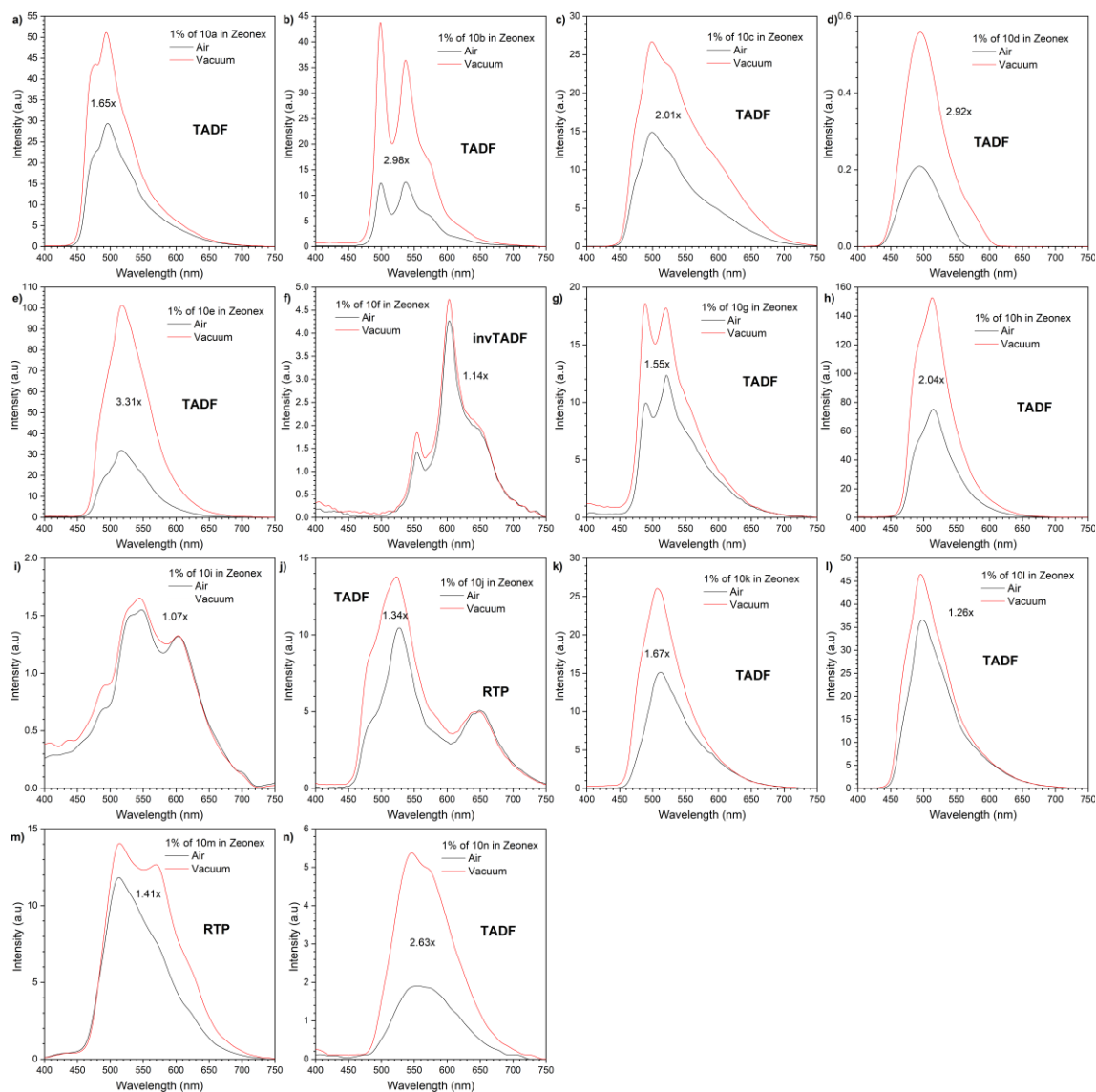
Figure 60. a) Emission spectra of 10a-n in Zeonex® matrix under air (black) and in vacuum (red) (λex = 355 nm). Solid layers were deposited in sapphire disc substrates.

7.2.3. Time-Resolved Spectroscopic Analysis

As the system for iCCD-gated spectroscopic measurements with He cryostat is very time-consuming, and this is a study of fourteen compounds, a different approach was used to accelerate the achievement of results. Therefore, in this chapter, to obtain iCCD-gated spectroscopic measurements, an N_2-cryostat was used, which works faster than the He cryostat. However, it is very important to mention that a cryostat that uses liquid nitrogen for the cooling system can only achieve the lowest temperature, around 70 K.

Once the use of different polarity matrices induces emission pathways deriving from different excited states, for a better understanding of the emission properties and characteristics, the studies were carried out using a polar (CBP) and a less polar host (Zeonex® polymer).

Although in previous chapters, the emission onset was used to determine the energy values of the excited states, which originate the emission mechanisms, in this chapter, the emission maxima are employed to calculate energy levels of S_1 and T_1.

Figure 61 displays the time-resolved spectra of compounds **10a-n** in Zeonex® matrix, acquired in different delay times, at 80 and 300 K.
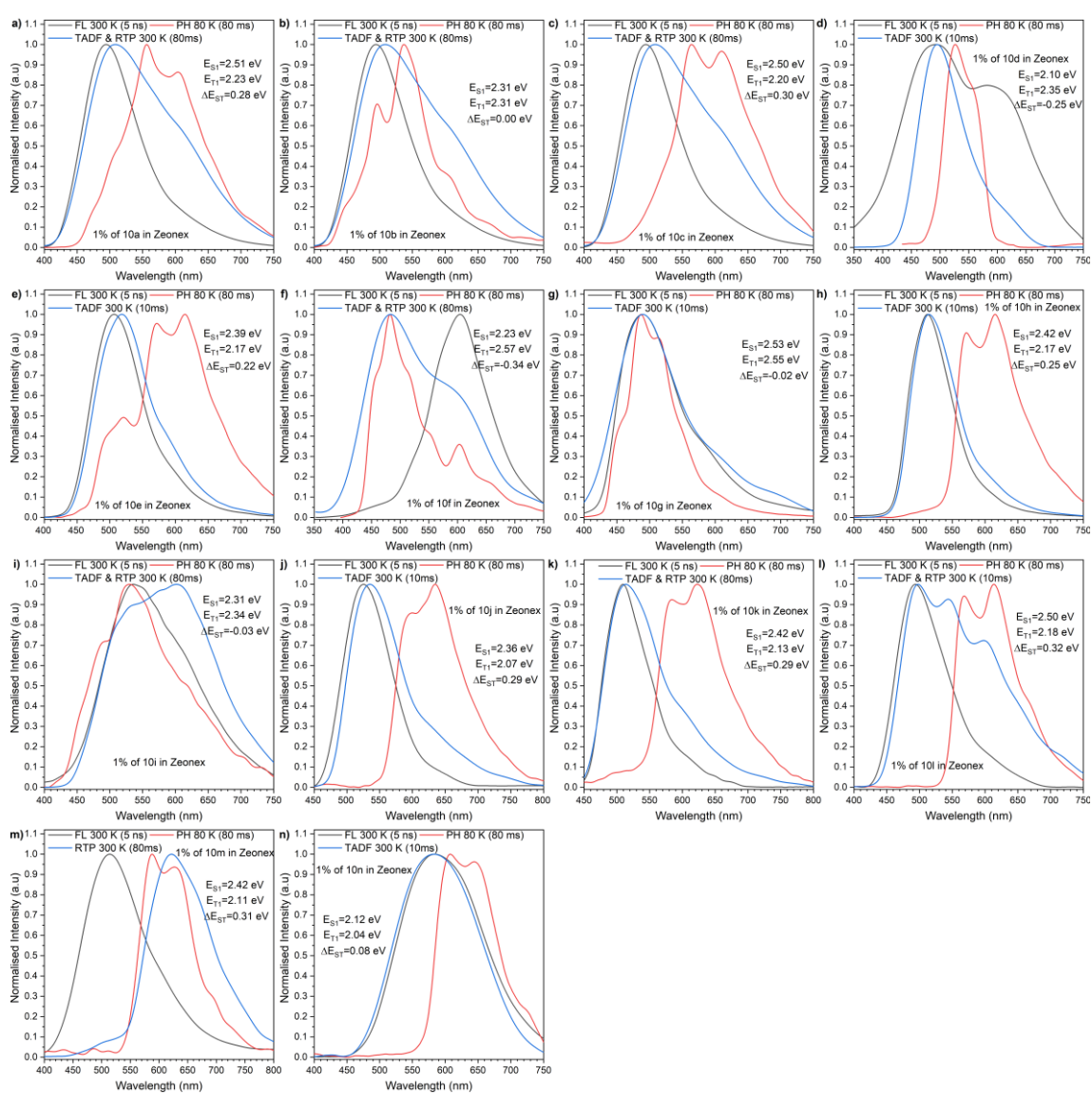
*Figure 61. Time-resolved spectra of a) – n) 1 wt% of compounds **10a-n** in Zeonex®*
matrix, at varying delay times at 300 K and 80 K.

The emission maxima of prompt fluorescence spectra are similar for samples in Zeonex® matrix (Figure 61) and toluene solution (Figure 59).

The smaller ΔE_{ST} gap (0 eV) was observed for compound **10b** (Figure 61), with an additional phenyl group at the acceptor's unit, increasing the conjugation length and decreasing the charge transfer energy. Compounds **10g** and **10i** presented the second and third smallest ΔE_{ST} gaps, being 0.02 and 0.03 eV, respectively. The addition of a thiophene ring seems to influence the triplet energy state in compound **10g**, exhibiting one of the highest T_1 energy levels.

The most significant difference was observed for the excited states' energy values of compound **10n**, which contain an additional bromine substituent compared to compound **10e** or an additional nitrogen atom when compared to compound **10m**. The combination of these two additions lowered T_1 and S_1 energy levels extremely.

For materials presenting TADF behaviour, through the study of their emission spectra varying stepwise from extremely low temperatures up to 300 K, it is possible to determine the point where the thermal activation occurs. For further investigation and characterization of the observed emission characteristics, compounds' emission spectra were collected at different time delays, varying from ns to ms time regime, as displayed in Figure 62. In summary, the energy values for excited states involved in the emission mechanisms were calculated and are depicted in the diagram in Figure 63.

*Figure 62. Transient decay of 1 wt% of **10a**-**n** in Zeonex® matrix at 300 K, insets are the respective spectra for particular delay time*

Nearly all compounds in the Zeonex® matrix have emissions with TADF behaviour. However, compounds **10d**, **10e**, **10g**, **10h** and **10n** exhibit pure TADF emission, while in the case of compounds **10a**, **10b**, **10c**, **10f**, **10i** and **10l,** a mix of TADF and RTP mechanisms are involved in the overall emission.

Compound **10m**, containing a mono-bromine substitution, is the only one to present a pure RTP emission. When compared to **10n**, it indicates that adding a nitrogen atom to the benzene ring leads to a change in pure TADF emission. Besides, the presence of a second bromine group (**10i**) generates a mixed TADF and RTP character.
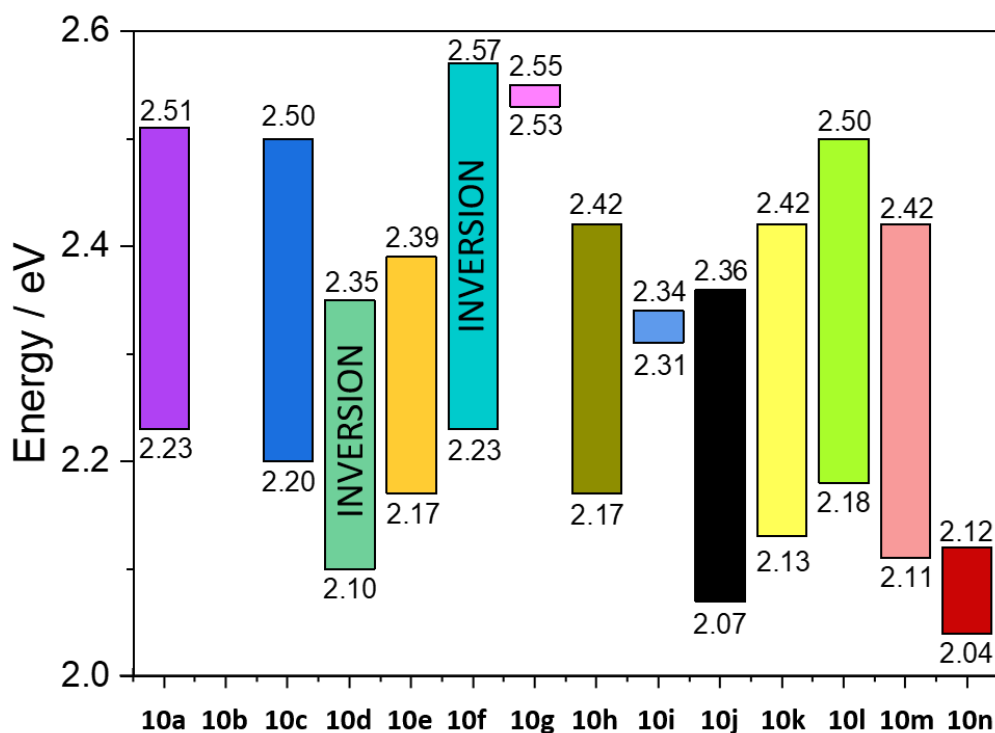
*Figure 63. Diagram of singlet and triplet energy levels for samples containing 1 wt% of compounds **10a-n** in Zeonex® matrix.*

The most interesting behaviour is noticed for compounds **10d** and **10f** (Figures 61d, 61f, 62d and 62f), which exhibit T_1 energy levels higher than S_1, known as a singlet-triplet inversion. In the case of compound **10d,** it may be not so obvious to observe such an effect because its prompt fluorescence exhibits two signals with maxima at 494 and 590 nm (Figure 61d). However, as shown in Figure 62d, the first signal (494 nm) disappears around 10 ns of delay time, and only the signal at 590 nm remains, which means that this second signal is related to the energy of the lowest singlet excited state. Compound **10f** also displays a singlet-triplet inversion, although in this case is more easily seen as the phosphorescence spectrum (represented as a red line in Figure 61f) occurs in lower wavelengths than the prompt fluorescence spectrum (black line in Figure 61f). In addition, a mixed TADF and RTP emission is observed from compound **10f** (Figure 62f).

As shown in Figure 62m, compound **10m** presents TADF emission at µs time regime, while at 0.2 ms delay time, the emission signal starts shifting and pure RTP is observed. Similar behaviour is noticed for compound **10f** (Figure 62f), which exhibits pure TADF emission at the µs range, and mixed TADF and RTP emission at the ms time regime.

In addition to the Zeonex® matrix samples, solid layers of 10 wt% of compounds **10a-n** in the CBP matrix were investigated. CBP was chosen as the host to evaluate the emissive properties of the compounds as active layers in OLED structures. Figure 64 displays the time-resolved spectra for compounds **10a-n** in the CBP matrix, acquired in different delay times, at 80 and 300 K. The plot of emission intensity *vs.* delay times is presented in Figure 65, and the diagram in Figure 66 displays the energy levels of the excited states involved in the emission process in a more illustrative way.
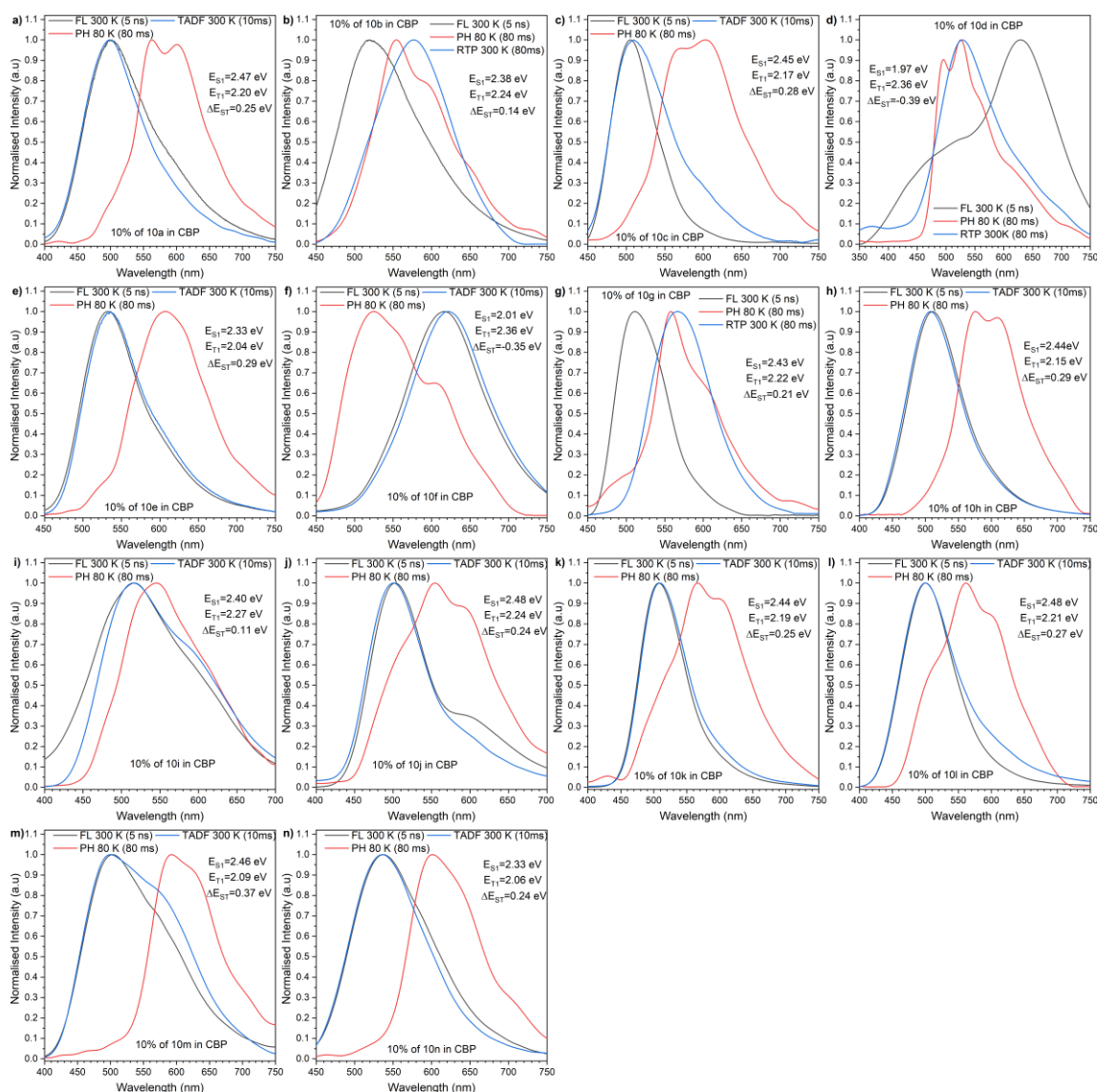
*Figure 64. Time-resolved spectra of a) – n) 1 wt% of compounds **10a-n** in CBP matrix, at varying delay times at 300 K and 80 K.*

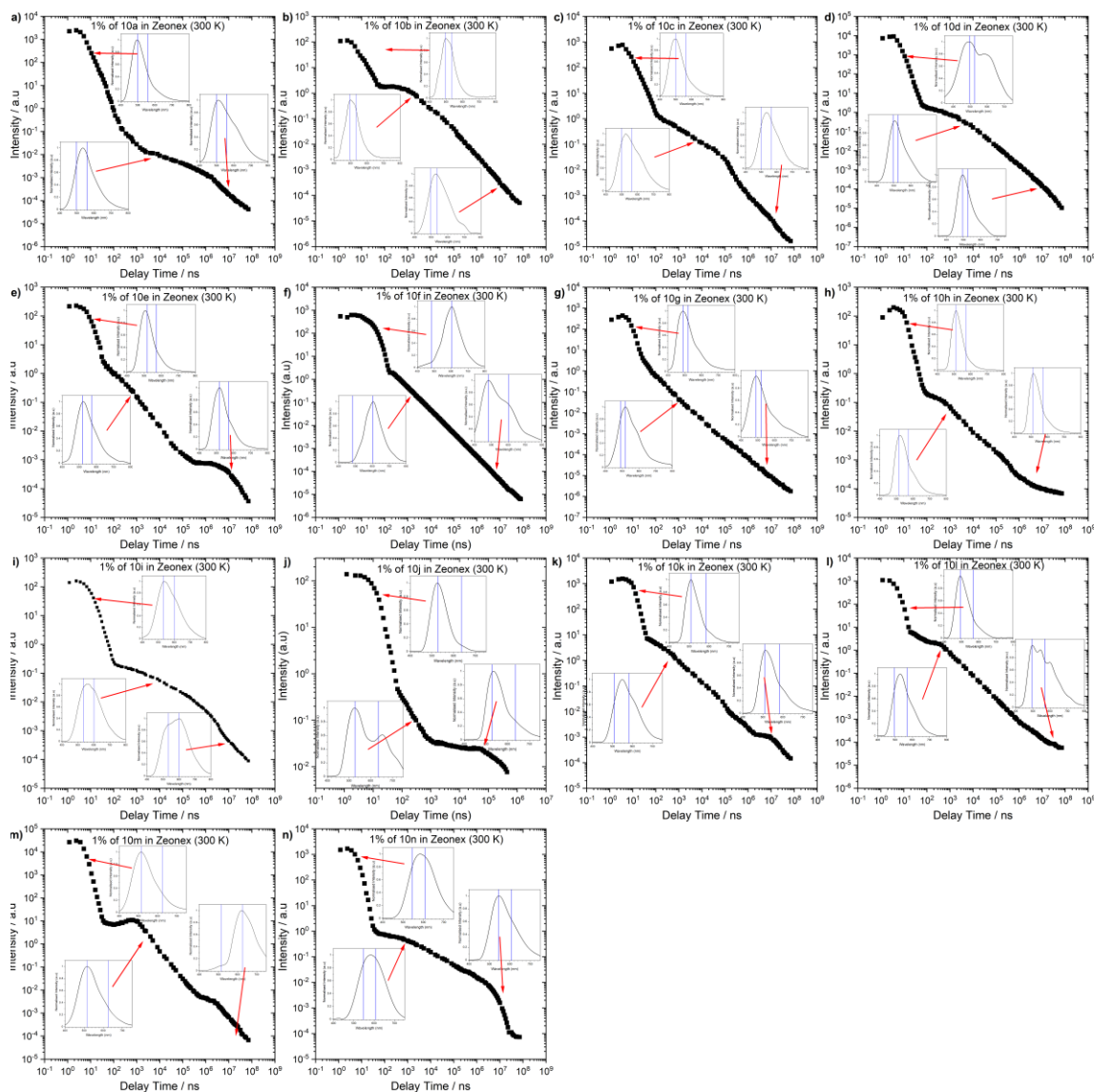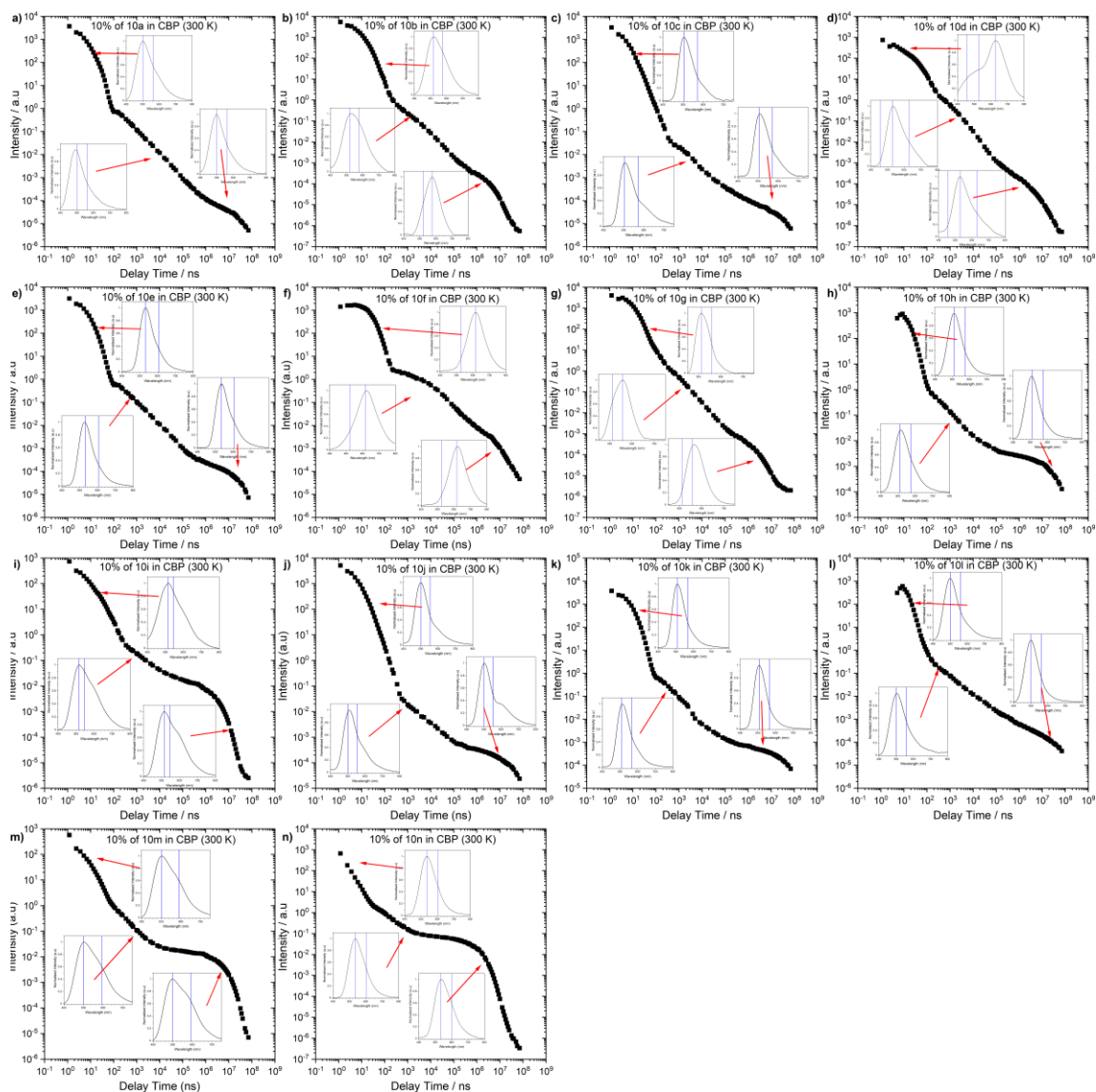*Figure 65. Transient decay of 10 wt% of **10a**-**n** in CBP matrix at 300 K, insets are the respective spectra for particular delay time.*

In Figures 64 and 65, it is noticed that the great majority of the compounds analyzed in the CBP matrix exhibit pure TADF emission, being them **10a**, **10e**, **10f**, **10h**, **10i**, **10j**, **10k**, **10l** and **10n**. Additionally, pure RTP behaviour was detected for compounds **10b**, **10d**, and **10g,** while mixed RTP and TADF character was observed only from **10c** and **10m**.
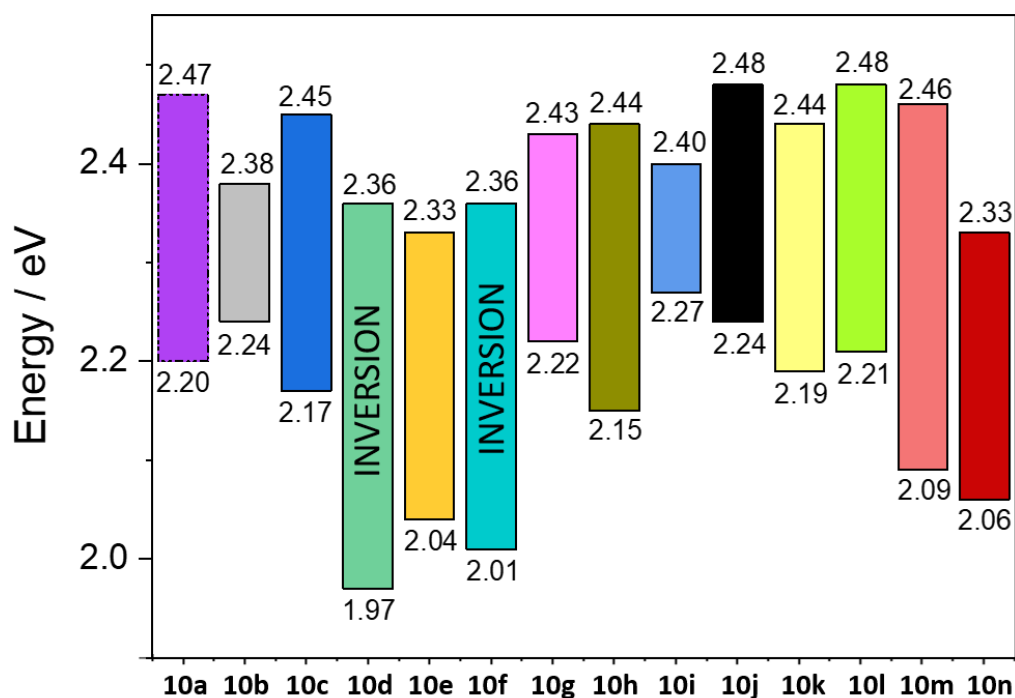
*Figure 66. Diagram of ΔE$_{ST}$ levels for samples containing 1 wt% of compounds **10a-n** in CBP matrix.*

The effect of singlet-triplet inversion is still observed for compounds **10d** and **10f**. However, the emission behaviour from these compounds displayed very distinct characteristics from Zeonex® and CBP matrices. Compounds **10a**, **10c**, **10f** and **10i**, which presented emission with RTP and TADF mixed character in Zeonex®, turned into pure TADF in the polar matrix. Other emitters with mixed features, **10m** and **10b**, exhibit pure RTP in the presence of CBP. Moreover, **10g** and **10d**, pure TADF emitters in Zeonex® matrix, have pure RTP behaviour in the CBP host.

Comparing the diagrams in Figures 63 and 66, we notice that the energy of triplet excited states of compounds 10d, 10e, and 10g had a significant drop with CBP compared with results in the Zeonex® matrix. In contrast, the singlet states were less affected by the host effect, leading to increased values of ΔE$_{ST}$. A more significant difference is noticed for compound **10g**, exhibiting a gap ten times bigger.

The increase of ΔE$_{ST}$ observed for compounds **10d** and **10g** is enough justification for the deactivation of the TADF process, turning into pure RTP emitters.

Compound **10f** exhibits a similar stabilization of triplet excited states, however, the presence of CBP host decreases the energy of the singlet excited state with the same intensity.

The null bandgap for compound **10b** in Zeonex® turns 140 meV in CBP. Along with the separation of TADF and RTP behaviours, which could not be observed isolated in the non-polar host. Though in CBP matrix exhibit TADF emission starting at μs time regime, shifting to pure RTP behaviour observed at 0.2 ms delay time, as shown in Figure 65b. Regarding application in OLEDs, lifetimes in the ms range are considered long-lived, which are known for increasing the roll-off efficiency.[30] Nevertheless, the two other pure RTP emitters, **10d** and **10g** displayed RTP behaviour at μs delay times, which is an interesting future considering the applicability as emitter layer in OLED devices.

The results from the analysis, calculations and interpretations are summarized in Table 6, containing values of PLQY, a lifetime of prompt (τPF) and delayed fluorescence (τDF), the ratio between delayed and prompt fluorescence (DF/PF), energy levels of singlet (S_1) and triplet (T_1) excited states involved in the emission, as well as the ΔE_{ST} values for compounds **10a-n** in Zeonex® and CBP matrices.

When investigating TADF and RTP mechanisms, one of the most important factors to be determined is the DF/PF ratio, which is related to the triplet state contribution to the emission process. If the ratio is equal to 3 or higher values, it means that 100% of the generated triplet excited states were involved in the overall observed emission.[137] The DF/PF ratios for compounds in the Zeonex® matrix higher than three were found for compounds **10b**, **10e**, **10h**, **10i**, **10j**, **10k**, **10l** and **10n**, with the highest ratio value of 21.49 given for **10b**.

In comparison to the values in Zeonex®, a decrease in the DF/PF ratio for most compounds with CBP matrix is noticed. Although, compounds **10m** and **10n** displayed impressive ratios of 65.43 and 62.10, respectively.

Unfortunately, the most interesting compounds of this study so far, the RTP emitters with a short lifetime, **10d** and **10g**, exhibit RTP emission weaker than the overall emission, resulting in ratios above zero (0.43 and 0.18).

Table 6. Summary of the general photophysical properties of the emitter compounds.

Emitter	λ_{em},	Host	PLQY	τ_{PF},	τ_{DF},	τ_{Ph},	DF/PF	S_1	T_1,	ΔE_{ST}
	nm[a]		(%)[b]	ns[c]	µs[d]	ms[d]		eV[f]	eV[f]	eV[g]
10a	493	Zeonex	10	3.89±0.15	10.81±0.9	1.80±0.10	1.01	2.51	2.23	0.28
	502	CBP	17	5.14±0.19	3.55±0.34	-	0.20	2.47	2.20	0.26
10b	536	Zeonex	35	5.22±0.37	1.82±0.12	9.23±0.83	21.49	2.31	2.31	0.00
	519	CBP	45	7.82±0.25	3.52±0.38	1.21±0.18	0.14	2.38	2.24	0.15
10c	497	Zeonex	8	4.96±0.23	2.47±0.12	5.97±0.57	2.80	2.50	2.20	0.30
	505	CBP	16	3.87±0.18	1.63±0.16	-	0.20	2.45	2.17	0.28
10d	497	Zeonex	2	3.04±0.04	7.43±0.65	-	0.46	2.10	2.35	-0.25
	456	CBP	16	15.68±0.91	2.42±0.30	-	0.43	1.97	2.36	-0.39
10e	519	Zeonex	36	6.95±0.38	4.30±0.49	-	8.17	2.39	2.17	0.22
	519	CBP	37	5.32±0.17	1.58±0.20	-	0.37	2.33	2.04	0.29
10f	555	Zeonex	6	25.42±1.12	0.94±0.06	-	0.35	2.23	2.57	-0.34
	617	CBP	86	23.74±1.14	1.00±0.09	-	1.89	2.01	2.36	-0.35
10g	490	Zeonex	2	4.73±0.38	0.96±0.08	-	0.38	2.53	2.55	-0.02
	511	CBP	29	7.80±0.17	0.58±0.02	0.72±0.07	0.18	2.43	2.22	0.20
10h	513	Zeonex	50	8.22±0.88	3.99±0.41	-	3.90	2.42	2.17	0.25
	507	CBP	37	9.41±0.24	1.60±0.11	-	5.30	2.44	2.15	0.29
10i	536	Zeonex	0.4	8.26±0.25	1.03±0.12	1.60±0.04	14.40	2.31	2.34	-0.03
	517	CBP	9	7.42±0.18	1.22±0.08	-	10.02	2.40	2.27	0.12
10j	525	Zeonex	18	<mark>10.02±0.42</mark>	2.78±0.37	-	3.05	2.36	2.07	0.29
	500	CBP	19	5.35±0.14	12.98±0.9	-	0.32	2.48	2.24	0.24
10k	511	Zeonex	17	7.74±0.75	1.20±0.13	-	3.06	2.42	2.13	0.29
	508	CBP	19	5.83±0.21	1.75±0.18	-	0.94	2.44	2.19	0.25
10l	495	Zeonex	12	3.10±0.13	0.66±0.05	6.70±0.73	4.36	2.50	2.18	0.32
	500	CBP	16	7.57±0.09	1.31±0.11	-	2.07	2.48	2.21	0.27
10m	512	Zeonex	1	3.07±0.31	1.58±0.14	3.12±0.23	0.73	2.42	2.11	0.31
	503	CBP	17	5.57±0.36	0.79±0.08	-	65.43	2.46	2.09	0.37
10n	546	Zeonex	2	4.05±0.02	1.98±0.18	-	13.14	2.12	2.04	0.08
	532	CBP	30	1.03±0.08	0.86±0.06	-	62.10	2.33	2.06	0.26

7.2.4. Electroluminescent Devices

At last, the compounds were applied in the fabrication of OLED devices. The device structure was optimised based on the previously studied electrochemical bandgap and HOMO and LUMO values. The structural configuration was done as follows: ITO/NPB [*N,N'*-di(1-naphthyl)-*N,N'*-diphenyl-(1,1'-biphenyl)-4,4'-diamine] (40 nm)/TSBPA [4,4'-(diphenylsilanediyl)bis(*N,N*-diphenylaniline)] (10 nm)/10% of **10a-n** in CBP (20 nm)/TPBi [2,2',2''-(1,3,5-benzinetriyl)-tris(1-phenyl-1-H-benzimidazole)] (50 nm)/LiF (1 nm)/Al (100 nm). The fabricated devices **10a-n** were characterized, and the results are shown in Figure 67.

Devices **10d** and **10g** displayed RTP behaviour, while all the other devices presented electroluminescence characteristics of TADF emission.

The device with the highest EQE value was based on emitter **10h** (11.5%, Figure 66e), with a trifluoromethyl group in its structure. The second highest EQE (10%) was given by the device containing emitter **10f** with double nitrile substitution, which exhibits singlet-triplet inversion. The smallest EQE values were obtained by devices with compounds **10c** and **10j**, with one methyl and di-fluorine substitutions, respectively, including a more significant roll-off effect. Finally, among the RTP based OLEDs, the device with emitter **10g** (thiophene derivative) displayed the highest EQE of 3.1%.

As seen in Figure 67c, the highest luminance value was achieved by the OLED containing emitter 10f, up to 24,680 cd/m^2. Furthermore, the RTP OLED based on **10g** obtained luminance values up to 10,250 cd/m^2.

The analysis of characteristics of the OLED devices revealed a significant increase in OLED efficiency depending on the structure. Through the observation of Figures 67b and 67e, the comparison of devices based on emitters **10a** and **10b** leads to the conclusion that an additional phenyl ring increases EQE 2.5 times. The insertion of a nitrogen atom resulted in an EQE 2 times larger (between **10a** and **10e**), whereas the addition of one bromine group led to a four times increase (between **10a** and **10n**).
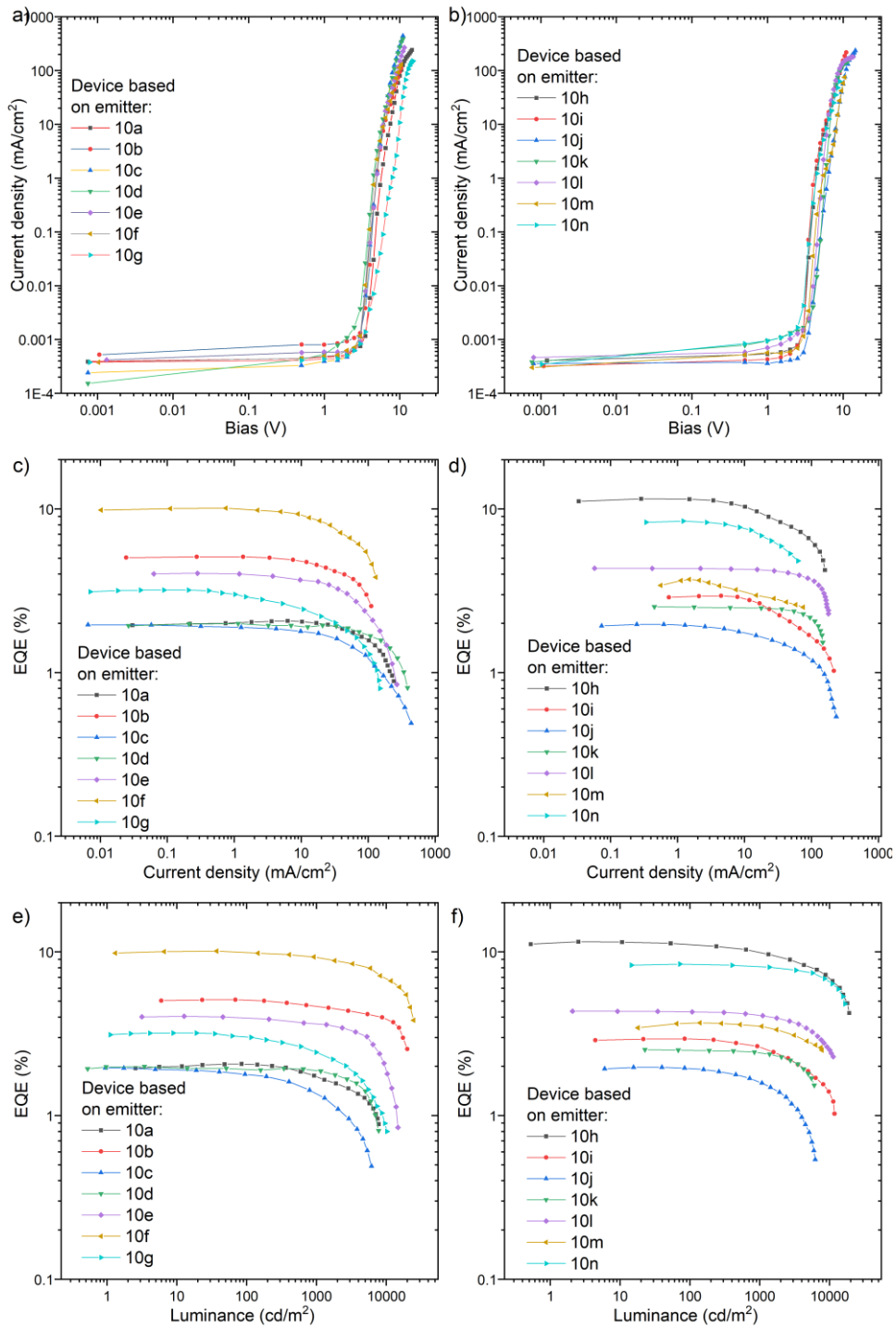
*Figure 67. The characteristics of the OLED devices are based on emitters **10a-n**. a), b) Current density-bias characteristics. c), d) EQE-current density characteristics. e), f) EQE - luminance characteristics.*

7.3. Conclusions

Herein was reported the investigation of electrochemical and photophysical properties of nitrogen-doped polycyclic aromatic hydrocarbons (N-PAHs), with intrinsic D-A electronic structures and bowl-shaped curvature. Despite a complete fused system, it comprises moderate to weak oscillator strength for HOMO-LUMO transitions and small ΔE_{ST} due to the presence of an anti-aromatic seven-membered ring. In contrast, the acceptor's strength influences PLQY amplification up to 86%.

The comparative study of emission characteristics of fourteen different compounds afforded a better understanding of the tuning between thermally activated delayed fluorescence (TADF), room-temperature phosphorescence (RTP), or dual TADF & RTP behaviours, depending on the substituent group on the acceptor's structure.

The assembly of TADP/RTP OLEDs with such materials provided yellow to orange emissions for the first time observed in N-PAH systems, achieving EQEs as high as 11.5%, good operational stabilities, and low roll-off processes.

The most interesting feature displayed by some of these emitters was the singlet-triplet inversion, which should enable the energy transfer from triplet to singlet excited states, accelerating the process. In particular, compound **10f**, with remarkably high PLQY (86.4%), produced an OLED device with high efficiency (EQE>10%) and a very efficient TADF process.

8. References

1.   Andrews, F. A Short History of Electric Light. https://www.debook.com/Bulbs/lightbulbs.htm (2005).

2.   Holonyak, N. & Bevacqua, S. F. COHERENT (VISIBLE) LIGHT EMISSION FROM Ga(As $1-$ x P x) JUNCTIONS . *Semicond. Devices Pioneer. Pap.* **82**, 898–899 (1991).

3.   Allen, J. W. & Cherry, R. J. Some properties of copper-doped gallium phosphide. *J. Phys. Chem. Solids* **23**, 509–511 (1962).

4.   Dutta, P. S. & Liotta, K. M. Full Spectrum White LEDs of Any Color Temperature with Color Rendering Index Higher Than 90 Using a Single Broad-Band Phosphor. *ECS J. Solid State Sci. Technol.* **7**, R3194–R3198 (2018).

5.   Narukawa, Y., Ichikawa, M., Sanga, D., Sano, M. & Mukai, T. White light emitting diodes with super-high luminous efficacy. *J. Phys. D. Appl. Phys.* **43**, (2010).

6.   Tang, C. W. & VanSlyke, S. A. Organic electroluminescent diodes. *Appl. Phys. Lett.* **51**, 913 (1987).

7.   Zhu, H. *et al.* Printable Semiconductors for Backplane TFTs of Flexible OLED Displays. *Adv. Funct. Mater.* **30**, 1–36 (2020).

8.   Qiu, X. *et al.* Novel 12,12-dimethyl-7,12-dihydrobenzo[a]acridine as a deep-blue emitting chromophore for OLEDs with narrow-band emission and suppressed efficiency roll-off . *J. Mater. Chem. C* (2021) doi:10.1039/d1tc03898b.

9.   Data, P. & Takeda, Y. Recent Advancements in and the Future of Organic Emitters: TADF- and RTP-Active Multifunctional Organic Materials. *Chem. - An Asian J.* **14**, 1613–1636 (2019).

10.   Zimmermann Crocomo, P. *et al.* The Impact of C2 Insertion into a Carbazole Donor on the Physicochemical Properties of Dibenzo[a,j]phenazine-Cored Donor–Acceptor–Donor Triads. *Chem. - A Eur. J.* **27**, 13390–13398 (2021).

11.   Ahn, D. H. *et al.* Highly efficient blue thermally activated delayed fluorescence

emitters based on symmetrical and rigid oxygen-bridged boron acceptors. *Nat. Photonics* **13**, 540–546 (2019).

12. Lee, D. R. *et al.* Above 30% external quantum efficiency in green delayed fluorescent organic light-emitting diodes. *ACS Appl. Mater. Interfaces* **7**, 9625–9629 (2015).

13. Liu, Y., Li, C., Ren, Z., Yan, S. & Bryce, M. R. All-organic thermally activated delayed fluorescence materials for organic light-emitting diodes. *Nat. Rev. Mater.* **3**, (2018).

14. Tao, Y. *et al.* Thermally activated delayed fluorescence materials towards the breakthrough of organoelectronics. *Adv. Mater.* **26**, 7931–7958 (2014).

15. Chen, C. *et al.* Intramolecular Charge Transfer Controls Switching Between Room Temperature Phosphorescence and Thermally Activated Delayed Fluorescence. *Angew. Chemie - Int. Ed.* **57**, 16407–16411 (2018).

16. The Editors of Encyclopaedia Britannica. Bioluminescence. https://www.britannica.com/science/bioluminescence.

17. Pope, M., Kallmann, H. P. & Magnante, P. Electroluminescence in organic crystals. *J. Chem. Phys.* **38**, 2042–2043 (1963).

18. Mitschke, U. & Bäuerle, P. The electroluminescence of organic materials. *J. Mater. Chem.* **10**, 1471–1507 (2000).

19. Adachi, C., Tsutsui, T. & Saito, S. Organic electroluminescent device having a hole conductor as an emitting layer. *Appl. Phys. Lett.* **55**, 1489–1491 (1989).

20. Wei, X. & Gu, B. *Optical Imaging in Human Disease and Biological*.

21. Jabłoństski, A. Efficiency of anti-stokes fluorescence in dyes [6]. *Nature* **131**, 839–840 (1933).

22. Yersin, H. Triplet Emitters for OLED Applications. Mechanisms of Exciton Trapping and Control of Emission Properties. 1–26 (2004) doi:10.1007/b96858.

23. Adachi, C., Baldo, M. A., Thompson, M. E. & Forrest, S. R. Nearly 100% internal phosphorescence efficiency in an organic light emitting device. *J. Appl. Phys.* **90**, 5048–5051 (2001).

24. Wassenberg, D. *Triplet states - triplet fates : phosphorescence and energy Triplet States – Triplet Fates Phosphorescence and Energy Transfer in Functional Molecules*. (2006). doi:10.6100/IR614648.

25. Jou, J. H., Kumar, S., Agrawal, A., Li, T. H. & Sahoo, S. Approaches for fabricating high efficiency organic light emitting diodes. *J. Mater. Chem. C* **3**, 2974–3002 (2015).

26. de Sa Pereira, D., Monkman, A. P. & Data, P. Production and characterization of vacuum deposited organic light emitting diodes. *J. Vis. Exp.* (2018) doi:10.3791/56593.

27. Liu, L. *et al.* Two-In-One Method for Graphene Transfer: Simplified Fabrication Process for Organic Light-Emitting Diodes. *ACS Appl. Mater. Interfaces* **10**, 7289–7295 (2018).

28. He, G. *et al.* High-efficiency and low-voltage p-i-n electrophosphorescent organic light-emitting diodes with double-emission layers. *Appl. Phys. Lett.* **85**, 3911–3913 (2004).

29. Data, P. *et al.* Evidence for Solid State Electrochemical Degradation Within a Small Molecule OLED. *Electrochim. Acta* **184**, 86–93 (2015).

30. Yersin, H., Rausch, A. F., Czerwieniec, R., Hofbeck, T. & Fischer, T. The triplet state of organo-transition metal compounds. Triplet harvesting and singlet harvesting for efficient OLEDs. *Coord. Chem. Rev.* **255**, 2622–2652 (2011).

31. Nagashima, K. & Velan, S. S. Understanding the Singletand Triplet States inMagnetic Resonance. *Concepts Magn. Reson. Part A* **42A**, 165–181 (2013).

32. Chen, C. H. *et al.* New carboline-based donors for green exciplex-forming systems. *J. Chinese Chem. Soc.* **68**, 482–490 (2021).

33. Segal, M., Baldo, A., Holmes, J., Forrest, R. & Soos, G. Excitonic singlet-triplet ratios in molecular and polymeric organic materials. *Phys. Rev. B - Condens. Matter Mater. Phys.* **68**, 1–14 (2003).

34. Endo, A. *et al.* Thermally activated delayed fluorescence from Sn4+-porphyrin complexes and their application to organic light-emitting diodes -A novel mechanism for electroluminescence. *Adv. Mater.* **21**, 4802–4806 (2009).

35. Jacko, A. C. & Powell, B. J. Electronic correlations in organometallic complexes. *Chem. Phys. Lett.* **508**, 22–28 (2011).

36. Mai, S. *et al.* Quantitative wave function analysis for excited states of transition metal complexes. *Coord. Chem. Rev.* **361**, 74–97 (2018).

37. Smith, A. R. G., Burn, P. L. & Powell, B. J. Spin-orbit coupling in phosphorescent iridium(III) complexes. *ChemPhysChem* **12**, 2429–2438 (2011).

38. Kim, S. Y. *et al.* Organic light-emitting diodes with 30% external quantum efficiency based on a horizontally oriented emitter. *Adv. Funct. Mater.* **23**, 3896–3900 (2013).

39. Kaji, H. *et al.* Purely organic electroluminescent material realizing 100% conversion from electricity to light. *Nat. Commun.* **6**, 2–9 (2015).

40. Wang, Y. *et al.* Comprehensive Investigation into Luminescent Properties of Ir(III) Complexes: An Integrated Computational Study of Radiative and Nonradiative Decay Processes. *Inorg. Chem.* **57**, 6561–6570 (2018).

41. *Photoluminescent MAterials and Electroluminescent Devices*. (Springer International Publishing AG 2017, 2017). doi:10.1007/978-3-319-59304-3_2.

42. Tanaka, D., Agata, Y., Takeda, T., Watanabe, S. & Kido, J. High luminous efficiency blue organic light-emitting devices using high triplet excited energy materials. *Japanese J. Appl. Physics, Part 2 Lett.* **46**, 3–6 (2007).

43. Zanoni, K. P. S., Ito, A., Grüner, M., Murakami Iha, N. Y. & De Camargo, A. S. S. Photophysical dynamics of the efficient emission and photosensitization of [Ir(: Pqi)2(NN)]+ complexes. *Dalt. Trans.* **47**, 1179–1188 (2018).

44. Sainsbury, P. Iridium's spectacular surge underpinned by hydrogen hype and supply cuts. https://materials-risk.com/iridiums-spectacular-surge-underpinned-by-hydrogen-hype-and-supply-cuts/ (2021).

45. Hobson, P. Tight supply and hydrogen hopes drive iridium up 160%. https://www.reuters.com/article/us-precious-iridium-idUSKBN2AC1DG (2021).

46. Krishna, V. G. Delayed fluorescence due to triplet-triplet annihilation: A theoretical study. *J. Chem. Phys.* **46**, 1735–1739 (1967).

47. Parker, C. A. & Hatchard, C. G. Triplet-singlet emission in fluid solutions. Phosphorescence of eosin. *Trans. Faraday Soc.* **57**, 1894–1904 (1961).

48. Maciejeski, A., Szymanski, M. & Steer, R. P. Thermally Activated Delayed S1 Fluorescence of Aromatic Thiones. *J. Phys. Chem.* **90**, 6314–6318 (1986).

49. Pander, P. & Dias, F. B. Photophysical Characterisation of Thermally Activated Delayed Fluorescence (TADF) Materials. *Disp. Imaging* **2**, 249–263 (2017).

50. Dias, F. B. *et al.* The role of local triplet excited states and D-A relative orientation in thermally activated delayed fluorescence: Photophysics and devices. *Adv. Sci.* **3**, 1–10 (2016).

51. Chen, J.-X. *et al.* Red/Near-Infrared Thermally Activated Delayed Fluorescence OLEDs with Near 100% Internal Quantum Efficiency. *Angew. Chemie - Int. Ed.* **58**, 14660 – 14665 (2019).

52. Okazaki, M. *et al.* Thermally activated delayed fluorescent phenothiazine-dibenzo[a,j]phenazine-phenothiazine triads exhibiting tricolor-changing mechanochromic luminescence. *Chem. Sci.* **8**, 2677–2686 (2017).

53. Gao, Y. *et al.* Hybridization and de-hybridization between the locally-excited (LE) state and the charge-transfer (CT) state: A combined experimental and theoretical study. *Phys. Chem. Chem. Phys.* **18**, 24176–24184 (2016).

54. Kumar, M., Ribeiro, M. & Pereira, L. New Generation of High Efficient OLED Using Thermally Activated Delayed Fluorescent Materials. in *Light-Emitting Diode - An Outlook On the Empirical Features and Its Recent Technological Advancements* (ed. Jagannathan Thirumalai) (IntechOpen, 2018). doi:10.5772/intechopen.76048.

55. Etherington, M. K., Gibson, J., Higginbotham, H. F., Penfold, T. J. & Monkman, A. P. Revealing the spin-vibronic coupling mechanism of thermally activated delayed fluorescence. *Nat. Commun.* **7**, 1–7 (2016).

56. De Silva, P. Inverted Singlet-Triplet Gaps and Their Relevance to Thermally Activated Delayed Fluorescence. *J. Phys. Chem. Lett.* **10**, 5674–5679 (2019).

57. Ehrmaier, J. *et al.* Singlet-Triplet Inversion in Heptazine and in Polymeric Carbon Nitrides. *J. Phys. Chem. A* 8099–8108 (2019)

doi:10.1021/acs.jpca.9b06215.

58. Ricci, G., San-Fabián, E., Olivier, Y. & Sancho-García, J. C. Singlet-Triplet Excited-State Inversion in Heptazine and Related Molecules: Assessment of TD-DFT and ab initio Methods. *ChemPhysChem* **22**, 553 –560 (2021).

59. Reichardt, C. & Welton, T. *Solvents and Solvent Effects in Organic Chemistry*. (Wiley-VCH Verlag GmbH & Co. KGaA, 2011).

60. Kautsky, H. Quenching of Luminescence by Oxygen. *Trans. Faraday Soc.* **35**, 216–219 (1939).

61. Laing, M. The Three Forms of Molecular Oxygen A. *J. Chem. Educ.* **66**, 453–455 (1989).

62. Strambini, G. B. & Cioni, P. Pressure - Temperature Effects on Oxygen Quenching of Protein Phosphorescence. *J. Am. Chem. Soc.* **121**, 8337–8344 (1999).

63. Draxler, S. *et al.* Effects of Polymer Matrices on the Time-resolved Luminescence of a Ruthenium Complex Quenched by Oxygen. *J. Phys. Chem.* **99**, 3162–3167 (1995).

64. *Fluorescence in Industry*. (Springer, 2019). doi:https://doi.org/10.1007/978-3-030-20033-6.

65. Murawski, C., Leo, K. & Gather, M. C. Efficiency Roll-Off in Organic Light-Emitting Diodes. *Adv. Mater.* **25**, 6801–6827 (2013).

66. Hirvonen, L. M. & Suhling, K. Wide-field TCSPC : methods and applications. *Meas. Sci. Technol.* **28**, 012003 (2017).

67. The Nobel Prize in Physics 2009. https://www.nobelprize.org/prizes/physics/2009/summary/ (2009).

68. Planck, M. *The theory of Heat Radiaton*. (Blakiston, 1914).

69. Farghaly, O. A., Abdel Hameed, R. S. & Abu-Nawwas, A. A. H. Analytical application using modern electrochemical techniques. *Int. J. Electrochem. Sci.* **9**, 3287–3318 (2014).

70. Elgrishi, N. *et al.* A Practical Beginner's Guide to Cyclic Voltammetry. *J. Chem.*

Educ. **95**, 197–206 (2018).

71.   Colburn, A. W., Levey, K. J., O'Hare, D. & Macpherson, J. V. Lifting the lid on the potentiostat: a beginner's guide to understanding electrochemical circuitry and practical operation. *Phys. Chem. Chem. Phys.* **23**, 8100–8117 (2021).

72.   Gagne, R. R., Koval, C. A. & Lisensky, G. C. Ferrocene as an internal standard for electrochemical measurements. *Inorganic* **19**, 2854–2855 (1980).

73.   Bard, A. J. & Faulkner, L. R. *Electrochemical Methods: Fundamentals and Applications*. (Wiley, 2001). doi:10.1146/annurev.matsci.30.1.117.

74.   Oldham, K. B. & Zoski, C. G. Mass Transport to Electrodes. *Compr. Chem. Kinet.* **26**, 79–143 (1986).

75.   Schmidbauer, S., Hohenleutner, A. & König, B. Chemical degradation in organic light-emitting devices: Mechanisms and implications for the design of new materials. *Adv. Mater.* **25**, 2114–2129 (2013).

76.   Weijer, P. Van De, Lu, K., Janssen, R. R., Winter, S. H. P. M. De & Akkerman, H. B. Mechanism of the operational effect of black spot growth in OLEDs. *Org. Electron.* **37**, 155–162 (2016).

77.   Ding, Z. *et al.* The nature of catastrophic OLED lighting panel failure. *J. Appl. Phys.* **125**, 055501 (2019).

78.   Wang, D., Cheng, C., Tsuboi, T. & Zhang, Q. Degradation Mechanisms in Blue Organic Light-Emitting Diodes. **2**, 1278–1296 (2020).

79.   Xia, S. C., Kwong, R. C., Adamovich, V. I., Weaver, M. S. & Brown, J. J. OLED Device Operational Lifetime: Insights and Challenges. in *2007 IEEE International Reliability Physics Symposium Proceedings. 45th Annual, 2007* 253–257 (2007). doi:10.1109/RELPHY.2007.369901.

80.   Zhuang, L. & Lu, J. *In-situ ESR for Studies of Paramagnetic Species on Electrode Surfaces and Electron Spins Inside Electrode Materials. In-situ Spectroscopic Studies of Adsorption at the Electrode and Electrocatalysis* (Elsevier B.V., 2007). doi:10.1016/B978-0-444-51870-5.50014-2.

81.   Pluczyk, S., Higginbotham, H., Data, P., Takeda, Y. & Minakata, S. The impact

of replacement of nitrogen with phosphorus atom in the pyromellitic diimides on their photophysical and electrochemical properties. *Electrochim. Acta* **295**, 801–809 (2019).

82.   Pluczyk-malek, S., Honisz, D., Akkuratov, A., Troshin, P. & Lapkowski, M. Electrochimica Acta Tuning the electrochemical and optical properties of donor-acceptor D-A 2 -A 1 -A 2 -D derivatives with central benzothiadiazole core by changing the A 2 strength. *Electrochim. Acta* **368**, 137540 (2021).

83.   Mortimer, R. J. Electrochromic materials. *Annu. Rev. Mater. Res.* **41**, 241–268 (2011).

84.   Holze, R. Optical and electrochemical band gaps in Mono-, Oligo-, and Polymeric systems: A critical reassessment. *Organometallics* **33**, 5033–5042 (2014).

85.   Data, P. *et al.* Dibenzo[a,j]phenazine-Cored Donor-Acceptor-Donor Compounds as Green-to-Red/NIR Thermally Activated Delayed Fluorescence Organic Light Emitters. *Angew. Chemie - Int. Ed.* **55**, 5739–5744 (2016).

86.   Vohra, V. *et al.* Low-Cost and Green Fabrication of Polymer Electronic Devices by Push-Coating of the Polymer Active Layers. *ACS Appl. Mater. Interfaces* **9**, 25434–25444 (2017).

87.   Grassi, A. P., Tremmel, A. J., Koch, A. W. & El-Khozondar, H. J. On-line thickness measurement for two-layer systems on polymer electronic devices. *Sensors (Switzerland)* **13**, 15747–15757 (2013).

88.   Inaba, S. *et al.* Eco-Friendly Push-Coated Polymer Solar Cells with No Active Material Wastes Yield Power Conversion Efficiencies over 5.5%. *ACS Appl. Mater. Interfaces* **11**, 10785–10793 (2019).

89.   Szydłowska, B. M. *et al.* Preparation of WS2-PMMA composite films for optical applications. *J. Mater. Chem. C* **8**, 10805–10815 (2020).

90.   Hoth, C. N., Schilinsky, P., Choulis, S. A. & Brabec, C. J. Photovoltaic loss analysis of inkjet-printed polymer solar cells using pristine solvent formulations. *Macromol. Symp.* **291**–**292**, 287–292 (2010).

91.   McCaig, H. C., Myers, E., Lewis, N. S. & Roukes, M. L. Vapor sensing

characteristics of nanoelectromechanical chemical sensors functionalized using surface-initiated polymerization. *Nano Lett.* **14**, 3728–3732 (2014).

92. Istif, E. *et al.* Thiophene-Based Aldehyde Derivatives for Functionalizable and Adhesive Semiconducting Polymers. *ACS Appl. Mater. Interfaces* **12**, 8695–8703 (2020).

93. Li, J., Han, X., Bai, Q., Shan, T. & Lu, P. Electropolymerized AIE-Active Polymer Film with High QuantumEfficiency and its Application in OLED. *J. Polym. Sci. Part A Polym. Chem.* **55**, 707–715 (2017).

94. Ai, Y. & Lacroix, J. C. Self-terminated fabrication of electrochemically-gated conducting polymer nanojunctions. *Electrochem. commun.* **112**, 106674 (2020).

95. Hao, H. *et al.* A multifunctional luminescent network film electrochemically deposited from a new AIEE emitter for OLEDs and explosive detection. *Org. Electron.* **69**, 281–288 (2019).

96. Holloway, J. O., Wetzel, K. S., Martens, S., Du Prez, F. E. & Meier, M. A. R. Direct comparison of solution and solid phase synthesis of sequence-defined macromolecules. *Polym. Chem.* **10**, 3859–3867 (2019).

97. Aldawoud, A. Conventional fixed shading devices in comparison to an electrochromic glazing system in hot, dry climate. *Energy Build.* **59**, 104–110 (2013).

98. Yao, B., Zhang, J. & Wan, X. Organic Near-Infrared Electrochromic Materials. in *Electrochromic Materials and Devices* 211–240 (Wiley-VCH Verlag GmbH & Co., 2015).

99. Fabretto, M. *et al.* Colouration efficiency measurements in electrochromic polymers: The importance of charge density. *Electrochem. commun.* **9**, 2032–2036 (2007).

100. Salam, L. B., Ilori, M. O. & Amund, O. O. Properties, environmental fate and biodegradation of carbazole. *3 Biotech* **7**, 1–14 (2017).

101. Schmidt, A. W., Reddy, K. R. & Knölker, H. J. Occurrence, biogenesis, and synthesis of biologically active carbazole alkaloids. *Chem. Rev.* **112**, 3193–3328 (2012).

102. Zhao, Y., Liu, H. & Sun, B. Chiral induction in carbazole-conjugated covalent organic frameworks: A supersensitive fluorescence sensing platform for chiral recognition. *Sensors Actuators B Chem.* **354**, 131253 (2021).

103. Patel, O. P. S. *et al.* Naturally Occurring Carbazole Alkaloids from Murraya koenigii as Potential Antidiabetic Agents. *J. Nat. Prod.* **79**, 1276–1284 (2016).

104. Han, L., Meng, C., Zhang, D., Liu, H. & Sun, B. Fabrication of a fluorescence probe via molecularly imprinted polymers on carbazole-based covalent organic frameworks for optosensing of ethyl carbamate in fermented alcoholic beverages. *Anal. Chim. Acta* **1192**, 339381 (2021).

105. Zhang, Y., Wada, T. & Sasabe, H. Carbazole photorefractive materials. *J. Mater. Chem.* **8**, 809–828 (1998).

106. Sathiyan, G., Sivakumar, E. K. T., Ganesamoorthy, R., Thangamuthu, R. & Sakthivel, P. Review of carbazole based conjugated molecules for highly efficient organic solar cell application. *Tetrahedron Lett.* **57**, 243–252 (2016).

107. Wex, B. & Kaafarani, B. R. Perspective on carbazole-based organic compounds as emitters and hosts in TADF applications. *J. Mater. Chem. C* **5**, 8622–8653 (2017).

108. Ledwon, P. Recent advances of donor-acceptor type carbazole-based molecules for light emitting applications. *Org. Electron.* **75**, 105422 (2019).

109. Yin, C., Zhang, D. & Duan, L. A perspective on blue TADF materials based on carbazole-benzonitrile derivatives for efficient and stable OLEDs. *Appl. Phys. Lett.* **116**, (2020).

110. Kricka, J. & Laboratories, D. Dibenz[b,/]azepines and Related Ring Systems. *Chem. Rev.* **74**, (1974).

111. Pashazadeh, R. *et al.* An iminodibenzyl-quinoxaline-iminodibenzyl scaffold as a mechanochromic and dual emitter: donor and bridge effects on optical properties. *Chem. Commun.* **54**, 13857–13860 (2018).

112. Kukhta, N. A., Batsanov, A. S., Bryce, M. R. & Monkman, A. P. Importance of Chromophore Rigidity on the Efficiency of Blue Thermally Activated Delayed Fluorescence Emitters. *J. Phys. Chem. C* **122**, 28564–28575 (2018).

113. Jhun, B. H., Jeong, D. Y., Nah, S., Park, S. Y. & You, Y. Novel anti-Kasha fluorophores exhibiting dual emission with thermally activated delayed fluorescence through detouring triplet manifolds. *J. Mater. Chem. C* **9**, 7083–7093 (2021).

114. Wang, Z., Wang, Z., Lu, P. & Wang, Y. Preparation and Photoluminescent Properties of Three 5-Amino Benzothiadiazoles (5-amBTDs). *Chem. - An Asian J.* **15**, 3519–3526 (2020).

115. Kusakabe, Y., Wada, Y., Nakagawa, H., Shizu, K. & Kaji, H. Conformation Control of Iminodibenzyl-Based Thermally Activated Delayed Fluorescence Material by Tilted Face-to-Face Alignment With Optimal Distance (tFFO) Design. *Front. Chem.* **8**, (2020).

116. Frank, S. N., Bard, A. J. & Ledwith, A. Electrochemical Oxidation of Iminobibenzyl and Related Compounds. *J. Electrochem. Soc.* **122**, 898–904 (1975).

117. Bachar, N. *et al.* Sensor arrays based on polycyclic aromatic hydrocarbons: Chemiresistors versus quartz-crystal microbalance. *ACS Appl. Mater. Interfaces* **5**, 11641–11653 (2013).

118. Aumaitre, C. & Morin, J. F. Polycyclic Aromatic Hydrocarbons as Potential Building Blocks for Organic Solar Cells. *Chem. Rec.* **19**, 1142–1154 (2019).

119. Jung, C. *et al.* A new photostable terrylene diimide dye for applications in single molecule studies and membrane labeling. *J. Am. Chem. Soc.* **128**, 5283–5291 (2006).

120. Schmidt-Mende, L. *et al.* Self-organized discotic liquid crystals for high-efficiency organic photovoltaics. *Science (80-.).* **293**, 1119–1122 (2001).

121. Chung, Y. H. *et al.* A pure blue emitter (CIEy ≈ 0.08) of chrysene derivative with high thermal stability for OLED. *J. Mater. Chem. C* **3**, 1794–1798 (2015).

122. Schnitzlein, M., Mützel, C., Shoyama, K., Farrell, J. M. & Würthner, F. PAHs Containing both Heptagon and Pentagon: Corannulene Extension by [5+2] Annulation. *European J. Org. Chem.* **2**, 1–6 (2021).

123. Zhigalko, M. V., Shishkin, O. V., Gorb, L. & Leszczynski, J. Out-of-plane

deformability of aromatic systems in naphthalene, anthracene and phenanthrene. *J. Mol. Struct.* **693**, 153–159 (2004).

124. Abou-Hatab, S., Spata, V. A. & Matsika, S. Substituent Effects on the Absorption and Fluorescence Properties of Anthracene. *J. Phys. Chem. A* **121**, 1213–1222 (2017).

125. Martin, J. W. *et al.* The Polarization of Polycyclic Aromatic Hydrocarbons Curved by Pentagon Incorporation: The Role of the Flexoelectric Dipole. *J. Phys. Chem. C* **121**, 27154–27163 (2017).

126. Wang, B. T., Petrukhina, M. A. & Margine, E. R. Electronic transport properties of selected carbon π-bowls with different size, curvature and solid state packing. *Carbon N. Y.* **94**, 174–180 (2015).

127. Hirai, M., Tanaka, N., Sakai, M. & Yamaguchi, S. Structurally Constrained Boron-, Nitrogen-, Silicon-, and Phosphorus-Centered Polycyclic π-Conjugated Systems. *Chem. Rev.* **119**, 8291–8331 (2019).

128. Schaub, T. A., Padberg, K. & Kivala, M. Bridged triarylboranes,-silanes,-amines, and-phosphines asminimalistic heteroatom-containing polycyclic aromatichydrocarbons: Progress and challenges. *J. Phys. Org. Chem.* **33**, (2020).

129. Ito, S., Tokimaru, Y. & Nozaki, K. Benzene-FusedAzacorannuleneBearinganInternalNitrogenAtom. *Angew. Chemie - Int. Ed.* **54**, 7256–7260 (2015).

130. Yokoi, H. *et al.* Nitrogen-embedded buckybowl and its assembly with C60. *Nat. Commun.* **6**, 1–9 (2015).

131. Mishra, S. *et al.* On-surface synthesis of a nitrogen-embedded buckybowl with inverse Stone-Thrower-Wales topology. *Nat. Commun.* **9**, (2018).

132. Krzeszewski, M., Dobrzycki, Ł., Sobolewski, A. L., Cyranski, M. K. & Gryko, D. T. Bowl-ShapedPentagon-and Heptagon-EmbeddedNanographeneContainingaCentralPyrrolo[3,2-b]pyrroleCore. *Angew. Chemie - Int. Ed.* **60**, 14998–15005 (2021).

133. Deng, N. & Zhang, G. Nitrogen-Centered Concave Molecules with Double Fused Pentagons. *Org. Lett.* **21**, 5248–5251 (2019).

134. Song, Y. & Zhang, G. Effect of Fusion Manner of Concave Molecules on the Properties of Resulting Nanoboats. *Org. Lett.* **23**, 491–496 (2021).

135. Zhou, L. & Zhang, G. A Nanoboat with Fused ConcaveN-Heterotriangulene. *Angew. Chemie - Int. Ed.* **59**, 8963–8968 (2020).

136. Zhu, G. *et al.* Modulating the properties of buckybowls containing multiple heteroatoms. *Org. Chem. Front.* **8**, 727–735 (2021).

137. Dias, F. B., Penfold, T. J. & Monkman, A. P. Photophysics of thermally activated delayed fluorescence. *Methods Appl. Fluoresc.* 012001 (2017) doi:10.1002/9783527691722.ch12.